Next Generation Graphene Photonics Enabled by Ultrafast Light-Matter Interactions and Machine Learning

by

Dehui Zhang

A dissertation submitted in partial fulfillment
of the requirements for the degree of
Doctor of Philosophy
(Electrical and Computer Engineering)
in The University of Michigan
2021

Doctoral Committee:

Associate Professor Zhaohui Zhong, Chair
Professor L. Jay Guo
Associate Professor Xiaogan Liang
Professor Theodore B. Norris

Dehui Zhang

dehui@umich.edu

ORCID: 0000-0002-7077-0639

Dedicated to My Family

Acknowledgments

"You will never know it unless you try it." my advisor, Prof. Zhaohui Zhong, said many times in our discussions. My years at Ann Arbor are, by itself, an experiment with many unexpected outcomes: Besides growing knowledge of the physical world, the journey repeatedly forces me to reflect on myself, and by doing so, nurtures my taste and cultivates my practice on both research and life. I am amazed by the largely unexpected, positive and negative 'data' of this six-year experiment. The lessons are invaluable for a lifetime.

My advisor, Prof. Zhaohui Zhong, is the one who made my experiment possible. I am grateful for the resource and guidance he provided. He is intelligent, kind, and professional. In my early career, his wise words saved me from impetuosity and pessimism. His openness to new ideas and disagreements gave me maximum opportunity to challenge myself and improve.

I would also like to express my gratitude to Prof. Theodore Norris. All my Ph.D. projects are in close collaboration with Ted's group. His passion, wisdom, and sense of humor never fail to impress and inspire me in this journey. My thesis committee, Prof. Jay Guo and Prof. Xiaogan Liang, gave me long-lasting supports and sincere advice in my career. Their kindness is unforgettable.

My lab mates, Dr. Che-Hung Liu, Dr. Minmin Zhou, Dr. Wenzhe Zang, Mr. Zhe Liu, Ms. Audrey Rose Gutierrez, Mr. Wade Wu, gave me lots of help in my work. Special thanks to Che-Hung for his dedicated mentorship in my first year at Ann Arbor, and to Audrey Rose for proofreading the thesis. Dr. Miao-Bin Lien, Dr. Gong Cheng, Mr. Zhen Xu, and Mr. Zhengyu Huang in Prof. Norris' group, and Dr. Thomas E. Beechem, Dr. Michael D. Goldflam, Dr. David W. Peters from Sandia National Lab made substantial contributions in my projects. I feel lucky to collaborate with them. I would also like to thank all my dearest friends in Ann Arbor. You will be a significant part of my nostalgia every time I think of this lovely town.

Lastly, and most importantly, I would like to thank my entire family for their love and support. My debt to my parents and grandparents is beyond measure. My wife, Ms. Meiqi Guo, is forever a miracle in my life that never follows the first principles. She is the one who gave me courage in the darkest times. She is also a magnificent source of inspiration in both my life and career. And our beloved cat, Paris, who typed (with his paw) his insightful comments (“bbbbbbbew”) in my thesis.

I spent six years running an experiment, and the answer is, to love and be true to life.

Ann Arbor, March 20

Table of Contents

List of Figures

Abstract

Graphene was first experimentally studied in 2004, featuring an atomically-thin structure. Since then, many unique photonic and electrical properties of graphene and other 2D materials were reported. However, additional efforts are necessary to convert these findings in physics to successful industrial applications. This thesis presents works exploiting the picosecond-scale ultrafast light-matter interactions in graphene to meet the growing demands in IR sensing, 3D detection, and THz light source.

We will start from graphene's interactions with ultrafast lasers. The hot carrier generation, relaxation, and transport will be discussed in graphene and graphene heterostructures. We present a graphene phototransistor with decent near- and mid-infrared (IR) responsivity. Moreover, the detector's responsivity is tunable with a gate voltage. The responsivity has different gate dependence under different illumination wavelengths. Based on the spectrally-resolved response, we adopt least square regression algorithms to extract the light source's spectral information at near-infrared. We further perform first-principle photocurrent simulations and spectral reconstructions on defect-free ideal devices with optimized band structure. The results indicate the detector's potential as an ultra-compact on-chip spectrometer for multispectral imaging after further developments.

Then we discuss how the graphene detector's high transparency enables a novel 3D detection and imaging technology. Our graphene phototransistors absorb < 10% of light and give a 3 A/W photoresponse at 532 nm wavelength. The high transparency and sensitivity enable transparent photodetector arrays built on glass substrates, with over 85% of incident light power transmits through such an imager chip. We stack multiple transparent arrays at different focal depths in a camera system. The setup enables simultaneous light intensity (image) acquisition at different depths. We use artificial neural networks to process the image stack data into 3D position and configuration of the objects. For a proof-of-concept demonstration, we used the setup to achieve

3D ranging and tracking of a point source. The technical approach benefits from compactness, high speed, and decent power efficiency for real-time 3D tracking applications.

Lastly, we explore the potential of graphene heterostructures as terahertz (THz) emitters and ultrafast photodetectors. The picosecond-scale light-matter interaction of graphene allows us to engineer its optical and electrical structures for THz field emission. We insert a graphene layer in the channel of a silicon photoconductive switch. The device works as a THz electromagnetic wave emitter under femtosecond laser pulse illumination. We use an on-chip pump-probe system to study the temporal and spatial behavior of the THz generation. Our device's emission amplitude is 80 times larger than a graphene-free control group under identical device geometry and test conditions. Moreover, we also observe strong photocurrent generation below 0.5 ps verified by the photocurrent autocorrelation test. The responsivity is 800 times larger than that in the graphene-free control group. The substantial enhancements are attributed to the high mobility in graphene and the strong absorption in silicon. Gate dependence observations indicate vertical hot-carrier transfer from the silicon layer to the graphene layer, followed by efficient lateral charge separation inside graphene. The results open the gate for more research and development of graphene-based strong THz sources and sensitive ultrafast photodetectors.

We conclude the works with strategies to convert graphene's unique properties to practical and competitive applications. The strategies are extended to general nanodevice and nano-system development methodologies. Specifically, we propose the synergic design of nanodevices and machine learning algorithms as a feasible approach towards many new applications.

Chapter 1
Introduction

1.1 Overview: Commercial Applications of Graphene in Optoelectronics

Despite the early theoretical works on graphite[1,2], graphene was not experimentally isolated into a monolayer until 2004[3]. Since then, significant efforts have focused on this two-dimensional material. Myriad unique physical properties and potential applications have been reported. In the field of electronics and optics, graphene features fascinating properties. The carrier mobility exceeds 150,000 cm^2/Vs at ambient conditions[4], more than two orders of magnitude higher than silicon. With a single atomic layer, suspended graphene absorbs 2.3% percent of light at 3 eV[5]. The absorption is significant for a single layer but allows decent transparency. More importantly, graphene has no bandgap, enabling ultra-broadband light-matter interaction from ultraviolet to microwave frequencies[6].

Based on these properties, a large variety of applications has been demonstrated with graphene-based devices. Few-layer graphene is both transparent and conductive. It is a feasible candidate as transparent electrodes for displays[7,8] and solar cells[9,10]. The strong light-matter interaction leads to IR and THz photodetectors and modulators[11,12,13]. The picosecond-scale photo-excited carrier dynamics points to applications in mode-locked lasers[14,15] and THz signal generation[16]. More importantly, due to the low density of states (DoS), the electrical and optical properties of graphene can be actively tuned with electrical gating, offering more possibilities to the applications mentioned above.

From the industry side, market studies show promising global market demand for graphene. It is predicted to increase from US$15-50 million in 2015 to US$200-2000 million around 2025[17], with an average growth rate of approximately 40%. Notice that the value includes only the

graphene material, not the end product that contains graphene. More specifically, in the field of electronics and optoelectronics, a >20% growth rate is expected, though the revenue remains low temporarily[18,19,20,21]. The perspective is promising yet still dwarfed by the abundant innovations reported in academia to date. The discrepancy stems from several reasons[17,22]:

1. Mass production of graphene devices requires new process development. For applications in microelectronics applications, this includes synthesizing low-defect, wafer-scale samples of graphene, as well as a high-reliability transfer technique to an arbitrary substrate. Even though wafer-scale chemical vapor deposition (CVD) growth and roll-to-roll transfer of graphene has been reported[8], the extra process still means an additional expense over traditional semiconductor fabrication.

2. For some proposed applications, like IR sensing, there are other competing candidate materials and devices with similar functions[23]. Despite the advantages graphene holds in specific applications, the industry is less motivated to shift from existing solutions with modest performance and take risks to develop new approaches.

3. For many applications, the device's supreme performance relies on the high quality of exfoliated graphene. Devices fabricated with CVD-grown samples cannot achieve comparable performance due to intralayer defects and surface contaminations. The currently obtainable mass-produced graphene is still the CVD-grown samples. This limits the industrial scaling up of such innovations.

My efforts to bridge 2D science and technology focus on the field of optoelectronics. To innovate mass-producible, industrially feasible applications with 2D materials, we focus on CVD-grown samples and propose two strategies:

(1) If a 2D technology surpasses existing counterparts in performance more than ten times, the industry might be motivated to revolutionize their products using the new solution.

(2) If a 2D technology fulfills crucial demands that conventional technologies cannot achieve, it can be finalized as a successful product.

My three projects took both strategies: With the first strategy, an 80-time-higher THz emission and 800-time photo-response enhancement were observed in a 2D-3D heterostructure. For the

second strategy, a multi-focal-plane camera combines graphene photodetectors and a machine learning method for 3D object detection. I also explore the possibility of on-chip spectrometers with 2D heterostructures, which feature an unprecedented small footprint.

The experiences lead to a third strategy to industrialize 2D technologies: A combination of 2D and other nano-sensors and artificial neural networks forms a novel reservoir computing system. The requirements of the reservoir design would inspire the design of the nanodevices. The new perspective and paradigm would lead to more innovations in 2D science and technology.

1.2 Electrical and optical properties of graphene

Graphene is composed of carbon atoms aligned in a planar honeycomb structure. Fig. 1.1 shows two inequivalent groups of carbon atoms paired with inversion symmetry. They interpenetrate each other in a hexagonal 2D lattice. The carbon atoms are bonded with sp^2-hybridized electrons. The extra valance electrons in the p_z orbital make up the π-bands and π^*-bands. These bands dominate the unique electronic and optical properties we study in this thesis. The band structure was theoretically derived with a tight-binding model[1] and expressed as:

$$E(k_x, k_y) = \pm t\sqrt{1 + 4cos^2\left(\frac{k_x a}{2}\right) + 4\cos\left(\frac{k_x a}{2}\right)\cos\left(\frac{\sqrt{3}k_y a}{2}\right)} \qquad (1.1)$$

with the interaction integral t = 2.5 eV and the lattice constant a of 0.246 nm.

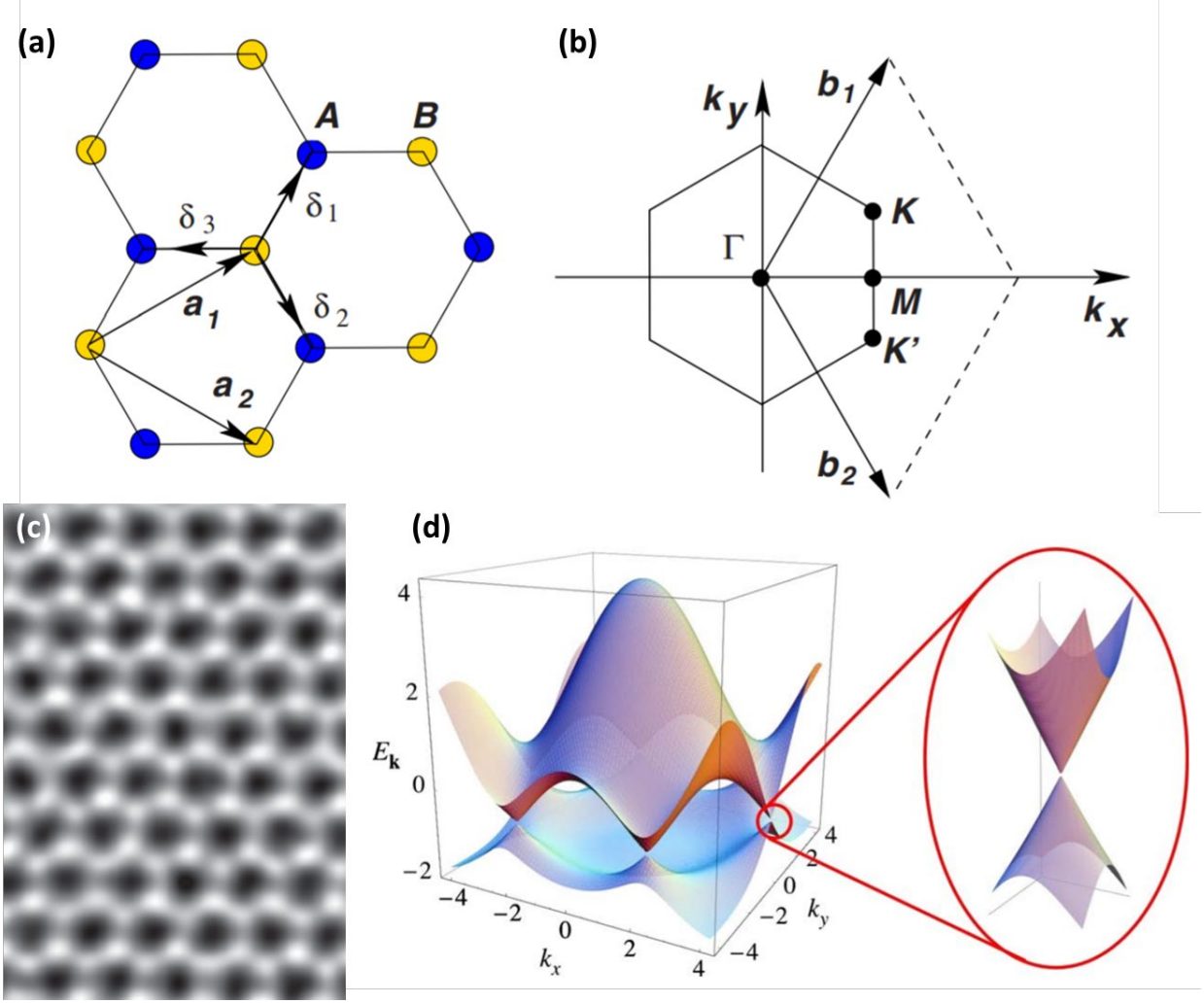

Figure 1.1. Graphene's lattice structure (a) and Brillouin zone (b). (c) is a TEM image of graphene's honeycomb lattice structure[24]. Its calculated band structure is in (d)[25].

An immediate observation from equation (1.1) is the gapless nature of graphene. As shown in Fig. 1.1 (d), the bandgap closes at corners of the first Brillouin zone, namely K and K' points. These points pair with inversion symmetry and form Dirac cones with linear dispersion relation. Near the Dirac cones, the dispersion relation writes[26]:

$$\widehat{H} = \pm\hbar v_F \boldsymbol{\sigma} \cdot \boldsymbol{\kappa} \qquad (1.2)$$

where $v_F \sim 8 \times 10^5$ m/s is the Fermi velocity. $\boldsymbol{\sigma} = (\sigma_x, \sigma_y)$ is the Pauli matrices, which operate on the pseudo-spin. The pseudo-spin stems from the superposition of atomic orbits of inequivalent carbon atoms, labeled with A and B in Fig. 1.1 (a). $\boldsymbol{\kappa} = \boldsymbol{k} - \boldsymbol{K}$ is the wavevector

deviation from the Dirac cone. This linear dispersion relation is a condensed matter analogy to the relativistic massless Dirac fermions[27].

There are several consequences of this dispersion relation and Hamiltonian: First, the gapless nature makes the material a semimetal, with a minimum quantum conductance of $4e^2/h$ at the charge neutral point[28] and a resistance around 1 kΩ/□ under ambient doping conditions. Unlike metals, the low DoS allows electrostatic doping of the semimetal like semiconductors, while supporting a large current in a single atomic layer.

Secondly, the pseudo-spin formalism of the wavefunction suppresses the matrix element for back-scattering of carriers[29,30]. As a result, ballistic carrier transport is observed at the scale of ~0.3 μm at room temperature[28]. The suppressed back-scattering also results in record-high carrier mobility. Suspended graphene gives a mobility of 10,000,000 $cm^2V^{-1}s^{-1}$ near the charge neutral point at 5K, when suspended in vacuum[31]. At ambient conditions, the mobility is sensitive to the dielectric environment, as discussed later in this section, but can still be two orders of magnitudes higher than silicon, enabling high-speed response to electric fields to THz bands.

Thirdly, though the gapless nature makes graphene a poor light emitter, it also allows inter-band absorption of photons with frequencies from microwave to UV, enabling photodetection over an ultra-broad spectral range. The greatest interests are on the IR to THz band. At IR frequencies lie the optical fingerprints of molecules, while the THz frequency response is also essential for security applications. Furthermore, the other technologies for these bands, including light sources, modulators, and detectors based on all existing solutions are less developed compared to other bands. Hence many graphene applications have been reported in these bands[6,11,12].

Furthermore, graphene supports surface plasmonic polaritons in the FIR-to-THz band[6,12]. Graphene was patterned into gratings and other nanostructures for efficient optical excitation at target wavelengths. The resonance is actively tunable via electrostatic doping of graphene nanostructures, which is fundamentally different from the surface plasmons in metals.

1.3 Synthesis and Subsequent Processing

Material synthesis is the first step for the experimental study of graphene. It largely determines the final device's electric and optical properties. Due to the large surface-volume ratio, graphene is also very sensitive to the environment. Hence subsequent processing also plays an important role in device performance. In this section, we introduce the mainstream methods to synthesize (or isolate) graphene monolayers, emphasizing the CVD method used in our works. Then we discuss the surface sensitivity of graphene and how the post-growth processes influence the physical properties.

1.3.1 Graphene Synthesis

The most widely-adopted graphene samples are produced with three methods: mechanical exfoliation, epitaxial growth, and CVD. Device requirements often determine the proper synthesis method. Typical considerations include the sample size, defect level, wrinkle, grain size, and surface contamination in the synthesis process.

The first monolayer graphene sample was isolated from graphite using the mechanical exfoliation method[3]. Graphite flakes are first placed on scotch tapes. Then two tapes are adhered, sandwiching graphite flakes in between. The Van der Waals interaction between graphene monolayers in bulk graphite is weak. When pulling the tapes apart, the flakes exfoliate into pieces along the graphene plane. After multiple exfoliations, some flakes become monolayers. The monolayers can then be dry-transferred to the sample, as described later in Section 1.3.2. To date, this method still produces the graphene samples with the best qualities, including low defect/wrinkle density and low surface contamination. The sample has a larger ballistic transport length and a longer dephasing time for the carriers than in samples produced with other methods. The method is ideal for studying quantum properties and dynamic processes since the clean system blocks any additional energy dissipation path extrinsic to the material. However, the exfoliated flakes are usually tens to hundreds of micrometers in size and need precise positioning with a micro-stage. This limits its application in commercial products, which requires wafer-scale, uniform samples.

Epitaxy method silicon carbide substrate supports wafer-scale growth[32,33]. The substrates heat up to around 1500 °C. Silicon atom sublimates on the (0001) surface of silicon carbides at this

temperature, producing high-quality graphene layers. However, this method needs precise control of growth conditions. Moreover, the silicon carbide substrate is expensive compared to silicon wafers widely used in the industry.

The growth method with probably the highest industrial potential is the CVD process on copper foil. It is also the process we use in our device fabrication. In this process, copper foil is heated up to 1000 °C, with a mixture of methane and hydrogen as the carbon source[8,34]. The graphene grown is uniform in centimeters to meters. However, for most works reported, the graphene is polycrystalline, with a grain size from 1 to 100 micrometers. The mobility is typically a few thousand $cm^2V^{-1}s^{-1}$. Recent works on the copper foil substrate growth give more exciting results: Meter-sized single-crystal graphene was epitaxially grown on thermally-treated, (1 1 1) Cu surface with a high throughput of 2.5 cm/min[35]. The graphene was then wet transferred with hBN capsulation, with a mobility of 15,000 $cm^2V^{-1}s^{-1}$ at room temperature. The value is still significantly lower than the mobility measured in exfoliated samples. Nevertheless, it shows the possibility of scalable, high-quality graphene for industrial applications.

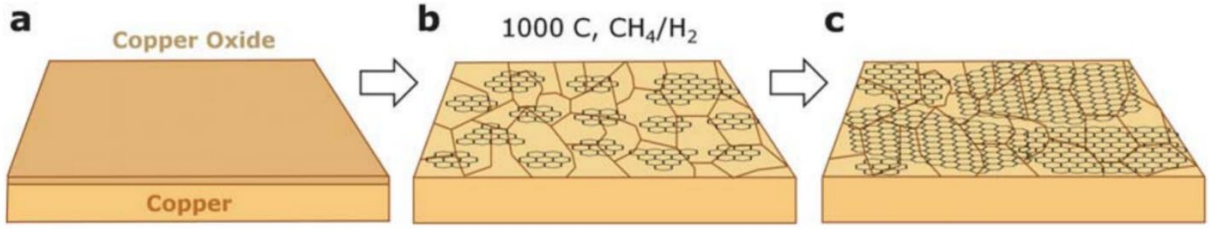

Figure 1.2. A schematic of the CVD growth process of graphene on copper foil[36].

1.3.2 Graphene Transfer Process

One bonus that graphene and other 2D materials offer is compatibility with any substrate. The Van der Waals interaction supports graphene transfer to a large variety of substrates to fabricate versatile devices. This is fundamentally different from silicon or III-V compounds, where a buffer layer or more complex techniques is required for solving the lattice mismatch. As a result, the separation of graphene from its original substrate and transfer to a new substrate is essential.

Three transfer processes are most common in literature: wet transfer, dry transfer, and roll-to-roll transfer. In the wet transfer process, a layer of PMMA is first spin-coated on the graphene sample. The sample is baked at 190 °C for 3 min. Then the sample is placed in an etchant solution to remove the substrate. In our work, we used ammonium persulfate ($(NH_4)_2S_2O_8$, 0.1 mol/L) to remove the copper foil substrate of CVD-grown graphene, with an etch time of 24 hours. After removal of substrate, the PMMA-graphene layer floats on water due to the hydrophobic nature of PMMA. We manually transfer the sample to DI water multiple times to remove the etchant and copper ions from the graphene surface. Then we transfer the graphene layer to the required substrate and dry it in the air for 24 hours. Lastly the PMMA is removed by soaking the sample in acetone for > 1 hour and subsequent rinsing with acetone and isopropanol. The wet transfer process is low-cost, easy to process, and large in area compared with the dry transfer. It is especially suitable for lab processing of centimeter-sized, CVD-grown graphene samples. However, the manual process in water makes it hard to locate the transfer position with micrometer accuracy, so that it is not suitable for transferring exfoliated samples. Moreover, it leaves water molecules and ions on the interface, resulting in mobile ions and chemical doping in the final device.

During the dry transfer process[37], thermal-release tape removes the graphene layer from the substrate. Then the tape is adhered with the target substrate, usually with the help of a micro-positioning system for exfoliated samples. After applying uniform pressure to the substrate, the substrate is heated up to around 120 °C. This treatment removes the adhesiveness of the tape. Hence the graphene layer is transferred to the substrate. This and related methods are suitable for preparing exfoliated samples, as multiple layers of graphene and other 2D materials can be performed with one stamping, leaving an ultra-clean interface. It also supports the transfer of reactive 2D materials, such as black phosphorus and WTe_2. Additional hydrocarbon removal is necessary to improve the sample quality, as will be discussed in the next section.

For larger scale, high throughput manufacturing, a roll-to-roll transfer method was also demonstrated[8]. Some literature describes the method as a type of dry transfer process. However, the mechanism is a combination of the two methods: a thermal-release tape was first adhered to the graphene on copper foil substrate with pressure produced by two rollers. Then solution-based copper etchant is used to remove the copper. The graphene surface is then exposed to the air and

dried before a thermal release process, which leaves the graphene layer on the target substrate. Also, controlled chemical doping is possible with an additional setup similar to that of copper etching.

1.3.3 Dielectric Environment Engineering

The physical phenomena can vary dramatically for the same device structure produced with different fabrication processes. Subsequent fabrication processes may introduce defects, contamination or reduce the coverage mechanically and/or chemically. Here we discuss the dielectric environment engineering to produce a clean device.

Graphene is single-atom-thick. In graphite, each layer of graphene is spaced 0.335 nm from another layer. After isolation, it has a Van der Waals interaction with substrates. The interaction ensures that the graphene-substrate distance lies in the same order of magnitude under good adhesion conditions. The distance is small enough for substrate potentials to modulate the motion of carriers inside graphene. Electrons scatter due to charged surface states and impurities, rough substrate surface, or optical phonons of substrate materials. Researchers observe that different substrates give different carrier mobilities[38,39] in graphene. When gated as a graphene transistor, there can be large hysteresis due to mobile ions on the surface.

Moreover, many other processes can happen in the sub-micrometer scale interface, including non-radiative energy transfer (NRET), charge transfer, and exciton-like bonded states. These processes produce additional energy dissipation and carrier transport pathways. In systems involving quantum coherence or ultrafast carrier dynamics, the target phenomenon may be drowned out by side-effects produced by these substrate-related processes.

The cleanest samples produced to date are exfoliated samples dry-transferred with hBN encapsulation. The hBN layer improves graphene mobility by more than an order of magnitude compared with the SiO2 substrate. The sandwiched structure can be fabricated with multiple stampings in a single transfer process. Hence the exfoliated samples suffer the least from interface contaminations in between. However, water molecules and hydrocarbons can still

reside at the interface due to exfoliation, organic layer removal, or water vapor in the ambient environment.

For CVD grown samples, more contamination sources are present even with a subsequent hBN encapsulation: The wet transfer process introduces etchant and copper ions, plus more water molecules than dry transfer. The relatively weaker and non-uniform adhesion with the substrate results in more wrinkles and roughness at the interface.

Besides all of this, the plasma-etch process in subsequent lithography steps leaves a thin layer of cross-linked photoresist on the sample, which is hard remove using acetone[40].

Multiple processes can remove the contaminations. In our wet transfer process, the sample is floated in DI water in 5 petri dishes for an hour to let ions diffuse away from the graphene surface. Most hydrocarbon in the organic coating or exfoliation process is removable with hot/cold acetone soaking for hours. After that, the remained organic molecules (including the solvent molecules) can be further reduced with annealing in N_2 or Ar at 300-500 °C for hours. Annealing's tradeoff is that it leaves amorphous carbons and causes additional defects in graphene with prolonged annealing time and elevated temperature. For interface hydrocarbons, annealing also helps the molecules to agglomerate into packets between two 2D material layers. The process leaves most interface areas clean even though a small amount of contamination is left. Moreover, annealing improves the graphene-substrate adhesion, reducing mechanical damage to the sample in subsequent processes. For cross-linked photoresists, an additional step of Remover-PG soaking is efficient, at the cost of additional damage to the graphene layer.

In our work, the device performance is robust enough without hBN encapsulation. Hence the hBN method is not used unless specifically mentioned. Other dielectric environment engineering methods, including ALD-grown passivation layers, are applied by case depending on the device design. We will discuss it in the following chapters.

1.4 Overview of Thesis

In this chapter, we generally reviewed graphene's industrial opportunities in optoelectronics. We also described the physical properties and critical processes that potentially make industrial

success feasible. Chapter 2 will go further into the ultrafast light-matter interaction of graphene, which is the theoretical building block of this thesis. Chapter 3 describes the instrumentation applied to conduct the experiments. Chapter 4 introduces our work to make an on-chip computational spectrometer based on the electrical tunability of graphene. A multi-focal-plane imaging system based on graphene photodetector arrays is discussed in chapter 5. It demonstrates a novel architecture to realize high-performance 3D sensing by combining graphene optoelectronics with machine learning. Chapter 6 reports enhanced THz emission and ultrafast photodetection, which is made possible by a metal-graphene-silicon photoconductive switch. Lastly, we conclude our work in chapter 7. We discuss how machine learning produces new opportunities to bridge nanoscale optoelectronics with successful commercial applications.

Chapter 2
Review: Ultrafast Hot Carrier Dynamics in Graphene and Its Heterostructures

2.1 Introduction

When photons propagate in materials, they can get absorbed and transfer energy to excited states of the material. For the photon energy from visible to THz, the transition from ground states to excited states may happen between bands/sub-bands of electrons, states of atomic motions, phonons, charge-trapped states, etc. For electron excitations (which is of our best interest), the electron occupies a high-energy state and leaves the previous low-energy state empty, creating an electron-hole pair. The system is in non-equilibrium with many electron-hole pairs (hot carriers) after illumination. As required by the second law of thermodynamics, the hot carriers have to relax to equilibrium via different paths: they can emit another photon to jump back to a low energy state, known as radiative relaxation, or dissipate energy to the lattice through Auger, defect- or phonon-assisted processes, which is categorized as non-radiative relaxation. These energy dissipation processes happen in different time-scales following Fermi's Golden Rule:

$$\Gamma_{i\to f} = \frac{2\pi}{\hbar}|\langle f|H'|i\rangle|^2\rho(E_f) \quad (2.1)$$

where the actual material and transition specify the matrix elements.

To exploit the hot carriers, we do not want them to relax freely to equilibrium, which trivially heats the material. We design structures to modify the carriers' spatial transport, converting a 'material' to a 'device'. Take a p-n photodiode as an example. The semiconductor is doped into p-type and n-type in two regions. The density gradient of carriers creates a built-in electric field at the interface. Under illumination, hot electrons and holes are dragged to opposite positions by

the electric field. The spatial separation of electrons and holes creates a net current. The photocurrent is collected outside the interface. Hence energy is harvested from the diode working as a solar cell. Optoelectronics' general purposes lie in the two aspects described: the study of the light-matter interaction and excited carrier dynamics in different materials, and engineering of the materials and (or) structures to manipulate the interactions and transports for different applications.

In graphene, the hot carrier dynamics differ from the case in either metals or semiconductors. After hot carriers' generation, the thermalization features hot carrier multiplication and phonon bottleneck effects, creating unique picosecond-scale dynamics of hot carriers. Understanding the hot carrier dynamics, and engineering the subsequent energy and charge transfer, are very important for designing novel optoelectronic devices based on graphene. This chapter reviews the ultrafast hot carrier dynamics in graphene, including its transport in specifically designed heterostructures.

2.2 Hot Carrier Relaxation

The hot carrier relaxation in graphene follows two different time scales, τ_1 and τ_2. After a short laser pulse illumination, the excited hot carriers transfer energy to optical phonons and other carriers in the first ~100 fs (τ_1). The hot carriers form quasi-Fermi levels in a subsystem decoupled to the lattice. The temperature can be a few thousands of Kelvins, much higher than that of the lattice. The second process generates a larger population of non-equilibrium carriers with lower energy. This hot carrier multiplication process is particularly efficient for heavily doped graphene samples.

After the quick thermalization process, the carriers experience a slower cooling-down. The time scale τ_2 ranges from one to tens of picoseconds depending on material preparation and temperature[41,42]. The process is much slower due to the optical phonon bottleneck effect: In τ_1, hot carriers dissipate energy mainly to the optical phonons close to the center of the Brillouin zone, as required by energy and momentum conservation of the process. As hot carriers' energy drops below the optical phonon energy at ~196 meV, this process fails to cool down the sample further. Hence electrons can only dissipate energy with much less efficient pathways such as

energy transfer to multiple acoustic phonons and the supercollision process enhanced by disorders[43].

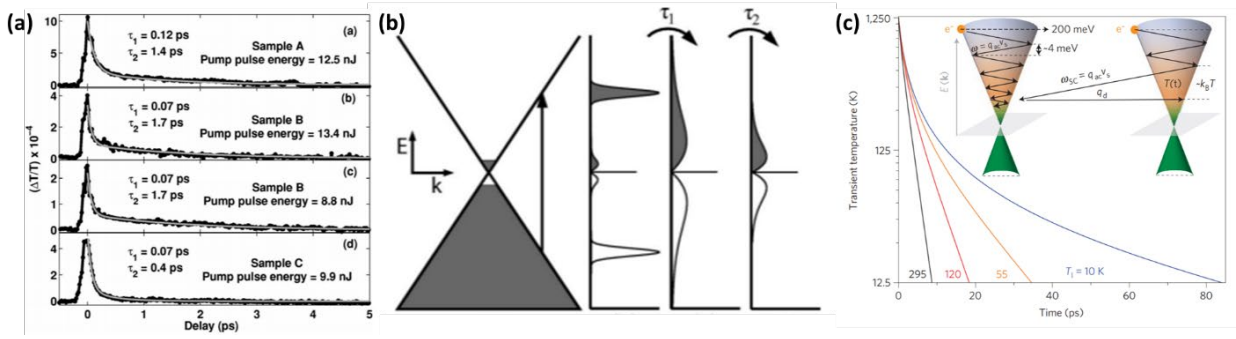

Figure 2.1. (a) and (b) illustrate the transient dynamics of photoexcited hot-carriers measured with a pump-probe setup[41]. (c) presents a picture of multiple acoustic phonon cooling (left schematic) and the supercollision process (right)[43].

2.3 Application: Graphene Photodetectors

As discussed above, the unique ultrafast dynamics of photo-excited hot carriers in graphene offer opportunities for ultra-broadband photodetection. However, efficient charge separation before the hot carrier reaches thermal equilibrium requires careful design of device structures. This section summarizes different methods reported for efficient photodetection using graphene as the optically active material. The methods include electrical designs to build photovoltaic, photoconductive, photogating, photo-thermoelectric, and bolometric detectors. Lastly, we introduce optical design strategies to increase the light-matter interaction in graphene.

2.3.1 Photovoltaic and Photoconductive Detectors

The most straightforward way to extract carriers after excitation is through an electric field. The electric field can be a built-in field in the structure, or a field caused by a bias between two contacts.

As briefly introduced in Section 2.1, the photovoltaic effect utilizes a built-in electric field to spatially separate electron-hole pairs in the material. The built-in field is created by breaking the material's inversion symmetry, either with different doping (p-n or p-i-n junctions) or interface with other materials (heterojunctions). Photovoltaic effect in graphene-metal junctions was first

observed in studies of electron transport[44,45]. The photocurrent served as a probe for spatial mapping of local built-in field and carrier transport in the device. Researchers found that graphene's Fermi level was pinned by the metal at the interface, while the off-interface doping is dependent on the gate voltage applied. Hence an electrically tunable built-in field at the edge is introduced, as shown in Fig. 2.2.

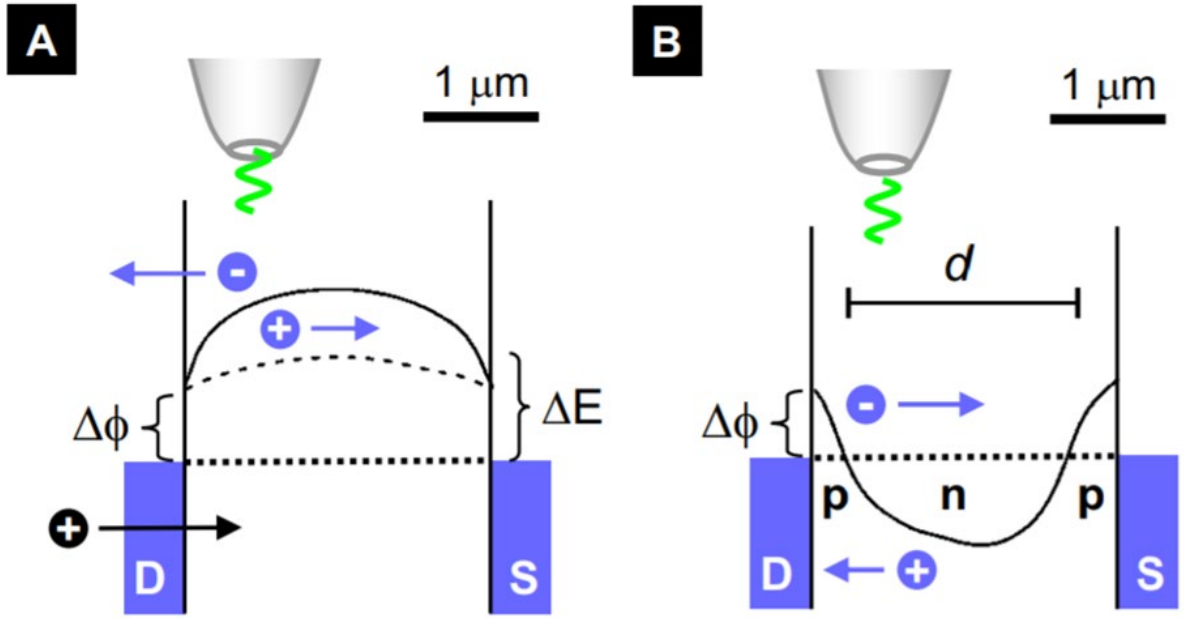

Figure 2.2. Built-in electric field profile of a graphene transistor with metal contacts. (A) and (B) show the cases with different channel doping with the back gate. A sign-flip of photocurrent was observed[45].

The graphene-metal structure was more intensely studied later as photodetectors, especially for the IR band[46,47,48,49]. The responsivity is around several mA/W. The relatively low responsivity is not a surprise, with only a few percent of light absorbed in the monolayer. Such detectors' benefit is an enormous bandwidth exceeding 40 GHz, with an intrinsic limit above 500 GHz[49]. The value is limited majorly by the devices' RC product, while the charge transfer and carrier relaxation allow a higher speed exceeding 1.5 THz.

A photocurrent can also be observed when the graphene transistor works in the photoconductive mode[50]. The responsivity was around 1 mA/W at 1V source-drain bias. Multiple mechanisms contribute to the photocurrent, including photovoltaic, photo-thermoelectric, and bolometric

effects. The dominant effect depends on the gate voltage, source-drain bias, and as later pointed out, the light source's power.

Some other works take the approach of vertical separation of hot carriers through graphene heterostructures[51]. A responsivity of 0.1-1 A/W is achieved at NIR using a TMDC-graphene-TMDC heterojunction.

2.3.2 Photogating in Graphene-Based Phototransistors

The photovoltaic detectors show limited responsivity. To increase the response, researchers utilize the photoconductive gain[52] in device design. We start with a photoconductive detector under illumination. Electron-hole pairs are generated and separated by the electric field. Due to the material and device properties, one type of carrier (electrons, for example) leaves the sample quickly, while the holes move slower and remain in the sample for a longer time. Charge conservation in the device requires additional electrons to flow into the device. Hence multiple electrons have to be driven through the device before a single hole ultimately leaves the sample. This process produces multiple portions of photocurrents with each portion of electron-hole pairs generated. The photoconductive gain is defined as the ratio between the slow carrier lifetime and the fast carrier's transit time across the sample:

$$G = \frac{\tau_{lifetime}}{\tau_{transit}} \qquad (2.2)$$

This equation indicates a gain-bandwidth product. Any effort to increase the responsivity in a similar device would generally lead to a slower operating speed. However, graphene-based IR detectors benefit from an ultra-broad bandwidth. In principle, the responsivity can be boosted considerably with a tolerable speed for many applications.

The first effort in building graphene phototransistors for IR detection was in a hybrid structure with quantum dots (QDs)[53]. The QDs are the active optical absorber and electron trap to produce the photogating effect. The device has a responsivity of 10^7 A/W at NIR, with a response time of hundreds of milliseconds. The QDs have strong optical absorption at NIR but cannot efficiently generate hot carriers at longer wavelengths. Our group conducted another work that replaced the QD layer with a graphene layer to create a broader-band detection[54]. Fig. 2.3 shows the structure

of the device. It is a phototransistor composed of two layers of graphene. A 6-nm layer of amorphous silicon separates the two layers. When operating the device, the top layer graphene works as the transistor channel, and a source-drain bias is applied. The bottom layer graphene works as a floating gate. When light illuminates the device, hot carriers will be generated on both layers of graphene. Due to the two graphene layers' unequal doping levels, the hot carriers will then transport across the thin silicon layer, which functions both as the gate dielectric and tunneling barrier for photo-generated hot carriers. The interlayer carrier transport creates a net charge accumulation on the graphene layers, changing the conductance of the top graphene channel. The system produces a huge photoconductive gain, boosting the overall responsivity beyond 1 A/W at mid-IR.

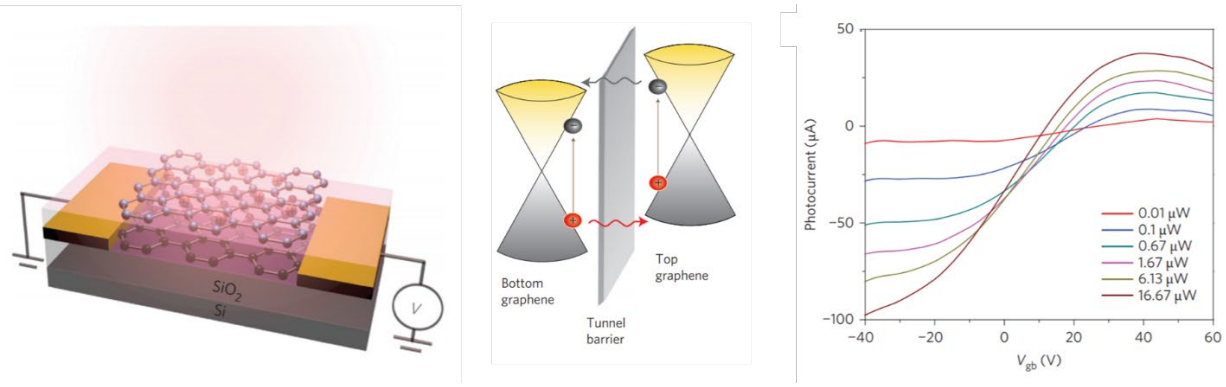

Figure 2.3. Device structure (left), band alignment (mid), and photoresponse (right) of a graphene phototransistor[54].

The speed of the device is limited to 1 sec. The low speed relates to both the gain-bandwidth tradeoff and the defective nature of the dielectric material. The speed can further improve with improved quality of tunneling barrier materials[55].

2.3.3 Photo-Thermoelectric Detectors

The photo-thermoelectric effect (PTE) dominates the photoresponse of many graphene devices. The origin of the response is a diffusion-based process. After the photo-excitation in graphene, the generated hot carriers show temperature and density gradients in positions with broken inversion symmetry. Hence the carriers diffuse based on the density gradient. If electrons and

holes are not diffusing at the same pace in the same direction, the electrons and holes are partially separated, creating a photoresponse from the graphene structure. The strong photo-thermoelectric effect in graphene comes from two reasons: The low thermal capacity of electrons in graphene and their slow coupling to the lattice enable them to be heated to high temperature at low optical power. The high carrier mobility enables a large diffusion coefficient, as determined by Einstein's relation.

In some of the works, the thermoelectric part of the process is attributed to the Seebeck effect. It describes the generation of electromotive force built up under a temperature gradient. The short-circuit thermal current equals[56]:

$$I_{therm} = \frac{(S_2 - S_1)\Delta T}{R} \quad (2.3)$$

where R is the resistance of the device. S_1 and S_2 are Seebeck coefficients of different regions, as required by the broken symmetry. ΔT is the temperature gradient. The Mott relation defines the Seebeck coefficient[57]:

$$S = -\frac{\pi^2 k_B^2 T}{3e} \cdot \frac{1}{G}\frac{dG}{dE} \ (E = E_f) \quad (2.4)$$

with *G* representing the conductance of the material.

The conductance of the material is tunable in graphene with changed Fermi levels. Hence a Seebeck coefficient difference is accessible in a single material via non-uniform electrostatic or environment doping. Seebeck current is reported in partially[58,59] or fully[60] illuminated graphene p-n junctions and graphene mono-double layer junctions[61]. It also plays an vital role in photocurrent generation at metal-graphene interface[50,59], though the dominating mechanism varies depending on the illumination type (CW or pulsed), illumination power, and sample preparation.

Another type of PTE is also reported in graphene-metal junctions when a pulsed laser illuminates the device. The photocurrent peaks at a metal-graphene junction[62]. Contrary to the current generated due to the Seebeck coefficient difference inside graphene, the photocurrent does not change its direction with different doping. The response originates from the lateral photo-Dember effect[16]: After the hot carrier generation, the electrons and holes diffuse due to the density gradient near the metal contact. The mobility of electrons and holes should be equal, as

required by the symmetric band structure. However, impurity and surface scattering cause a difference, which is further amplified by the large absolute values of mobilities in graphene. The hot electrons and holes diffuse at different speeds to the metal contact, creating a transient photocurrent. The photo-Dember effect also points to a large transient dipole at the junction. Since the hot carrier dynamics lie in the THz regime, this points to a novel THz generation process. A similar photocurrent is later demonstrated in a patterned graphene layer, with spatial inverse symmetry broken by the edge[63].

2.3.4 Bolometers

The carrier's low heat capacity also opens opportunities for bolometer-type devices working at high frequencies. Graphene bolometers, with single-layer graphene[64] and gated double-layer graphene[65], are demonstrated with a working frequency exceeding 1 GHz at cryogenic temperature. One recent work realized room temperature IR photodetection with a responsivity of 16 mA/W at 12 μm wavelength[66]. It is realized by integrating graphene plasmonic structures with graphene nanoribbons. The plasmonic part enhances the near-field electromagnetic energy intensity, with the graphene nanoribbons acting as a bolometer. The tradeoff is complex sample preparation as well as a limited bandwidth.

2.3.5 Enhanced Light-Matter Interaction: Optical Design

Graphene photodetectors suffer from an inherent disadvantage: though the light-matter interaction is strong when normalized to a single atom, the total absorption is only a few percent in the monolayer. Multiple solutions were proposed to enhance the light-matter interaction. Some works make light pass through the graphene layer multiple times with microcavities[67] or crumpled graphene[68]. Another approach utilizes the near-field enhancement effect of surface plasmons. The plasmons are excited either with metal structures[69,70,71] or patterned graphene layers[6]. On the other side, integration with on-chip waveguides also increases the interaction strength, as light propagates along the graphene surface rather than perpendicular to it. More

importantly, this approach fully utilizes the potential of ultrafast operation of such detectors for high-speed integrated photonics applications[71,72,73,74].

2.3.6 Summary

In conclusion, graphene's gapless band structure, strong light-matter interaction, and unique hot carrier dynamics enable broad-wavelength-range, high-speed photodetection. However, unconventional device design strategies are necessary to overcome the low absorption and low quantum efficiency. The table below summarizes the performance of different graphene-based photodetectors.

Table 2.1

Mechanism	Wavelength Range	Responsivity	Speed	Note
Photovoltaic	Vis-NIR[46-50]	~1 mA/W	> 500 GHz	
	NIR[11]	0.1-1 A/W	~ 10 kHz	Graphene-TMDC heterostructure
Photogating	NIR[53]	10^7 A/W	~1 Hz	Graphene-QD heterostructure
	Vis-MIR[54]	> 1 A/W at 3μm	~1 Hz	
PTE	Vis-MIR	~20 mA/W at 630 nm[63]	>1 THz	Best performance given by photo-Dember effect
Bolometers	MIR-FIR	16 mA/W at 12 μm[66]	> 1 GHz	FIR operation is under cryogenic conditions

2.4 Graphene THz Emitters

THz electromagnetic waves feature unique interactions with materials in comparison with other bands of interest. THz time-domain spectroscopy and THz imaging techniques are useful for chemical detection through a decent penetration depth. Hence applications such as security check demand efficient THz sources.

The picosecond-scale hot carrier dynamics in graphene point to not only photodetection but also THz emission. Many different techniques are applied to generate THz signals using graphene structures. In most techniques, the graphene layer is driven to non-equilibrium with a laser pulse. Then the hot carrier dynamics create transient dipoles. These dipoles emit THz pulses. The exact mechanisms include the PTE effect in graphene[75], quantum resonant tunneling in a graphene Esaki diode[76], photon drag effect[77,78] and coupling to THz plasmon from thermal emission[79] or laser in a waveguide[80]. Though graphene is a promising candidate of THz sources, such sources' industrial application has to be motivated by a significant improvement in performance compared with existing products, which is still absent.

Chapter 3
Instrumentation

3.1 Introduction

Understanding ultrafast hot carrier dynamics in graphene and related devices requires comprehensive characterization tools. This chapter introduces the electrical and optical measurement instruments used in Chapter 4-6. Section 3.2 introduces electrical instruments for room-temperature and cryogenic measurements. Section 3.3 introduces the light sources used to illuminate the devices. In Section 3.4 and 3.5, we introduce two optical setups for time- and space-resolved characterization.

3.2 Electrical Instruments

The electrical signals were applied to and extracted from nanodevices with the tools shown in Fig. 3.1. Several micro-positioners with tungsten pins were mounted on a room-temperature probe station and a low-temperature probe station. The micro-positioner and the probe station connect samples to the measurement equipment. A microscope system is mounted on each probe station for precise control of the probes. The low-temperature station supports temperature-dependent measurements from 5 K to 350 K, which is a powerful tool for carrier transport studies.

The probe stations are not perfectly compatible with our optical setup for many tests. For some optical measurements, we mount the sample either on an Oxford cryostat or a 24-pin game card socket. Devices were wire-bonded to a chip holder with gold pads. The pads were connected to either of the two setups. The cryostat provides excellent grounding and a very stable mount with

negligible position drift. However, it is bulky when integrated with optical setups and does not support double-sided illuminations for transparent samples. Hence, we developed the game card socket setup for the transparent photodetector project. It is then used on the THz pump-probe measurement as well.

The unpackaged nanodevices are fragile to electrostatic discharges, which happens regularly in wire-bonding and testing operations. To solve the problem, all measurement equipment, as well as the researcher, are grounded. Wearing cotton and linen during measurements also reduces device burning, since the two materials tend to remain charge-neutral. In wire-bonded samples, a switch box is attached to the device, shifting between GND and ON states during measurements. The switch box further protects the nanodevice from discharges. It connects the device either to the ground or to the ADC/DAC ports throughout the measurement.

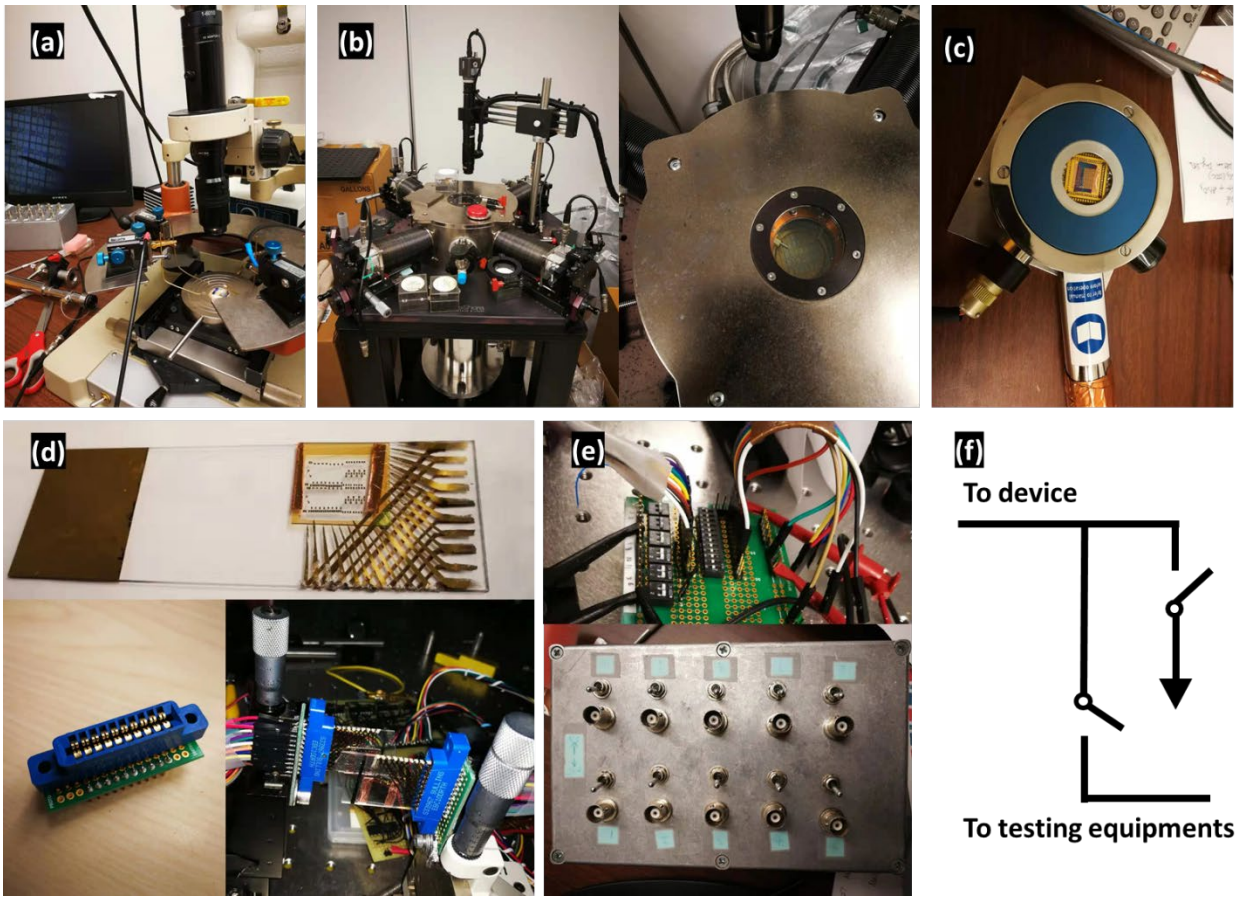

Figure 3.1. Room temperature (a) and low temperature (b) probe stations with micro-positioners. Samples can also be wire-bonded with a cryostat (c) or a game card connector (d). Grounding switches (e)(f) were applied to reduce damage due to electrostatic discharges.

The data collection toolkit is shown in Fig. 3.2. It includes a DAC/ADC card, a pre-amplifier, a lock-in amplifier, and a motorized micro-stage controller. All tools are controlled via LabVIEW programs on the PCs.

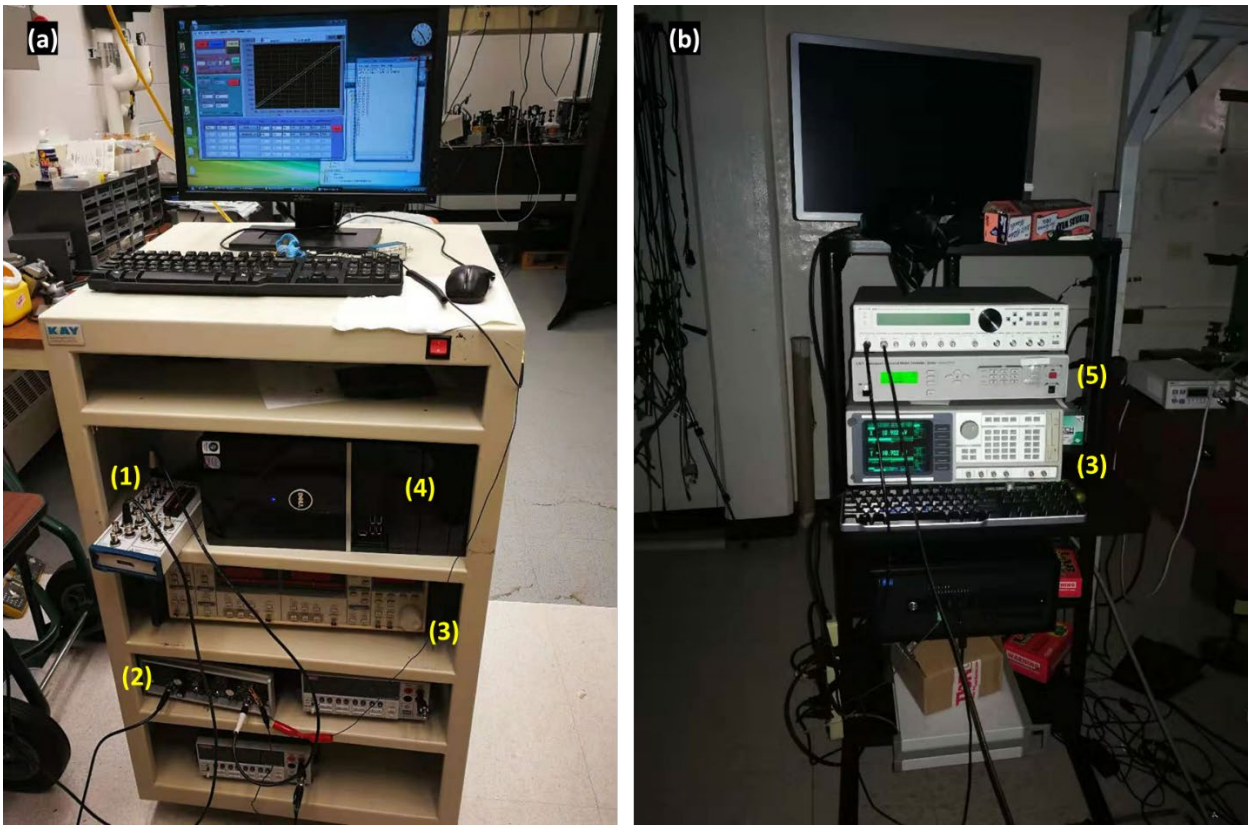

Figure 3.2. Figure of the data collection carts. (1) DAC/ADC card; (2) pre-amplifier; (3) lock-in amplifier; (4) PC; (5) motorized micro-stage controller.

3.3 Light Sources

Several light sources are used for light-matter interaction studies: A Coherent Verdi V10 laser (532 nm) is used for optical alignment and simple photo-response test. It is also used as the pump for a Ti:sapphire (model Mira 900) laser working at 800 nm. The Ti:sapphire laser works at either continuous wave (CW) mode or mode-locked mode. At mode-locking condition, the pulse width is below 100 fs, sufficiently short for our time-resolved measurements. For NIR photoresponse with more wavelengths, optical parametric amplification (OPA) is applied. A Ti:sapphire laser (Coherent RagA 9000) pumps the OPA, generating a signal and an idler. Both beams are used as light sources illuminating the sample. The single and idler peaks at the

frequency domain were tuned between 1.1-2.4 μm. With filters mounted in front of the device, this works as a light source with tunable NIR wavelengths.

3.4 Scanning Photocurrent Spectroscopy

As discussed in Chapter 2, the spatial distribution of photocurrent is essential. It unveils important clues for understanding the light-matter interaction mechanism. In our work, the measurement is performed using the setup shown below:

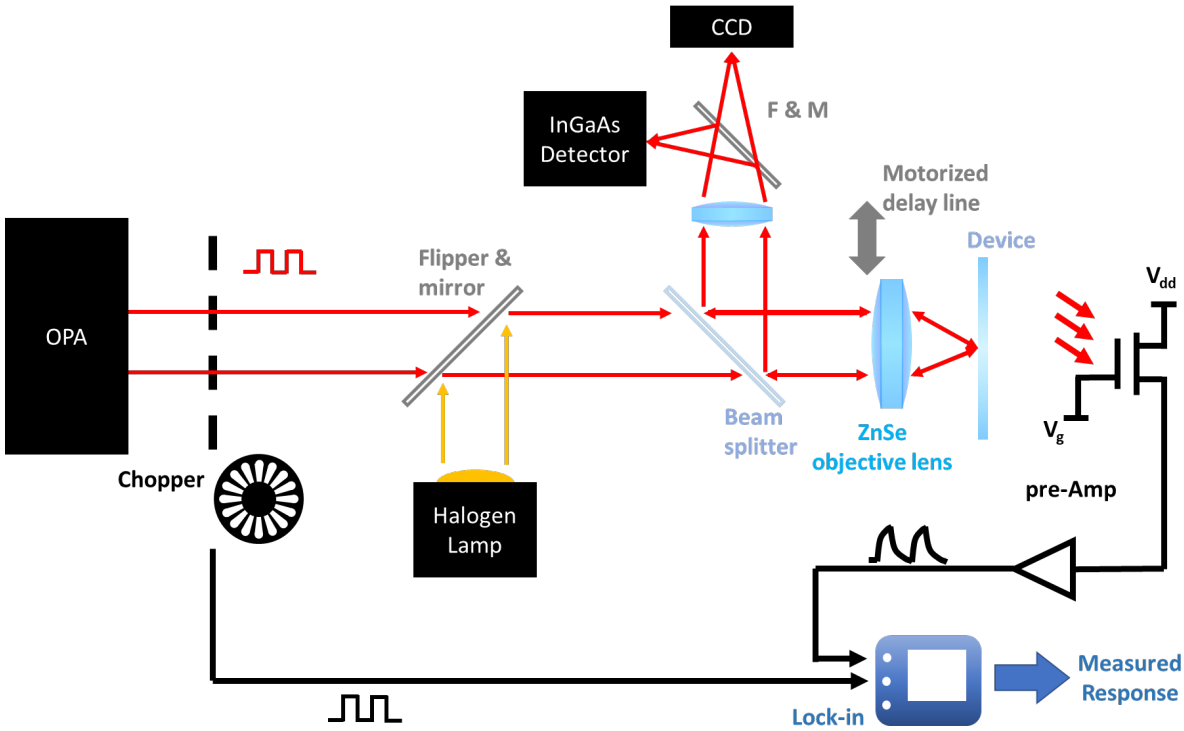

Figure 3.3. Optical and electrical setup for scanning photocurrent spectroscopy.

We use a chopper to modulate the pump beam for some of the measurements. The modulated signal is collected and processed with a lock-in amplifier. This helps to increase the signal-noise ratio in the measurement. The lamp and CCD camera work as a microscope system, which helps to optimize the beam quality and align the beam to the targeted area. The device is wire-bonded and mounted on either the cryostat or the game card socket. For scanning photocurrent spectroscopy, a 2D motorized stage is used to move the objective lens. The LabVIEW program

synchronizes the measured signal with the position of the stage. For the 3D camera project mentioned in Chapter 5, a 3D motorized stage is used to move the objective, mimicking a point object that moves in three dimensions.

3.5 On-Chip Pump-Probe Spectroscopy

Fig. 3.4 shows the optical setup for on-chip pump-probe microscopy. The setup is used to study the THz signal emitted from a graphene emitter. The pump beam illuminates the THz emitter. The THz field is coupled to a double metal stripe waveguide. After 100 μm propagation, the signal reaches the Auston switch. The Auston switch is fabricated with O+ implanted silicon. It turns on at a FWHM of 0.7 ps under pulsed illumination, allowing the THz field to be extracted from the waveguide. We can tune the pump and probe beam's time-delay via the motorized delay line at a range of 160 ps. The measured current is a convolution of the THz field and the Auston switch's temporal response.

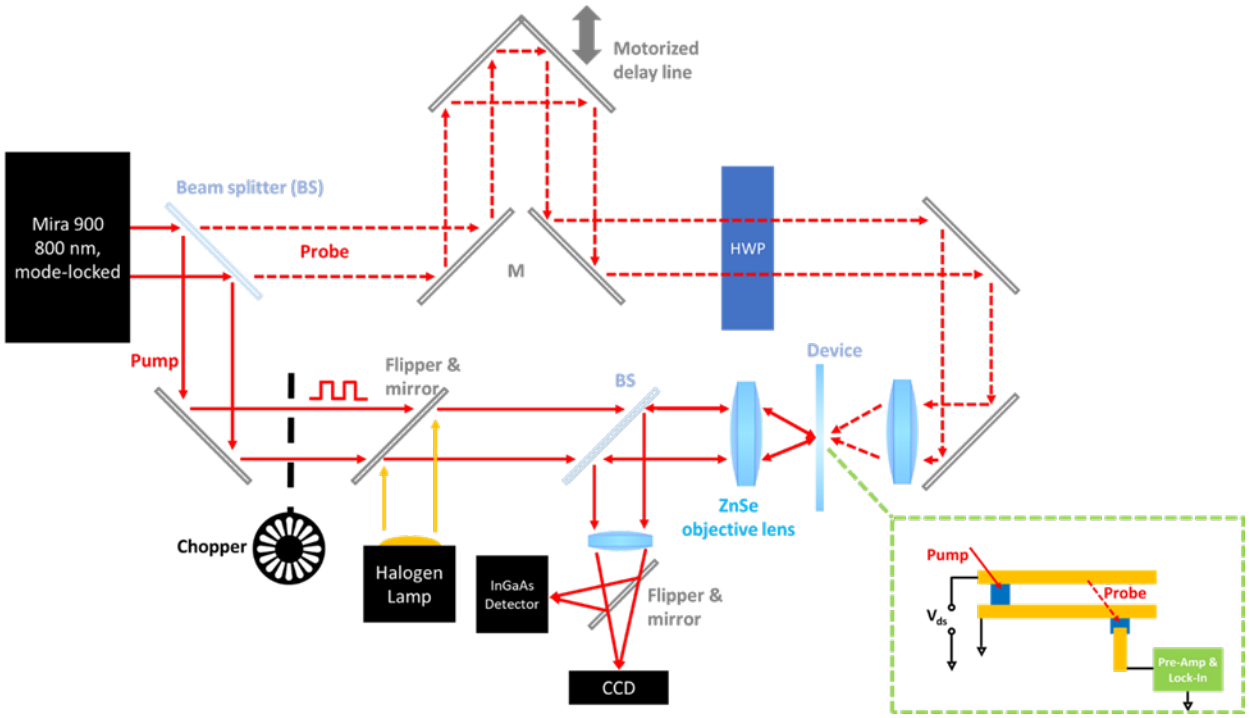

Figure 3.4. The optical setup for on-chip pump-probe spectroscopy. The pump and probe beams hit the sample in opposite directions. A motorized stage controls the time delay between the pump and the probe. Bottom-right: the device structure and operation condition on the chip.

The chopper is placed at the path of the pump beam because the graphene emitter is highly conductive. Placing it on the probe beam would induce a large background signal in the pre-amplifier, which saturates the preamplifier before reaching the optimum amplification.

In Chapter 6, we apply the pump and probe beams on two sides of a transparent silicon-on-sapphire substrate instead of a more straightforward single-sided setup. This is due to several reasons: For the choice of substrate, we need to minimize the THz absorption by the substrate and need a thin-layer undoped silicon for fabrication of the Auston switch. Hence the silicon-on-sapphire substrate is chosen. It is transparent and made it possible to pump and probe from two sides of the device. Secondly, the sample is studied later with both temporal and spatial resolution by integrating the scanning photocurrent spectroscopy into the setup. To modify the position of only the pump beam while maintaining a decent beam quality, we applied motorized stages to control the objective lens position. The objective lens of the two beams must be decoupled to make it work. As a result, double-sided illumination is a good choice.

Chapter 4
Spectral Information Extraction from a Graphene-Based, Electrically-Tunable Phototransistor

4.1 Introduction

As mentioned in previous chapters, many graphene photodetectors were reported covering the visible to FIR range. However, the industrial applications of the detectors are still limited by the factors discussed. For further motivating the industrial applications, we target functionalities beyond simple photodetection. One approach is to extend the photodetection to spectral detection with our graphene phototransistors.

Optical spectroscopy, including FTIR and Raman spectroscopy, are powerful tools to study the microscale structure and chemical composition of materials. The light-matter interactions give essential clues on atomic/lattice oscillations, orbit/band transitions, and dielectric properties. In recent years, the miniaturization of spectroscopy hardware has become a growing demand, as it helps lower the cost and extend the possible applications of optical spectroscopy.

Some works report coin-sized spectrometers by stacking optical filters on an imaging array[81,82,83,84]. Others took the approach of integrating photodetectors with chip-scale filters[85], interferometers[86,87] or resonance structures[88,89]. The readouts in these spectrometers are often not a directly observed spectrum. Computational methods can convert the readout into measured spectra. The technology is sometimes termed computational spectroscopy[5,83,86]. Another strong candidate in on-chip spectroscopy comes from the recent advances in integrated photonics. Frequency combs with high resolution have recently been demonstrated[90,91,92]. These designs further lower the cost of spectroscopy by either lowering the requirements for filter preparation or miniaturizing the system to chip-scale. The lower expense and portability potentially make

spectrometers more accessible to biosensing[93] and chemical detection[94,95] applications. However, neither of the solutions could further reduce the device footprint to a few micrometers. The computational spectroscopy approach requires a larger number of pixels with different spectral responses for better accuracy. On the other hand, the integrated photonics approach's footprint is limited by the scale of key components such as waveguides and ring resonators.

This chapter introduces a new approach with a graphene-based photodetector with a tunable responsivity. We find that with different gate voltage applied, its responsivity shows different spectral dependence. The corresponding computational method is applied to the data to give a preliminary demonstration of spectral information retrieval from the device. This opens the possibility of using such kind of tunable photodetectors to build ultra-compact, on-chip spectrometers. After further performance improvement, the device can be built into arrays as a low-cost, on-chip multispectral camera.

4.2 System Overlook and Device Fabrication

Fig. 4.1 (a) illustrates our device design. A graphene-based photodetector absorbs light and produces a photocurrent. A control voltage (V_g) can be applied to the device, so that the photocurrent changes. The control voltage changes the photocurrent differently when the light source is of different wavelengths. This feature encodes the spectral information in the photocurrent-voltage dependence. A personal computer documents the photocurrent-voltage dependence. A spectral reconstruction algorithm then processes the data into a measured spectrum.

Graphene is the chosen photodetection material for its broad-band absorption from visible to microwave[96,97]. This is a giant advantage over traditional optoelectronic materials, whose responsivity is limited by the absence of well-controlled inter-band or inter-state transitions at long wavelengths. We choose the graphene phototransistor, since it provides a large, broad-spectral-range photoresponse with a strong gate tunability.

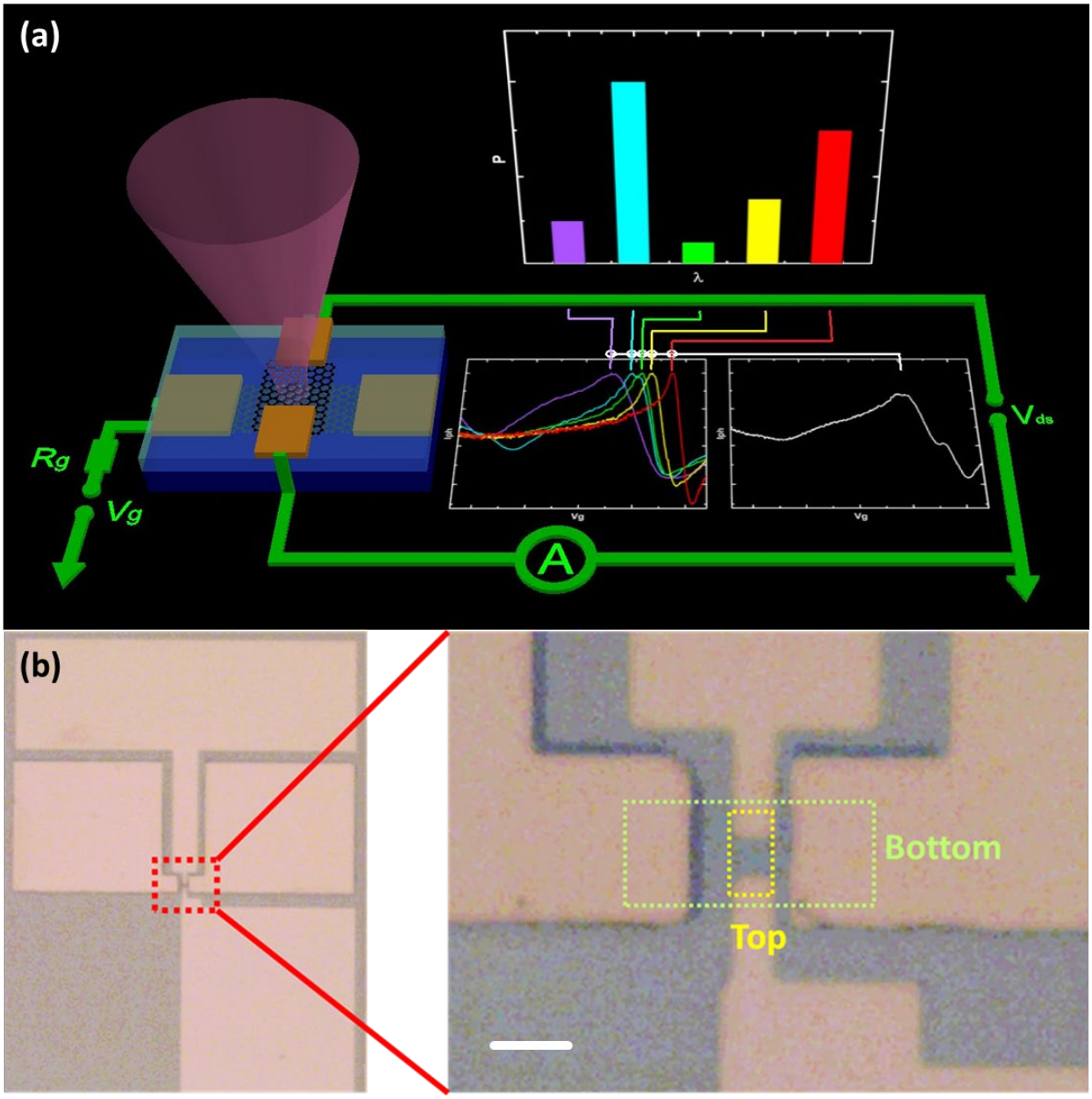

Figure 4.1. (a) Schematic illustration of how such kind of device potentially works as a spectrometer. When illuminated by light with some arbitrary spectrum, the device produces a photocurrent curve under sweeping gate bias. The shape of the curve varies for different wavelengths. With a least-square linear regression algorithm, this curve can be converted to the reconstructed spectrum. (b) Microscopic photograph of the device structure, scale bar: 10 μm.

Our device is a graphene phototransistor composed of two layers of graphene. We introduced the device structure and the photogating effect in Section 2.3.2 for our prior work. Instead of floating the gate layer, which is the case in the previous works, we apply a bias on the gate. The gate voltage makes the tunneling barrier electrically reconfigurable.

The devices are fabricated on a silicon substrate. We first deposited a 5-nm / 50-nm/ 5-nm Ti/Pt/Al layer. The titanium layer serves as the adhesion layer. The aluminum layer's surface oxidizes in air and enhances the quality of subsequent ALD-grown gate dielectric. We then used ALD to grow an 85-nm layer of Al_2O_3, on which we fabricate our device. Such a substrate removes possible photoresponses from the silicon substrate (see photocurrent measurements). Then a monolayer CVD-grown graphene is wet-transferred[98] onto the substrate and patterned with photolithography and oxygen plasma etching. Then lithography, metal evaporation (Cr/Au 5/50 nm), and lift-off process define the contact. We sputtered un-doped silicon as the dielectric barrier. Then a top layer of metal-graphene structure is fabricated with similar corresponding processes.

4.3 Spectrally-Resolved Photoresponse

We first perform DC measurements for the photocurrent of our device. We gradually increase the illumination power from darkness and measure the current across the graphene channel. As in Figure 4.2 (a), there is a change in current across the channel when the light was on. This change gives the photocurrent in our phototransistor. In contrast to what was observed before in the device with floated gates, where we observe a simple shift of Dirac point in the transfer curves[54], we find a distortion of the curves with increased power. We qualitatively analyze the behavior through the band diagram across the dielectric barrier when different bias is applied (Figure 4.2 (b)(c)). At flat-band case (gate voltage equals V_{FB}), hot carriers transport to both directions at an equal rate. There is no net charge accumulation, and the photocurrent at V_{FB} is zero; however, when the gate bias deviates from V_{FB}, two mechanisms help to distort the barrier: the gate bias itself creates an electrical field in the barrier; the gating introduces additional doping to both layers of graphene, with the Fermi-level difference between the two layers determined by the gate voltage. This doping contributes to the band distortion as well, which further modulates the carrier transport. The transfer curves' distortion indicates tunability on the carrier transport across the barrier with the gate bias.

The tunability offers a wavelength-dependent photoresponse. The barrier distortion differs with changing gate bias; hence the carrier separation efficiency across the barrier changes. The hot

carriers with energy slightly below the barrier height are of particular interest. Such carriers' transport rate changes drastically when the barrier distorts by hundreds of meV, while a hot carrier with lower energy remains insensitive to this bias change. Since the excitation wavelength determines the hot carrier energy (with exceptions discussed later), the responsivity has different gate-bias dependence at different wavelengths.

To further examine the wavelength dependence, we use an optical chopper and a lock-in amplifier to measure the photocurrent. We focus on the AC photocurrent instead of the DC measurement based on signal-noise ratio and hysteresis considerations (see Section 3.4). We use an optical parametric amplification (OPA) pumped with a femtosecond laser at 800 nm as the light source. The generated wavelength covers through 1.1 μm to 2.4 μm with either the signal or the idler as the source. For 800 nm measurements, we use the pump directly as the light source. Band-pass filters are applied to make the beam monochromatic. For different power, the shapes of the photocurrent curves are similar at the same wavelength. For different wavelengths, the shapes of curves become different (Figure 4.2 (d)(e)). Figure 4.2 (d) shows how the photoresponse evolves with respect to different wavelengths. The curves are normalized with their peak values. When the incident wavelength is longer, both the peak and the zero points of the curves shift from left to right. Furthermore, if we evaluate each curve's curve peak width, we see a continuous decrease from left to right. Another feature is the increase of the absolute value of the ratio between the negative and positive peaks. This continuous evolution of the curves' features certainly indicates a robust difference in the photoresponse for different wavelengths.

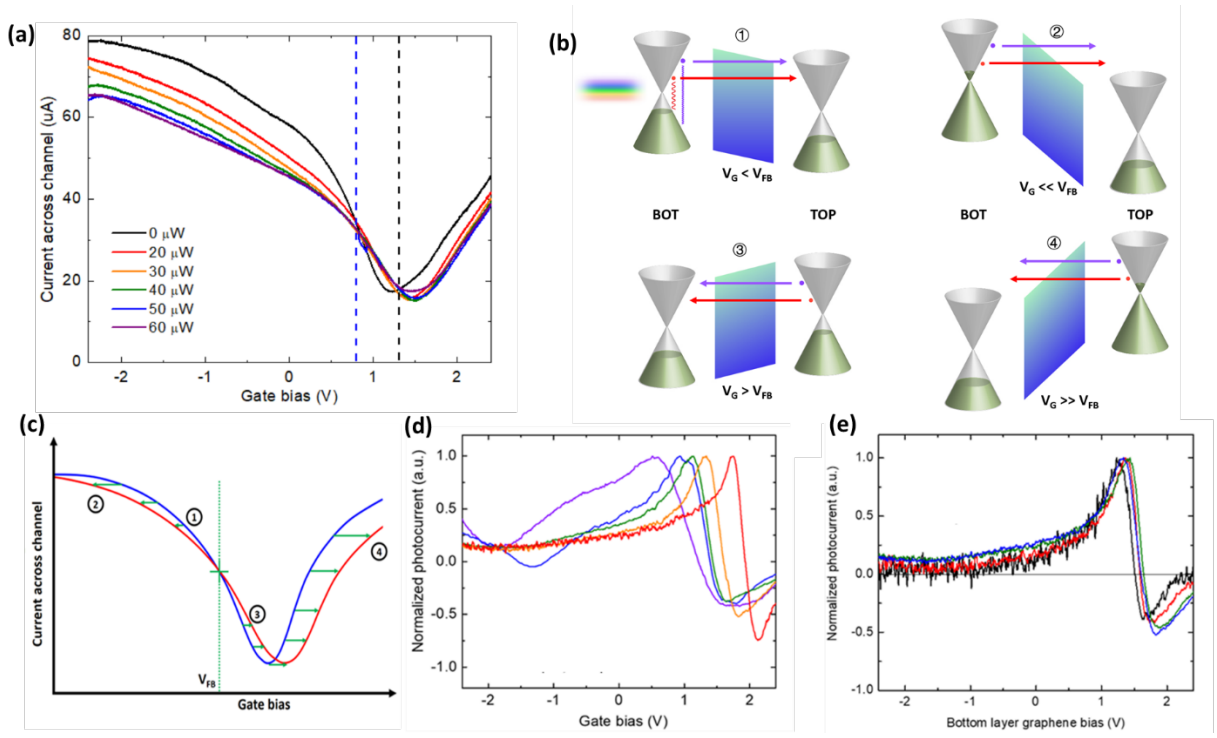

Figure 4.2. DC and AC photoresponse. (a) DC measurement of how the device's channel current changes under different illumination power. The incident wavelength is 1.3 μm, and a gate bias was applied to the bottom graphene layer. Black: curve measured in darkness; Red to purple: under the power of 20 μW, 30 μW, 40 μW, 50 μW, and 60 μW. (b) Band diagram of the graphene – silicon – graphene heterojunction under different gate bias. Red and purple arrows represent hot electrons carrying different photon energy. (c) A qualitative sketch of the photoresponse behavior predicted by the model described in (b). (d) Photocurrent of the device under different wavelengths, purple to red: 0.8 μm, 1.2 μm, 1.5 μm, 1.9 μm and 2.2 μm. (e) Photocurrent of the same device at the same wavelength (1.9 μm) but different power. The curves are normalized by their peak value for comparison of their shapes. Black: 200 μW, red: 300 μW, green: 400 μW, blue: 500 μW.

4.4 Computational Spectroscopy: Algorithms

The additional gate voltage expands the device's readout from a scalar to a dual-vector (the gate-responsivity curve). Moreover, the shapes of such V_g - I_{ph} curves differ for different incident wavelengths. This indicates that the spectral information is encoded inside the dual-vector. It potentially allows spectral reconstruction from the readout of a single device. To extract the spectral information from the vectorized photocurrent of an unknown light source, we applied a computational method similar to the previous works[83]. The spectral reconstruction process is modeled as matrix manipulations in a linear system. First, we linearly map the gate-dependent photocurrent vectors to the spectrum. A set of N_g discrete gate voltages are applied to the device. The device has different responsivities at the N_s wavelength, recorded as a vector for each gate voltage. We place all the vectors abreast and define the $N_g \times N_s$ matrix as M. When light with an

unknown spectrum illuminates the device, the gate dependence of photocurrent (vector *I*) is measured. By linear superposition, the expression of *I* written in terms of *M* and the input spectra *S* is:

$$I = M \cdot S \tag{4.1}$$

A straightforward solution to the reverse problem is to calculate the inverse matrix of *M* and multiply it to both sides in equation (4.1). However, practically M^{-1} can be singular at large matrix sizes and creates overfitting in the results. We adopted the least-square linear regression method instead. This method converts the problem to an optimization task that finds the proper vector *S* to minimize an error function[99,100]:

$$\min_{S} \left\{ \frac{1}{2N} \sum_k \left(I_k - \sum_j S_j M_{jk} \right)^2 + \lambda R(S) \right\} \tag{4.2}$$

The first term in equation (4.2) evaluates the mean square error of a predicted photocurrent compared to the real photocurrent *I*. Initially, the algorithm (run in a PC) generates a random hypothesized spectrum *S*. We sum up the photocurrent contributed by each frequency component to calculate *S*'s corresponding photocurrent. Then we compare the hypothesized photocurrent and the experimental photocurrent by calculating the mean square error of $I - M \cdot S$. At the first iteration, the error is large because the hypothesized spectrum significantly deviates from the actual one. The PC minimizes the error with many subsequent iterations. Each iteration generates a new hypothesized spectrum to reduce the mean square error. The algorithm stops after the error's drop meets a convergence condition. The optimized hypothesized spectrum becomes the reconstructed spectrum. We compare the reconstructed spectrum to the actual spectrum (measured with a commercial spectrometer) to check our device's performance on spectral information detection.

The term with λ and $R(S)$ is the regularizer added to avoid overfitting in the optimization process. Various forms of *R(S)* are available to achieve decent reconstruction accuracy[86]. We choose the LASSO regularizer for single-peak reconstructions with our experimental data since it penalizes wide-band overfittings. For ideal device simulations, we make *R(S)* = 0 (pseudoinverse) to explore the general accuracy-resolution tradeoff without pre-knowledge of the test spectra's properties.

4.5 Spectral Reconstruction: Results and Discussion

Before using the device to test unknown spectra, we first calibrated the M-matrix by illuminating the sample with six different wavelengths (0.8 μm, 1.2 μm, 1.4 μm, 1.65 μm, 1.9 μm, and 2.4 μm). We sweep the voltage for each wavelength and measure the responsivity. Then we do the same gate bias sweep of our device under the illumination of the test spectrum. We use the photocurrent as the *I* vector and reconstruct *S*. Since there are only several wavelengths in our calibration matrix, we have limited resolution in the reconstructed spectra. Unlike the case with multiple quantum dot pixels, we improve the resolution with a two-dimensional interpolation of the M-matrix. The operation is plausible in our device since there is a continuous responsivity evolution when either the gate voltage or the incident wavelength changes.

Figure 4.3 (b) is a comparison between the reconstructed spectra and the actual spectra. We test the performance of the system with six different spectra. Some test examples are of the same wavelengths with the calibration matrix. We used different illumination powers for the measurements to avoid overestimating the performance. These results also give hints on the system performance with illuminations of identical spectra but different power. The reconstructed spectra are decently well separated for different inputs. We are limited by the optical system's large spatial dispersion, so that only such monochromatic examples can be tested.

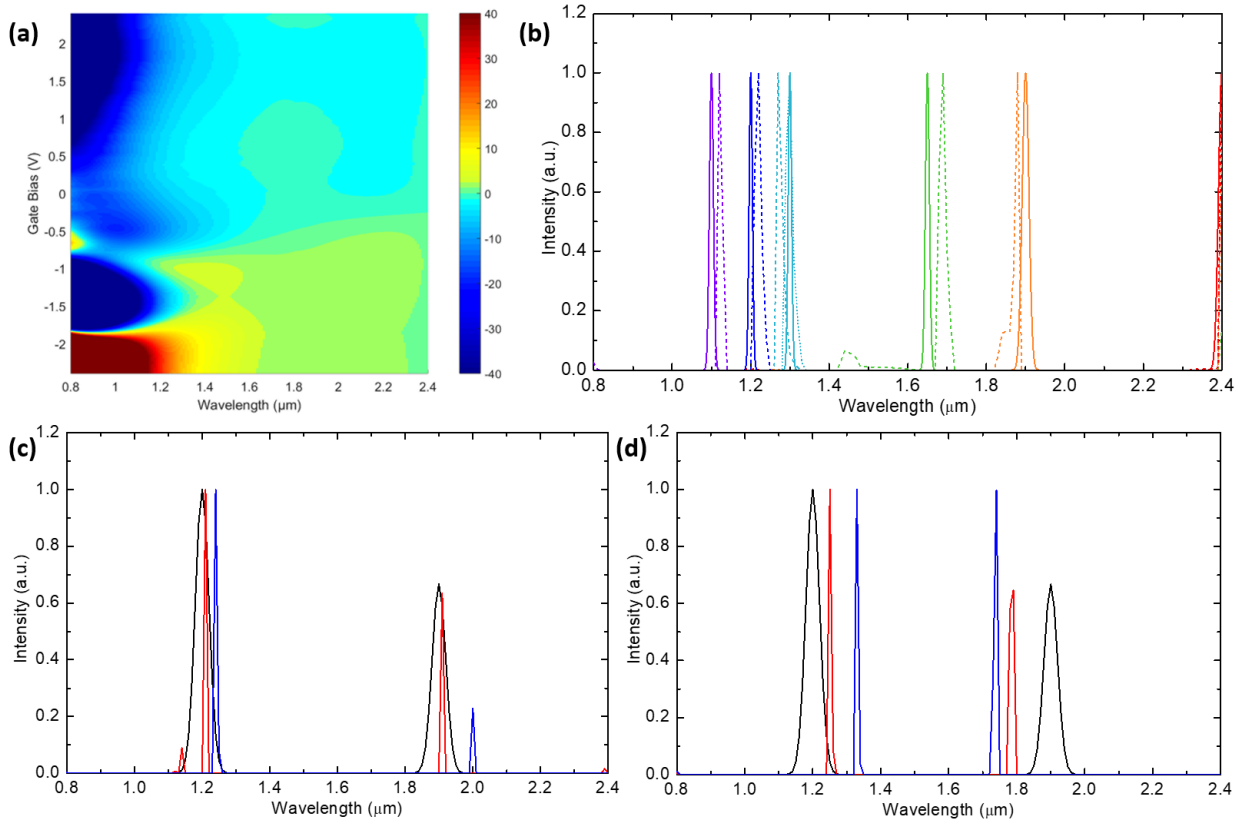

Figure 4.3. (a) AC responsivity of a device (mA/W) after interpolation from experimental data. (b) Reconstructed spectrum normalized with peak value. Solid lines are real spectra, while dashed lines of the same color are reconstructed ones. Influences of noise (c) and hysteresis (d) on the reconstructed spectra are investigated. We first construct some imaginary spectrum, convert it to photocurrent via the measured calibration matrix, then add noise to photocurrent ((c), black: original; red: with white noise equivalent to 1% peak value; blue: 10% peak value) or shift voltage of the curves ((d), black: original; red: shifted left by 25 mV; blue: shifted left by 50 mV). When converting the processed data back to spectra, we get a schematic representation of how noise and hysteresis influence the result.

To explore the reasons that prevent the system from working as a perfect spectrometer, we analyzed the system from both signal processing and device physics perspectives. First, the device suffers from the remaining hysteresis, as shown in Fig. 4.3 (d). Secondly, the photoresponse curves' shape is not precisely unchanged when the power is different (Fig. 4.2 (e)). A pure linear system's responsivity should be independent of the input power, because two photons' contributions to photocurrent should linearly superpose. The mechanisms that contribute to the nonlinearity are summarized in Fig. 4.4. When light illuminates the device, hot carriers are generated in both layers of graphene. Two ultrafast processes are competing: intralayer carrier thermalization and interlayer hot carrier transport. Intralayer carrier transport happens in three phases[101,102,103]: In the first tens of femtoseconds, the carriers quickly

thermalize to a Fermi-Dirac distribution at high temperature. Then the carriers interact with optical phonons and lose most of the energy in 500 fs. Hot optical phonon generation then creates a bottleneck effect and slows down the carriers' further cooling to a few picoseconds. Interlayer carrier transport happens in a time scale between tens of femtoseconds[104] to much longer, depending on the interlayer separation, band offsets, and dominating transport mechanisms. If intralayer relaxation happens much faster than carrier transport, the interlayer carrier transport fails to filter the electrons carrying different photon energy. Hence it is essential to minimize the interlayer transport time. Previous interlayer transport study[105] showed that interlayer transport tends to dominate for extremely thin dielectric layers under a high bias. In that case, Fowler–Nordheim tunneling dominates, especially for carriers bearing photon energy that is slightly lower than the tunneling barrier.

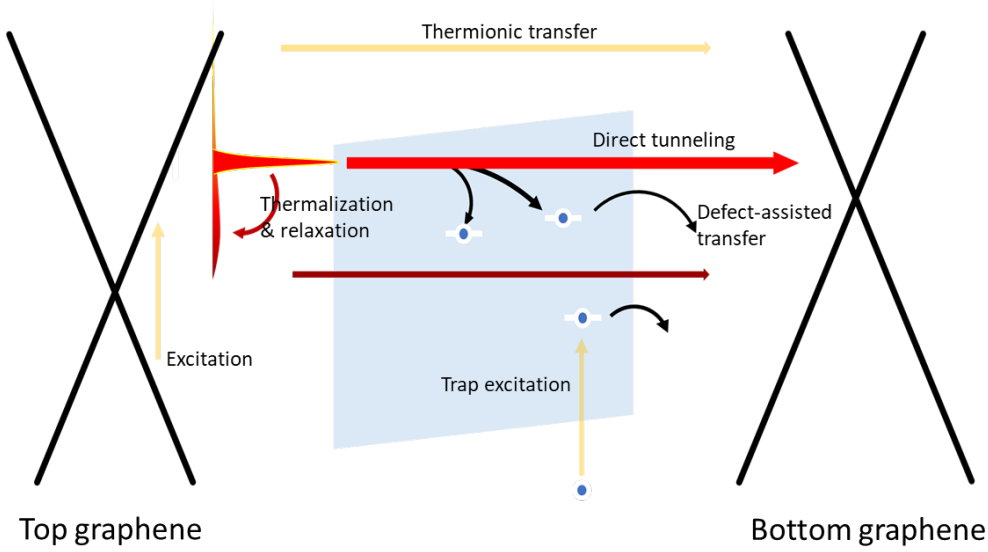

Figure 4.4. Side effects that break the system's linearity, including intralayer carrier relaxation and subsequent thermionic transport, charge trapping in the dielectric layer, defect-assisted charge transport, and photogating effect produced by trap states. These effects compete with direct tunneling (red arrow), reducing the accuracy of spectral reconstruction.

We experimentally examined the carrier transport across the silicon barrier. We used two methods: temperature dependence study of dark carrier thermionic transport[106] and low-temperature tunneling current measurement[107] to extract the barrier height.

When thermionic transport is dominant for the dark carriers, the carrier transport is similar to the case of two Schottky junctions placed back-to-back. In such a case, a reverse-biased graphene-silicon Schottky junction defines the bottleneck for total current flow. The current flow follows the Landauer formalism:

$$J = \frac{q}{\tau}\int_{-\infty}^{+\infty} T(E)D(E)(f_g - f_{Si})dE \qquad (4.3)$$

In a metal-insulator-metal (MIM) junction, the metal part can accommodate or emit unlimited numbers of electrons due to its large density of state (DOS). Contrary to that, graphene has a limited DOS. Hence the equation takes a different form from typical MIM junction when simplified:

$$J = J_0\left(e^{\frac{qV}{\eta k_B T}} - 1\right) \qquad (4.4)$$

$$J_0 = [\frac{qD_0}{\tau}(k_B T)^2(\frac{\Phi_B}{k_B T} + 1)]e^{-\frac{\Phi_B}{k_B T}} \qquad (4.5)$$

We measured current across the silicon barrier at different biases from 5 K to 350 K. Fig. 4.5 (a) shows the modified Arrhenius plot at different biases across the barrier. It is linear at room temperature and above. At low temperatures, the direct tunneling between the two graphene layers dominates over the thermionic transport. With a linear fit at high temperatures, we extract the barrier height to be around 150 meV. The value is significantly lower than 250 meV to 500 meV for realistically p-doped graphene.

We explore the barrier height using another method for comparison: at 0K, FN tunneling dominates the carrier transport. Hence the current-bias relation is:

$$J = (q^3E^3/8\pi h\Phi)\exp\left(-\frac{4(2m)^{\frac{1}{2}}\Phi^{\frac{3}{2}}}{3\hbar qE}\right) \qquad (4.6)$$

The extracted barrier height is 800 meV. The value is higher than work function calculations or previous experimental works.

There is a large discrepancy between the two barrier heights we extracted. We attribute this to the oxidization of the silicon barrier. During fabrication, the silicon barrier is amorphously sputtered onto the bottom graphene layer. Immediately after that, the top graphene layer is wet-

transferred onto the silicon layer. The water and oxygen-rich environment will cause the silicon layer to oxidize, thereby increasing the barrier height. However, the defects in amorphous, partially oxidized silicon create carrier transport pathways at room temperature at an energy much lower than the bandgap. As a result, the barrier height extracted from high-temperature data is lower.

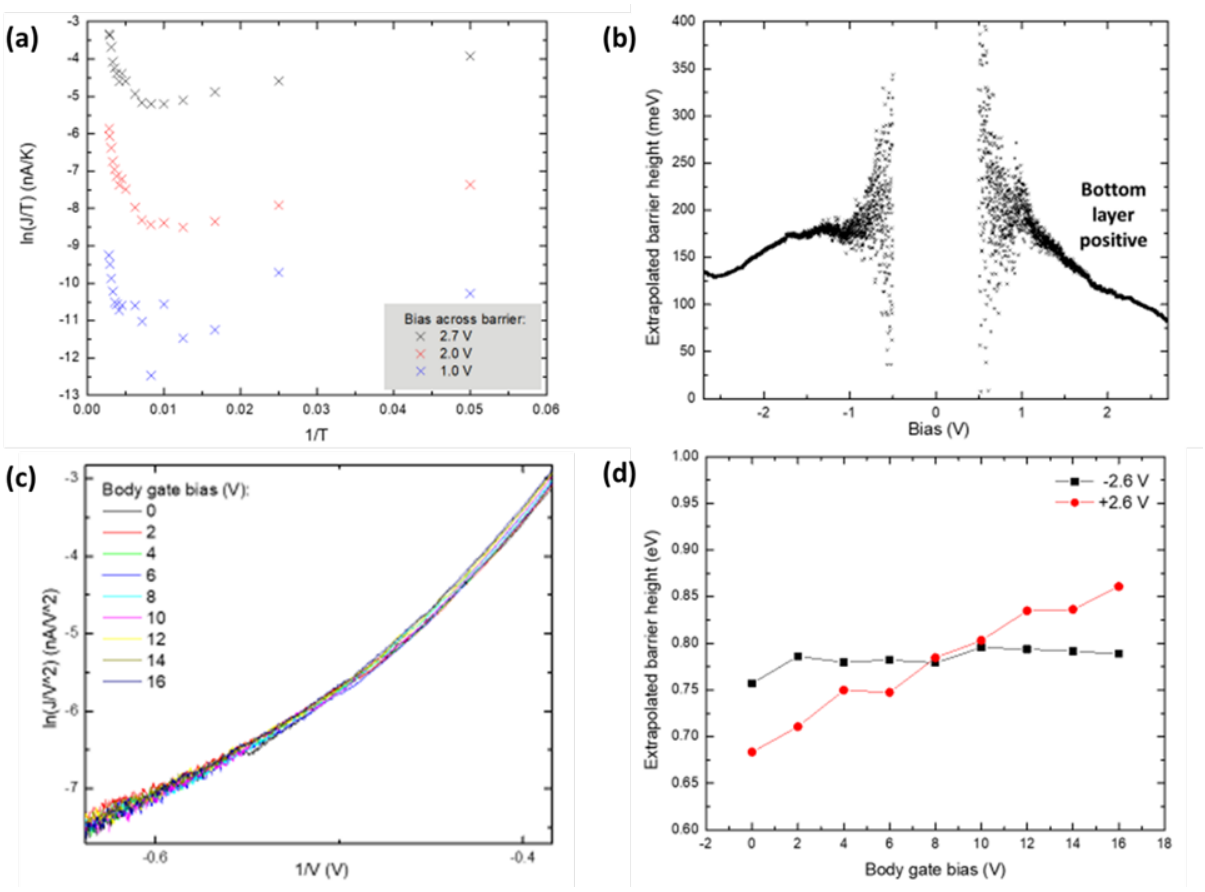

Figure 4.5. Barrier height measurement using thermionic transport model (a) and its bias dependence (b). At 0 K, the FN tunneling model is applied to extract the barrier height (c) and its body gate dependence (d).

The findings, combined with the large hysteresis, indicate abundant trap states in the silicon barrier. The states trap and release charges, exchange momentum and energy with carriers, and assist the interlayer transport. It may also get excited when light is on, creating a small photoresponse. The traps reduce the linearity of our detector's photoresponse, hence preventing it from being a perfect spectrometer.

Possible improvements to minimize the nonideal effects include removing traps and improving the interface qualities through more careful choice of the dielectric and encapsulating materials. Especially, other 2D materials may be an excellent choice, since there have already been many works indicating a high quality of interfaces between these 2D materials[38,39 ,108,109]. One further problem is that we did the interpolation with a limited number of wavelengths. The result can be more precise if we replace the interpolation with more experimental data points.

4.6 Simulated performance of ideal devices

Despite the experimental limitations in the lab, we can use simulations to predict the proposed spectrometer's ultimate performance. Moreover, modeling of the system boosts our understanding of the system and helps to optimize the system.

4.6.1 Band Configuration

First of all, simple order-of-magnitude analysis justifies that the photo-induced Fermi-level change has a negligible effect in band alignments:

The number of photons captured by one layer of graphene (normalized to the area of the device):

$N_{ph} = \frac{\alpha P}{h\nu} = \frac{2.3\% \times 100\mu W}{1eV} = 15$ e-h pairs/ps

For continuous wave light sources, we can estimate the electron-hole pair's generation rate based on a time-average. Consider the number of electrons in a $5\mu m \times 5\mu m$ graphene channel:

$$n = \frac{\sigma}{e\mu} = \frac{10^{-3}S}{1.6 \times 10^{-19}C \times 10^{4}cm^2V^{-1}s^{-1}} = 0.6 \times 10^{12}cm^{-2}$$

So that the number of electrons near the Fermi level is $N_e = nA = 1.5 \times 10^5$.

As a result, one e-h pair would have to heat up 10^4 electrons to form the quasi-Fermi level. Dividing the photon energy (~1 eV) to that value, it contributes to a 0.1-meV shift of Fermi energy. This shift is negligible in the band alignment.

This is different from the experimental observations. The aforementioned experiments and previous works were performed either with femtosecond laser or supercontinuum laser[105], which is not CW. The instantaneous power is orders of magnitude higher. Secondly, the pulse beam is typically diffraction-limited. It creates a high photon flux at a small range. For natural light photodetection, the device illumination is far less intense. Direct exposure to sunlight has an irradiance of roughly 1000 W/m^2. If focused by a lens with 5 mm diameter to and 5mm focal length (sun angular diameter = 0.5 degrees, projection diameter = 44 μm), the power is 20 mW. For a single pixel, the optical power is about 330 μW. The typical studio illumination is one or two orders of magnitude weaker.

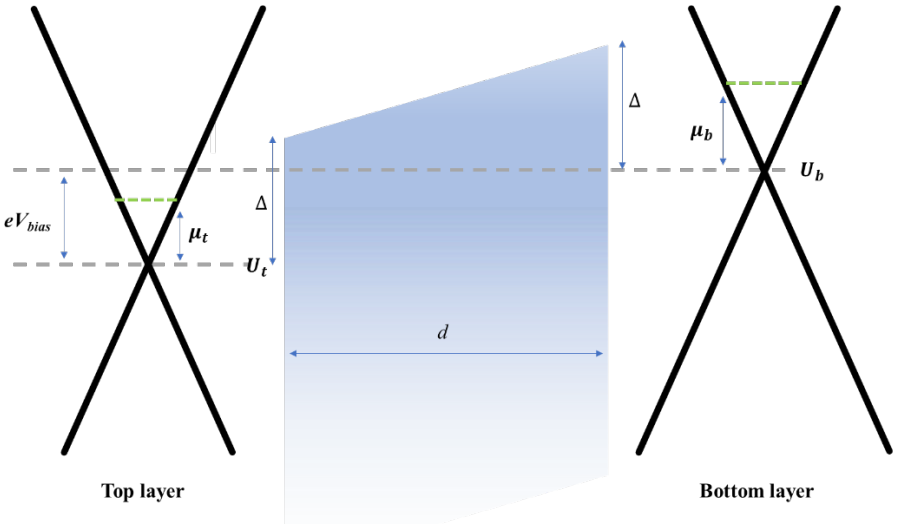

Figure 4.6. Band alignment of the system. For the initial band structure, assume a very high hole barrier, so that the electron transfer processes dominate.

Assume the initial doping profile of μ_t and μ_b at zero bias. The total number of electrons is 0 when the chemical potential falls on the Dirac point ($\mu = 0$). So that we have $n(\mu)$ given by:

$$n(\mu) = \int_0^\infty DoS(E) \cdot f(E,\mu,T) \cdot dE - \int_{-\infty}^0 DoS(E) \cdot [1 - f(E,\mu,T)] \cdot dE \qquad (4.7)$$

$$DoS(E) = \frac{2E}{\pi(\hbar v_F)^2} \qquad (4.8)$$

$$v_F \cong 8 \times 10^5 \frac{m}{s}, \hbar v_F = 0.53\ eV \cdot nm$$

The hole term is written this way to allow good convergence at infinite energy for numerical simulation. Under gate bias V_{bias}, there are extra charges Δn on two layers. The extra charge density follows:

$$\Delta n_b = -\Delta n_t = C(V_{bias} - \frac{\Delta\mu_b - \Delta\mu_t}{e}) \qquad (4.9)$$

We can solve Eq. 4.7-4.9 for the new chemical potentials at any given V_{bias}.

4.6.2 Direct Tunneling and Thermionic Transport

Here we assume electron transport dominates. If hole transport dominates, there will be additional sign-flips of U_t and U_b in the brackets in Eq. 4.10.

The transmission rate follows the equations for different electron energies[110]:

$$Tr(E) = \exp\left[-\frac{\alpha d}{U_t - U_b}\left((\Delta + U_t - E)^{\frac{3}{2}} - (\Delta + U_b - E)^{\frac{3}{2}}\right)\right] \quad if\ (E < \Delta + \min(U_t, U_b))$$

$$= \exp\left[-\frac{\alpha d}{abs(U_t - U_b)}\left((\Delta + \max(U_t, U_b) - E)^{\frac{3}{2}}\right)\right] \quad if\ (\Delta + \min(U_t, U_b) < E < \Delta + \max(U_t, U_b))$$

$$= 1\ if\ (E > \Delta + \max(U_t, U_b)) \qquad (4.10)$$

$\alpha = \frac{4\sqrt{2m_{eff}}}{3\hbar} = 3.2\ eV^{-\frac{1}{2}} \cdot nm^{-1}$, taking the typical value of effective mass to be 1/5 of the electron mass.

And for total transport current, we have (Fermi's Golden Rule):

$$I \propto \int_{-\infty}^{\infty} Tr(E)Dos(E - U_t)Dos(E - U_b)[dist(E, U_t, \mu_t, T_t) - dist(E, U_b, \mu_b, T_b)]\, dE \qquad (4.11)$$

We used this formalism instead of the well-cited one used in the Tsu-Esaki model[111], since the vertical velocity is not well-defined for a 2D material. A state-transition model better describes the process. There is an uncertainty of the absolute value of the current, which we will further discuss later. The function *dist* is the electron energy distribution for the top and bottom layers:

$$dist(E, U, \mu, T) = f_{FD}(E - U, \mu, T) + G_{ph} \qquad (4.12)$$

The second term is the extra contribution before the electron fully thermalizes. If tunneling before thermalization dominates, and multiple times of tunneling back-and-forth is negligible, then we have a simplified version of it: $G_{ph} = \gamma P \delta(E - U - \frac{h\upsilon}{2})$. This means we simplified the largely un-thermalized electrons to hold the same photon energy, with the pre-factors determined by absorption coefficient and illumination power.

The most important issue is the dominant mechanism: If thermionic transport after thermalization dominates, then the carrier transport is not linear. If tunneling before thermalization dominates, then the carrier transport is linear. Then it is an ideal device for spectral reconstruction. We first estimate the temperature of the electrons. Assuming constant lattice temperature, there is an energy balance between illumination and dissipation. Hence, we have the equation:

$$P_c = \frac{\int_{-\infty}^{\infty} E \cdot DoS(E) \cdot f_{FD}(E,\mu,T)dE - \int_{-\infty}^{\infty} E \cdot DoS(E) \cdot f_{FD}(E,\mu_0,T_0)dE}{\tau} \qquad (4.13)$$

The estimated lifetime is ~ 10 ps in previous theory and experiments in the condition we use[43,112,113]. The chemical potential may change when electrons heat up. The new chemical potential conserves the number of electrons:

$$\int_{-\infty}^{\infty} DoS(E) \cdot [f_{FD}(E,\mu,T) - f_{FD}(E,\mu_0,T_0)]dE = 0 \qquad (4.14)$$

Using Eq. 4.13 and 4.14, we can estimate the electron temperature.

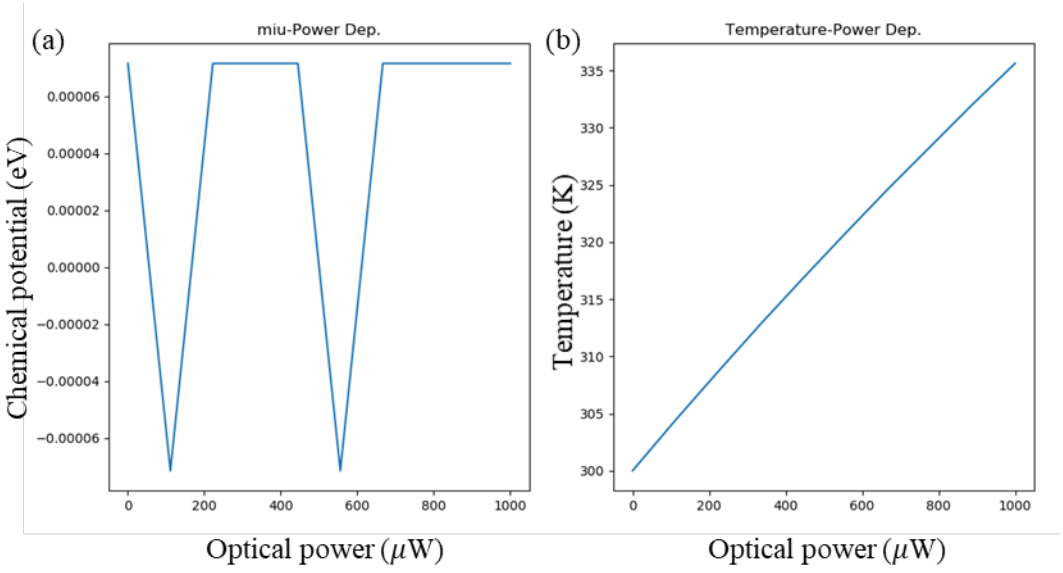

Figure 4.7. The dependence of chemical potential and electron gas temperature on illumination power. (a) change of chemical potential starting from $\mu_0 = 0\ eV$ in darkness. The peaks result from computational artifacts from finite elements, which is physically sufficiently small. (b) corresponding lattice temperature in Kelvin. The result matches the value previously reported in orders of magnitude[50].

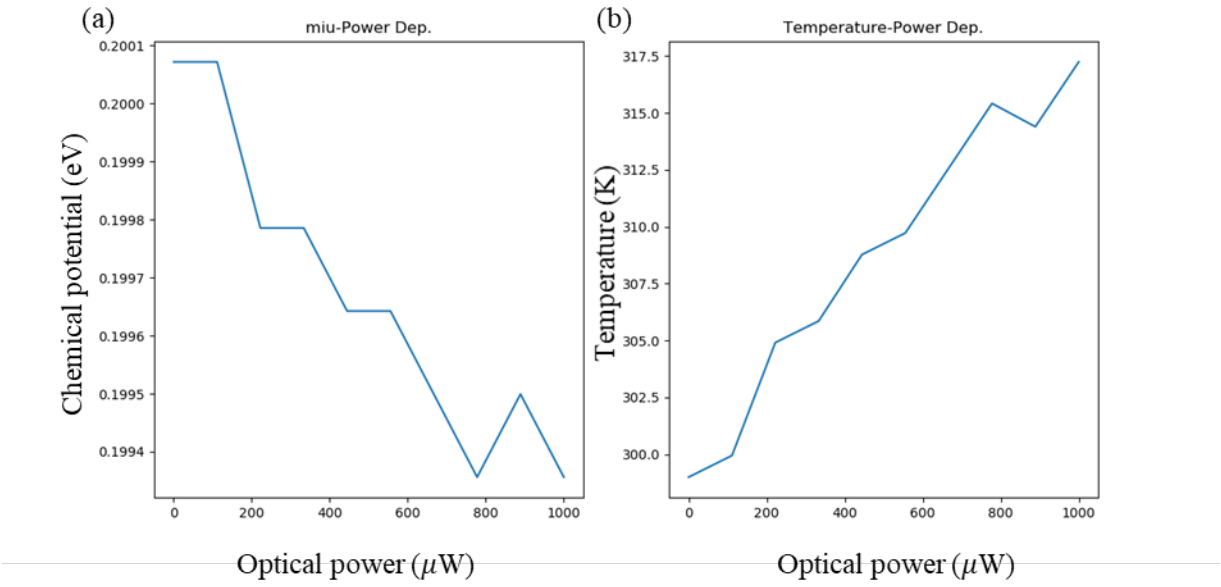

Figure 4.8. Same plot as Fig. 4.7, but with $\mu_0 = 0.2\ eV$ in darkness. A larger drift of chemical potential is observed due to broken electron-hole occupation symmetry. The temperature change is smaller as a result of increased heat capacity at higher doping.

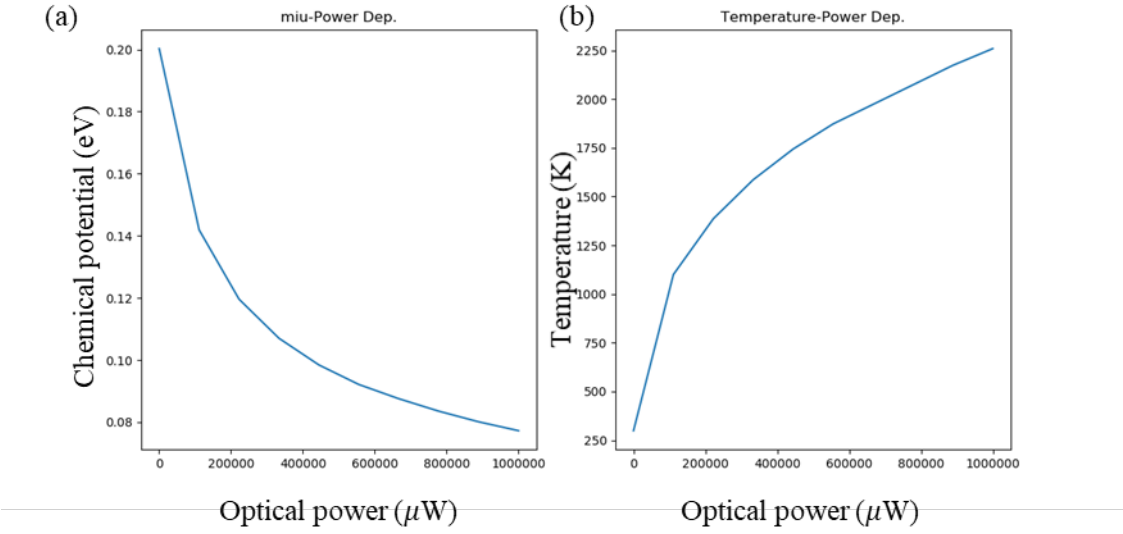

Figure 4.9. Same plot as Fig. 4.7, but with 1000-time broader instantaneous power range.

The chemical potential change is smaller than 1 meV, consistent with our order-of-magnitude estimation in the previous section. The temperature variance is low under natural light, which has

very low instantaneous power. In previous works, the researchers used a laser power of 1mW and pulse duration around 90 ps for a supercontinuum laser. Assuming the repetition rate is 100 MHz, the instantaneous power is 3 orders of magnitude larger than in our model. Then the model gives a result similar to the previous work (see Fig. 4.9).

We then analyze the contributions of (1) tunneling before thermalization, (2) tunneling after thermalization, and (3) thermionic transport that happens after the thermalization. We plot the contribution percentages to both bias, wavelength, and illumination power.

The direct tunneling's contribution is not always dominant. We consider only an electron barrier of 0.5 eV, with the hole barrier much higher. The illumination power is 100 μW. The dominant effect depends on multiple parameters, including initial doping of the graphene layers, interlayer bias, barrier thickness, and wavelength.

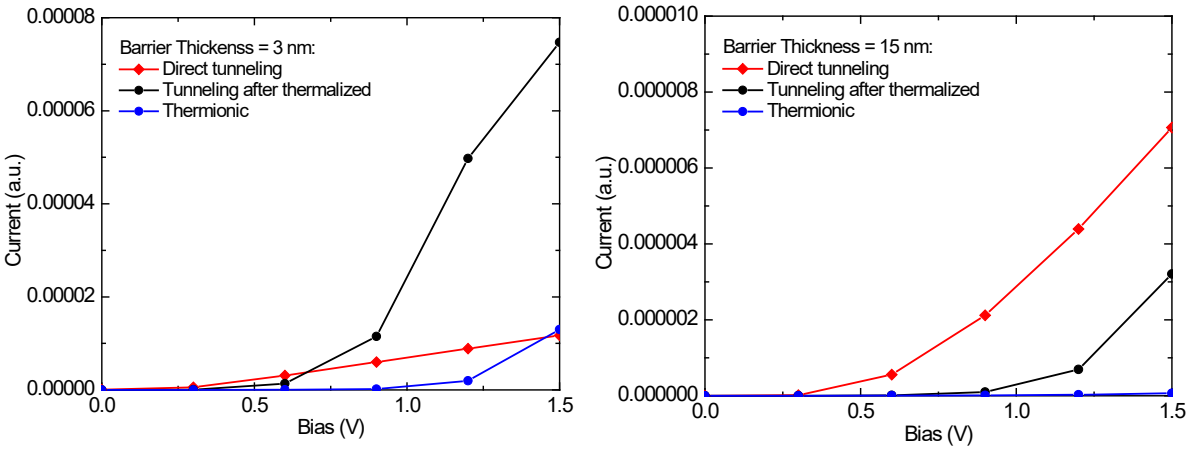

Figure 4.10. Contributions of interlayer carrier transfer. The figures above are simulated with environmental doping condition: μ_t = 0.01 eV, μ_b = -0.01 eV at zero bias.

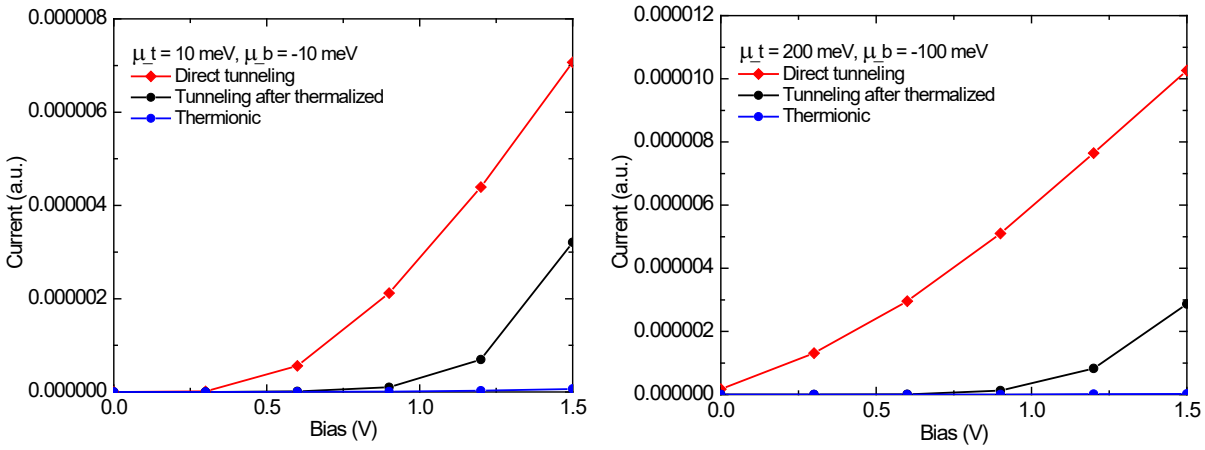

Figure 4.11. Same plot as Fig. 4.10, with barrier thickness of 15 nm.

Based on the simulation results, we chose a relatively thick barrier of 15 nm, with the doping profile of $\mu_t = 0.25\ eV,\ \mu_b = -0.25\ eV$. The doping profile is easily accessible via electrostatic and/or chemical doping. We explore the wavelength and bias dependence of the tunneling current (Fig. 4.12 and 4.13). Under natural light illumination, thermalization effects are negligible. This makes the system linear enough for spectral reconstruction.

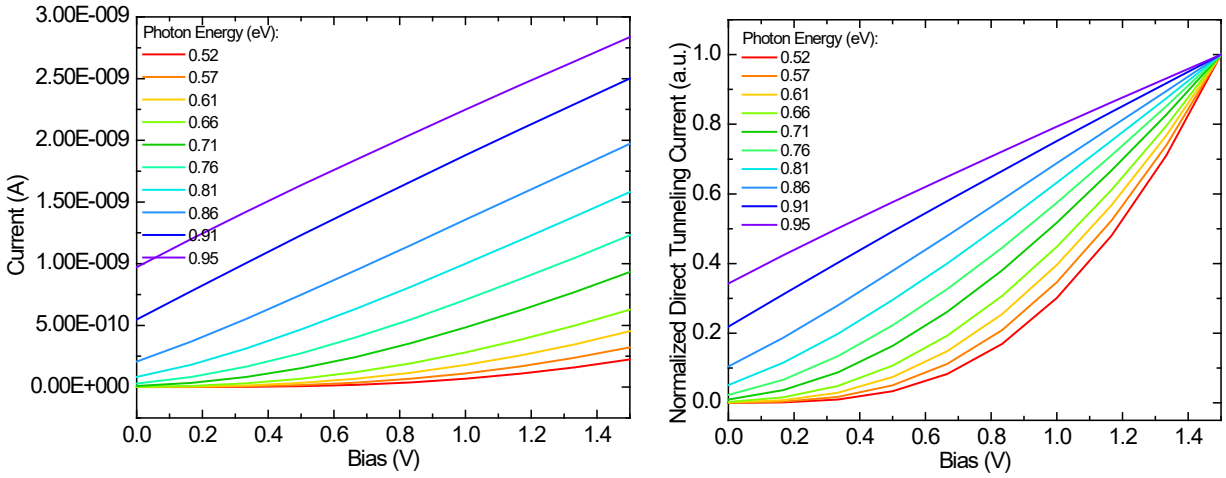

Figure 4.12. Tunneling photocurrent under different interlayer bias and wavelength. Left: absolute values; right: curves normalized with maximums for better comparisons.

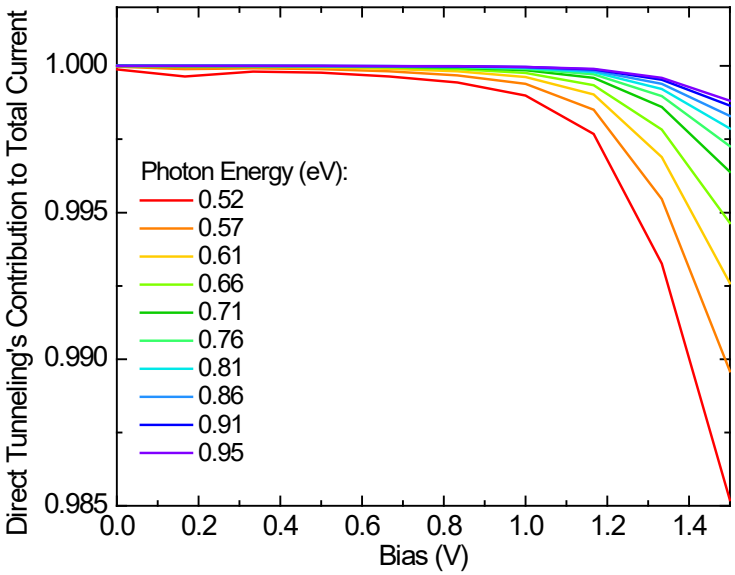

Figure 4.13. The percentage of interlayer photocurrent contributed by direct tunneling before thermalization. Optical power = 1 mW.

4.6.3 Modeling of Photoconductive Gain

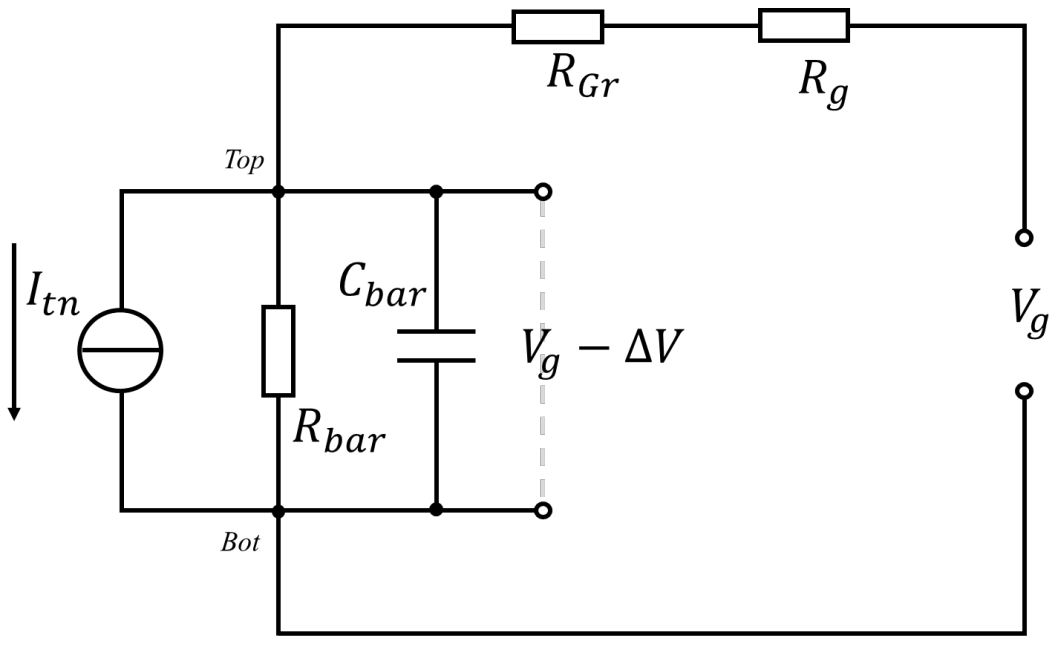

Figure 4.14. Equivalent circuit of the graphene phototransistor under operation.

Fig. 4.14 illustrates the equivalent circuit model that produces the photoconductive gain. The interlayer photocurrent is equivalent to a current source (I_{tn}) paralleled with a barrier resistance R_{bar} and a capacitance C_{bar}. The resistance is above 100 GΩ, and the capacitance is around 0.1 pF for our device. R_{Gr} is the graphene channel resistance, typically at 1 kΩ. R_g is a resistor tied to the gate bias source to protect the device from electrostatic discharges. It is set at 10 MΩ. When light is chopped at a frequency of ω, the bias across the barrier is not equal to V_g, the deviation is given by:

$$\frac{\Delta V}{R_{bar}} + \frac{\Delta V}{R_{Gr}} + j\omega C \Delta V = I_{tn} \qquad (4.15)$$

Hence the voltage difference is:

$$\Delta V = \left(\frac{1}{R_{bar}} + \frac{1}{R_{Gr}+R_g} + j\omega C\right)^{-1} I_{tn} \qquad (4.16)$$

For the graphene phototransistor, the photocurrent is determined by the transconductance g_m:

$$I_{ph} = g_m \Delta V \qquad (4.17)$$

Hence the photoconductive gain is:

$$G = \frac{I_{ph}}{I_{tn}} = g_m\left(\frac{1}{R_{bar}} + \frac{1}{R_{Gr}+R_g} + j\omega C\right)^{-1} \qquad (4.18)$$

For the previous publication, the gate is floated ($R_g \to \infty$). The photoconductive gain reduces to:

$$G = \frac{g_m R_{bar}}{1+j\omega C R_{bar}} \qquad (4.19)$$

The RC product is around 1ms – 1s, hence the operation frequency of the device remains at around 1 to 1000 Hz, while the photoconductive gain is very high: With regular $g_m \sim 4 \times 10^{-2}\ A/V$ for graphene transistor with a square channel and 15 nm gate dielectric, G is over 10^9.

For a finite gate resistance around 10 MΩ, the photoconductive gain reduces to:

$$G = \frac{g_m R_g}{1+j\omega C R_g} \qquad (4.20)$$

The RC product points to a 1-MHz operation speed. As a tradeoff, the gain reduces to around 4×10^5.

Attaching a gate resistance does not produce anything in device performance beyond the gain-bandwidth product. However, it allows us to make the device gate tunable as a spectrometer. Additional nonlinearity may mix in as increased optical power shifts ΔV. A sufficiently large ΔV would modify the band alignment. The distorted band alignment would cause a shift in the tunneling efficiency. Hence to thoroughly understand the limitation of the spectral reconstruction, we need to consider the effects of both thermalization and optical power-induced band-distortion.

The analysis requires absolute value estimation of the photocurrent. The value given above is simulated with the following method: We first adopted Eq. 4.6 to study the dark current[107,114]. Then we compare it with our simulation to fit the unknown parameter related to the transfer matrix in Fermi's Golden Rule:

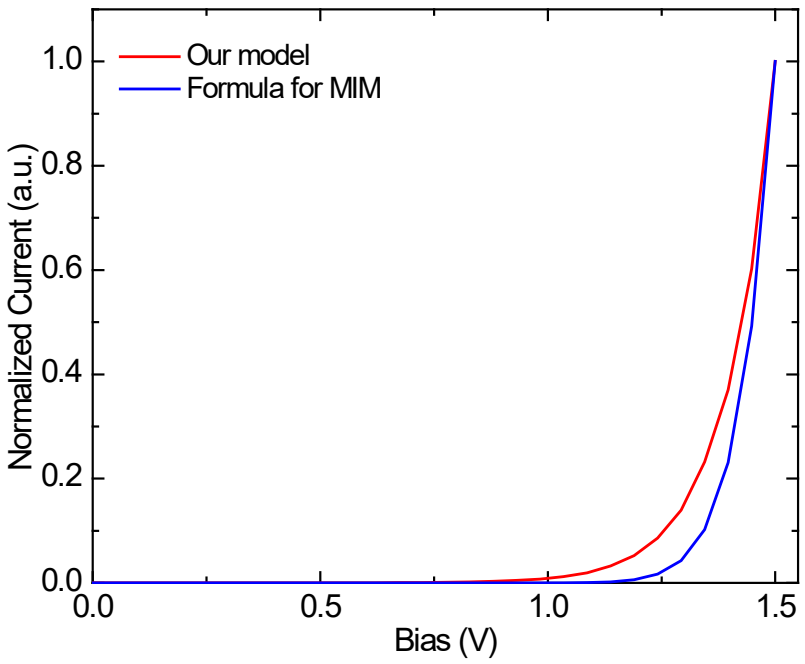

Figure 4.15. Bias dependence of dark tunneling current. Comparison between MIM equations and our model. Both curves normalized with their maximums.

This works only in estimating the order of magnitude, since graphene has a much lower DoS compared with metal contacts in the model. The lower DoS leads to a substantial Fermi level shift when biased, so that the MIM equation no longer holds strictly. In our case, the Fermi level shift lifts the barrier height when further forward bias, hence producing the difference indicated in the figure above. Taking parameters of our device into the equation, we get a value of 0.3 pA for 1V bias, while our model gives the number 3×10^{-9}. A factor of 10^{-4} is assigned to the model to get a current in ampere. The value is used only for order-of-magnitude predictions.

Now we have two equations in the tunneling barrier model for determining ΔV or the interlayer photocurrent:

$$V_{bias} = V_g - R_g \Delta I \qquad (4.21)$$

$$\Delta I = f(V_{bias}) = f\left(V_g - R_g \Delta I\right) \cong f\left(V_g\right) - R_g \Delta I \frac{df}{dV_g} \qquad (4.22)$$

Hence, $\Delta I \cong \frac{f(V_g)}{1+R_g \frac{df}{dV_g}}$ (4.23)

This equation holds for small $R_g \frac{df}{dV_g}$. For the photocurrent mentioned above at 0.1 mW, we have a range of 0.75~3 nA. The slope is approximately 0.05 ~ 2 nS. This makes the correction term to be equal to 0.0005~0.02. Hence the higher-order terms are negligible. With proper ΔV, we can calculate the change in channel current based on the doping shift. The channel current is related to the Fermi level following the equation[115]:

$$\sigma(V_{bias}) = C \frac{e^2}{h} \frac{n}{n_i} \qquad (4.24)$$

C is around 20 as an experimental value, and the disorder-related effects are negligible for our heavy doping profile. We do not count in the conductivity change due to electron temperature change, since previous experiments have shown a responsivity less than 1 mA/W in a single graphene channel. Multiple mechanisms, including bolometric effect, photo-thermoelectric effect, and photovoltaic effect, contribute to the small responsivity. It is considered as a < 3% deviation from the ideal case.

We checked the system linearity at the longest wavelength (2.4 μm) applied in the system. At this wavelength, thermalization makes the most significant contribution to the tunneling current.

The thermalized carrier's current tends to provide a superlinear power dependence of the tunneling current. The power change from 10 to 110 μW only produces a 1% error in responsivity, good enough for reconstruction based on the linear system assumption.

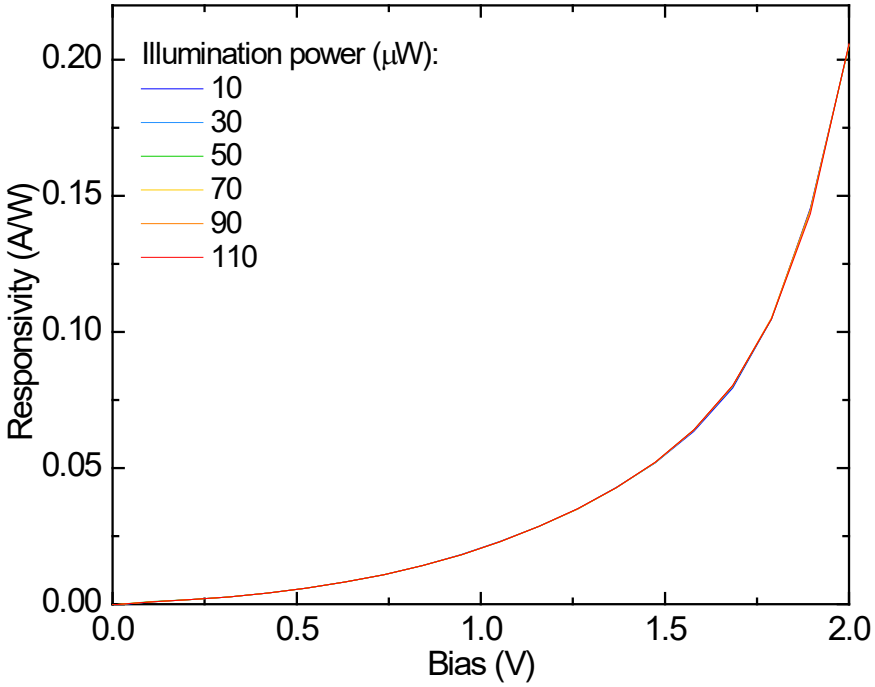

Figure 4.16. Responsivity curve under different power of illumination at 2.4 μm.

4.6.4 Simulation Results

Finally, we use our model to study the proper band profile and testing conditions for a defect-free device. To increase the spectral resolution, we add more features to the photocurrent by changing the barrier shape, as shown in Fig. 4.17 (a). Simulation under identical conditions produces photocurrents with more spectrally dependent features, boosting the number of effective sampling points to 16, or a wavelength resolution of 75 nm. If we continue to increase the number of sampling points at the same spectral range, the regression method produces overfittings in the reconstructed spectra and reduces the accuracy, which is evident from Fig. 4.17 (c). Notice that we used a WKB model for calculating the tunneling rate. The resonant tunneling is not considered. Resonant tunneling of dark current at room temperature was

experimentally observed in such systems[116]. Such phenomena could further increase the resolution of our spectrometer.

More efforts in the algorithm can further overcome the accuracy-resolution tradeoff. A regularizer in the LLS method sends pre-knowledge to the system. For example, in Fig. 4.3 (b), we used a LASSO regularizer that pre-assumes a sharp peak instead of a broadband distribution. Such techniques sacrifice the generality of reconstruction accuracy but work exceptionally well for a subset of testing spectra for specific purposes. Another strategy is to introduce more nonlinearities in the algorithm, such as adopting an artificial neural network. This would make the algorithm more robust over non-idealities in the device, such as current drifting and hysteresis. The tradeoff is that it requires a larger training data set.

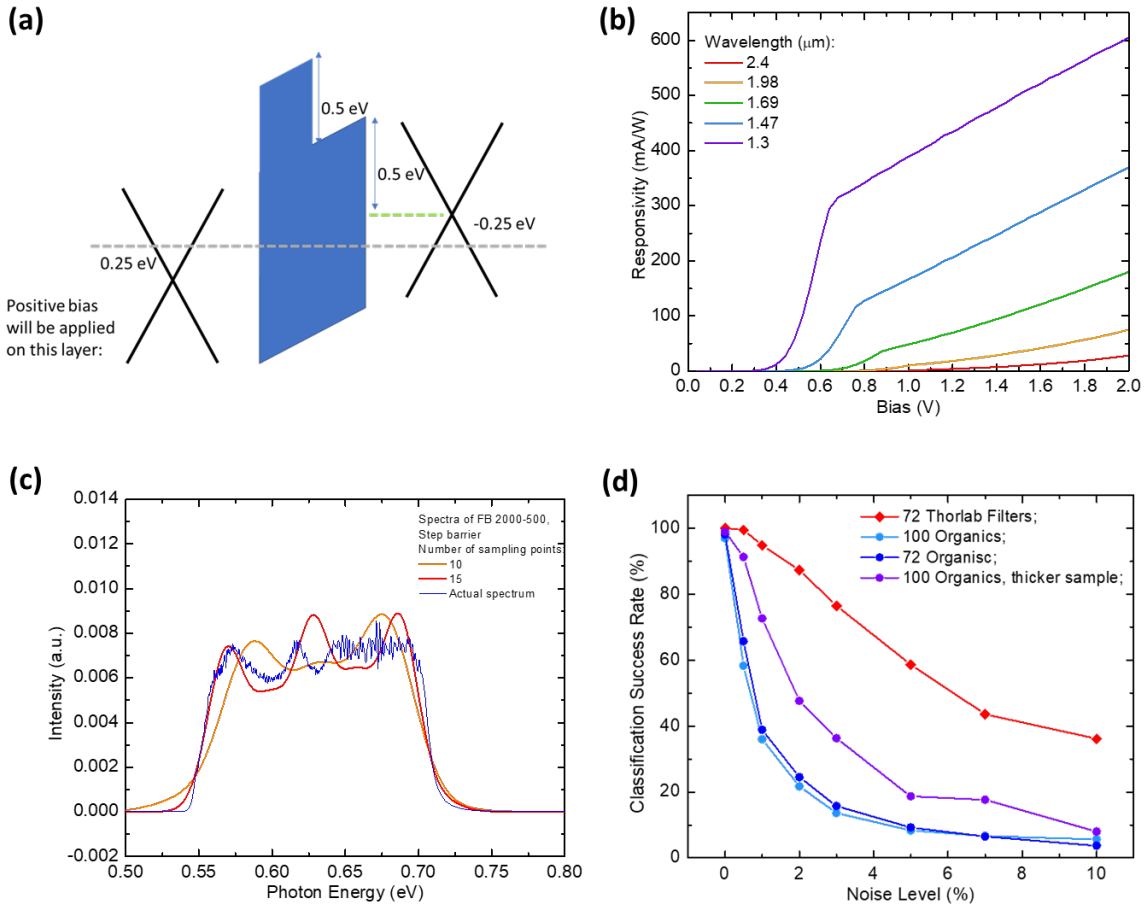

Figure 4.17. Simulation of responsivity and spectral reconstruction in a further optimized band structure and working condition. The channel bias holds at 1 V. (a) Band profile and responsivity (b) of the device with a step barrier under identical testing conditions. (c) Comparison of the accuracy-resolution tradeoff with different regression parameters. (f) Accuracy of spectra-based classification and its dependence on the noise level.

Lastly, we demonstrate classifications of materials based on the photocurrent readout. This avoids the high-resolution reconstruction of spectra but meets realistic needs. We adopted the transmittance and reflectance of 72 Thorlab filters and IR spectra of 100 organics[117] as the optical input. The simulation shows that our system can classify the materials at decent accuracy with different noise levels considered, as shown in Fig. 4.17 (d).

The experiments and simulations above point to improvement that can be made: We can minimize the side effects by removing traps and improving the system linearity through more careful choice of the dielectric and encapsulating materials. Especially, 2D semiconductors are excellent choices, since there have already been many works indicating a high quality of interfaces between these 2D materials[108,109]. As suggested by the simulation, the band profile of tunneling barriers, including barrier height, thickness, graphene doping profile, and incident wavelength range, also have to be designed to achieve decent performance.

4.7 Conclusion

By electrically tuning the barrier distortion of a graphene-dielectric-graphene heterostructure, we successfully modulated the spectral response of a graphene-based phototransistor. We further demonstrated the possibility of utilizing such kinds of devices to extract spectral information of light sources. More work can be done as discussed to improve the performance of such kind of electrically tunable photodetectors. Moreover, this work can lead to a large variety of applications in IR spectroscopy and hyperspectral imaging.

Chapter 5
Neural Network Enabled Graphene Transparent Multi-Focal-Plane Imaging System

5.1 Introduction

Transparent photodetectors have different applications, including optical sensing components in transparent or wearable electronic systems[118,119,120], reflectivity detection[121], and interference pattern recognition[122,123]. These transparent photodetectors have a tradeoff between responsivity and transparency. The graphene-based phototransistor we studied in Chapter 4 overcomes the tradeoff with photogating effects[54]. The detectors absorb only a few percent of incident light yet give a significant photoresponse. Moreover, graphene is also an excellent transparent electrode material for various applications[7,8]. These factors enable us to use graphene to make transparent imaging arrays.

On the other hand, emerging technologies such as autonomous vehicles demand imaging technologies that can capture not only the 2D image but also the 3D spatial position of objects. People have been implementing LiDAR systems[124,125,126], 3D computational imaging methods[127,128], and light-field cameras[129]. Using our transparent graphene photodetectors, recent works proposed several computational imaging methods to achieve high-resolution light-field imaging[130,131,132]. The proposed approach applies sophisticated model-based image reconstruction from multi-focal-plane images (focal stack) obtained by stacks of photodetector arrays to reconstruct light-fields of scenes effectively. However, only preliminary data from two transparent pixels was used previously to test the idea of 1D depth ranging[18].

This chapter introduces a multi-focal plane imaging system enabled with all-graphene photodetector arrays and a neural network algorithm. Figure 5.1 (a) illustrates the structure and

working principle of the novel imaging system. In the imaging process, an arbitrary object (e.g., a ball-and-stick model) is projected by the camera lens to the right side. Graphene-based imaging arrays are stacked at different focal planes. They are highly transparent so that the projected light field well illuminates all planes. An illuminated detector absorbs only a few percent of light and gives a large photoresponse. Hence, we can capture images at a stack of focal planes. Each image in the stack records light distribution at a specific depth. We can then use neural networks to process the images and reconstruct the 3D configuration of the object. This imaging system allows 3D image reconstruction with a single exposure and ultra-compact setup.

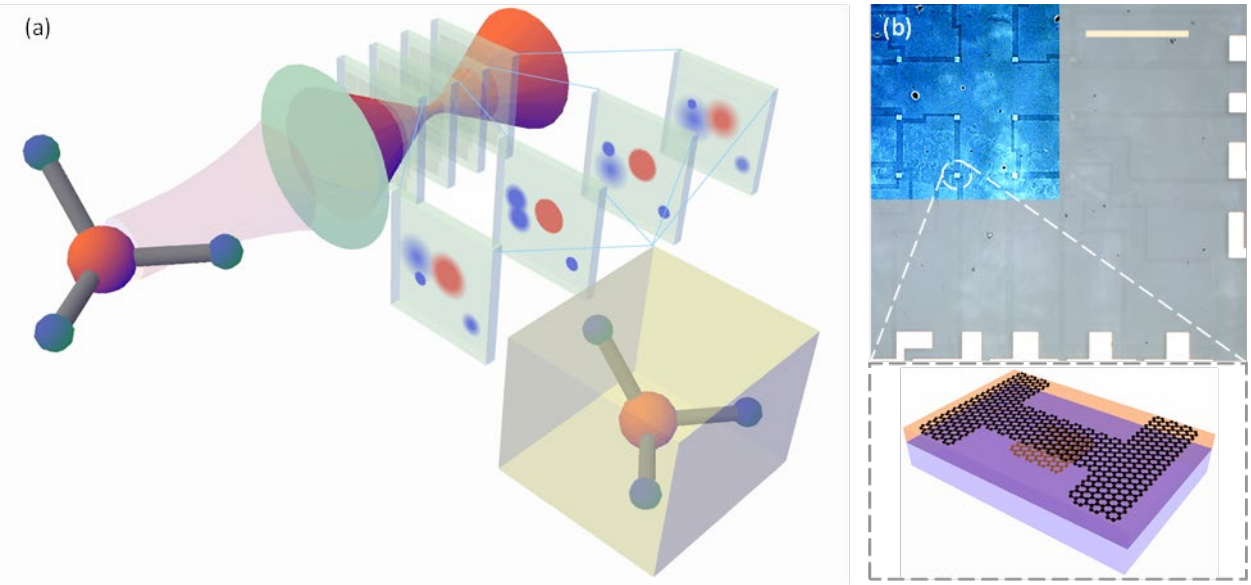

Fig. 5.1. Design of light-field imaging system. (a) A conceived diagram of the arrangement of the imaging planes in a camera. Depth information of objects is captured by multiple detector planes. (b) Upper panel: Image of a 4-by-4 transparent photodetector array under an optical microscope, scale bar: 500 μm. The top-left corner is with artificially enhanced color and contrast in order to visualize the patterns. Lower panel: Schematic of a single graphene phototransistor, wired out with graphene as interconnects.

We first show the devices' decent yield, responsivity, and transparency that allows a scalable transparent imaging array. We then demonstrate that the assembled multi-focal-plane imaging system, together with a feedforward neural network, can accurately estimate an object's 3D position. The performance of the system is tested with a point source as the object. Experimental results show that our graphene-based transparent photodetector array is a scalable solution for 3D information collection. This type of optical system is potentially useful for emerging

technologies such as face recognition, autonomous vehicles, and unmanned aero vehicle navigation.

5.2 Device Fabrication and Characterization

Fig. 5.1 (b) shows a schematic of the photodetector array and structure of a single pixel. We used CVD-grown graphene on copper foil and used a standard wet transfer technique in our process[98]. The device structure, photodetection mechanism, and fabrication process are identical to the device discussed in Chapter 4. The exceptions are that the substrate is glass and that the bottom layer graphene is floated as the gate. We fabricated a 4-by-4 array of phototransistors. The devices are wired out separately and connected to metal pads. The pads connect to a customized signal readout circuit. During regular operation, we apply a bias across the graphene channel and measure the channel current. Light illumination induces a change in the current, producing photocurrent as the readout.

We fabricated two such sensor arrays and mounted them along the optical axis, separated at a distance, to form a stack of imaging planes. Fig. 5.2 (a) shows the optical and electrical setup. For a simple demonstration, we used a convex lens to focus a 532 nm laser beam and used the focused beam as a point object. A motorized stage controls the position of the object-generating lens to change the 3D position of the object. To remove the phototransistors' drifting and hysteresis effects, we chopped the beam at 500 Hz and captured the AC photoresponse. In the imaging process, the light beams pass the detector planes mostly unperturbed. This enables us to simultaneously capture images of an object in multiple planes as if the other detector planes do not exist. A DC bias of 0.5 V is applied across the graphene channel of the pixels. The current is collected by a scanning line circuit that helps to switch between different pixels. A pre-amplifier amplifies the channel current. The signal is then sent to a lock-in amplifier, where the signal is synchronized with the chopper and the AC photocurrent is extracted from the devices.

5.2.1 Properties of Fabricated Device:

The yield and uniformity of devices are first characterized by measuring the channel conductance. 99% of the 192 devices show sufficiently large channel conductivities (see Fig. 5.2). The high yield demonstrates the feasibility of using these graphene-based detectors as an imaging array. We then examine the photoresponse of a single pixel. We observe a 3 A/W responsivity at the channel bias of 0.5 V. It is consistent with the previous publications[54,130] in the order of magnitude. A lock-in amplifier measures the AC photocurrent. This measurement scheme sacrifices responsivity but makes the measurement faster and more reliable. The power dependence of the AC photocurrent is also examined. The responsivity remains constant in the power range of interest. Hence only a single exposure is necessary to calibrate the nonuniformity between the pixels. To examine the transparency, we measured the transmission of an array with a beam focused on the plane. The transmission of the 532-nm laser through the array is 81%, while the glass substrate's reflection causes an 86% transmission, as measured at the chip's graphene-free area. The graphene detector array contributes to only a 5% decrease in transmission. Moreover, the transparency can further improve by refractive index compensation methods such as anti-reflective coatings or oil immersion. The imaging array is demonstrated with good transparency using graphene as both device and interconnect material.

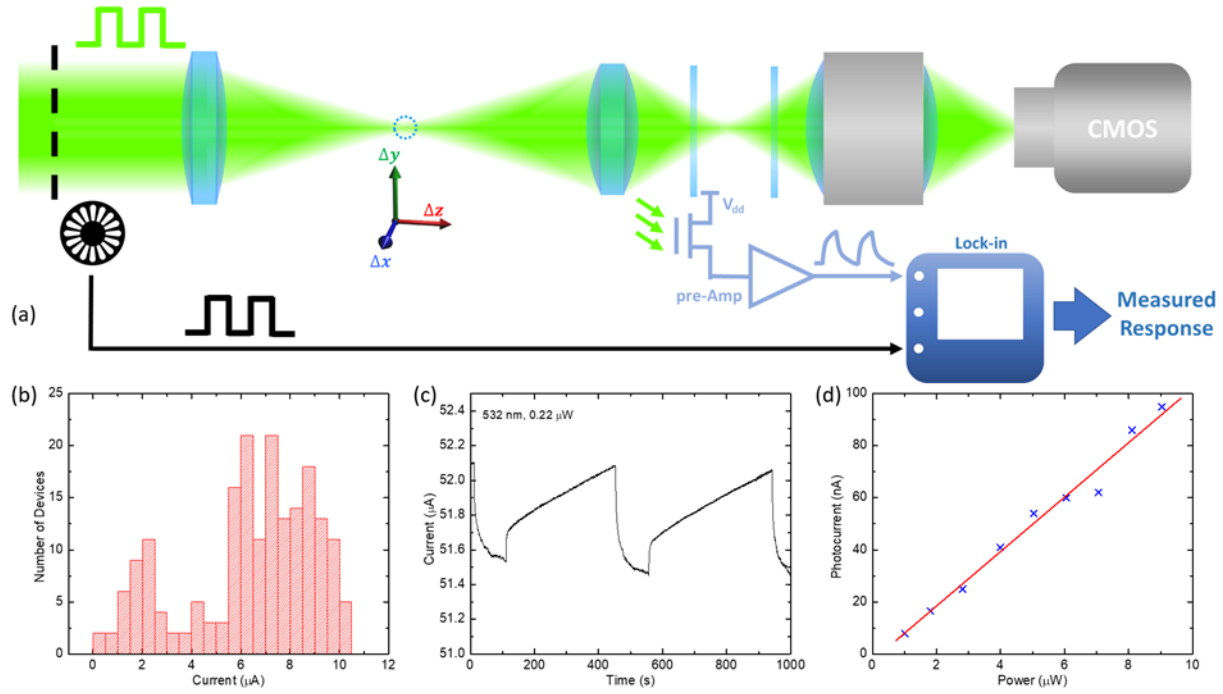

Figure 5.2. Optical and electrical measurements on the device. Device yield (b), DC temporal photoresponse (c), and AC response with a linear power dependence (d).

The photoconductive gain provides high responsivity. However, such detectors may be noisier given that not only signals from the 'clean' photons are amplified. Noise analysis is necessary to validate the application of the system.

5.2.2 Device Noise Analysis

The noise equivalent power (NEP) is a good measure to discuss the SNR in practical applications. The NEP of the device is discussed in the supporting information of our previous work[54]. We collect our data with a modulation frequency of 500 Hz. At this frequency, the noise spectral density is 10^{-9} A/Hz$^{1/2}$. The noise level is consistent with the 1/*f* noise of graphene transistors observed in other works[133]. The channel's 1/*f* noise dominates over the shot noise of dark currents in the tunneling barrier. With an AC responsivity of 10 mA/W, the NEP is 0.1 μW/Hz$^{1/2}$. The value is small compared with our test illumination power of ~10 μW per device.

We can also compare this with realistic illumination powers in a camera system. Assume a camera system with a 20-mm aperture and a numerical aperture of 0.7. When using it to image a white Lambertian surface under sunlight, the estimated optical power per pixel is 0.05 μW. This indicates a relatively low SNR for our current device.

The low SNR is mainly due to the detector's slow response, which is caused by the large density of charge traps in the tunneling barrier. Charge traps capture the tunneling charges and compensate the local field that motivates more interlayer hopping. One of our previous works replaced amorphous silicon with high-quality Al_2O_3. The responsivity at 1 kHz is as high as 60 A/W at 532 nm[55]. Taking all the corresponding design variations, including increased noise due to a larger channel current, we expect a NEP of 0.1 nW/Hz$^{1/2}$, which is sufficient for practical applications. In this experiment, we did not adopt the Al_2O_3 barrier for fabrication yield considerations, as the thin material is vulnerable to the base used in lithography. Nevertheless, there is no fundamental limitation that prevents us from fabricating transparent devices with higher speed and responsivity.

In the above discussion, experimental results suggest that the tunneling current is not the major contribution of noise. For a complete discussion, we can further analyze the tunneling noise's

order of magnitude. The shot noise's current spectral density is $S = 2eI$ when the interlayer bias $V >> kT/e$ [134]. The current is the total of the dark current and the photocurrent, which is around 10 pA in our device. Hence the noise current density of the tunneling photodiode (before amplification) is around 1.8 fA/Hz$^{1/2}$. The value is much smaller than the photocurrent at any practical illumination power. Also notice that $1/f$ noise is not considered here so that the estimation only sets the lower limit for the noise amplitude contributed by the tunneling current before being amplified by the photogating effect. Moreover, neural networks can be trained to be robust against input noises. This further lifts the SNR requirements for the reported application.

In summary, the device's noise is dominated by the $1/f$ noise in the channel. The photoconductive gain amplifies the noise from the vertical tunneling diode. However, it does not dominate the device noise based on both tests and order-of-magnitude estimation. Better implementation of the device to image ambient objects needs an increase in responsivity. One promising way is to improve the tunneling barrier quality.

5.2.3 Transparent Interconnects

In the array design, graphene is used not only as the pixel material but also as the interconnect. Compared with other transparent electrode materials such as indium-tin oxide (ITO), graphene is significantly thinner at similar conductivity. This allows minimized optical interference patterns generated from the interconnect patterning, as well as suppressing edge scatterings of wires, see Fig. 5.3 for a comparison of optical transmission images of arrays under 532 nm laser illumination.

Even though the interference and scattering effect for ITO wires can be reduced with a refractive index compensation layer, it adds more complexity to device fabrication. Furthermore, it is harder to design optical antireflection coatings for each layer of photodetector arrays. For the graphene case, easy refractive index matching is possible with oil immersion that matches the glass substrate's refractive index.

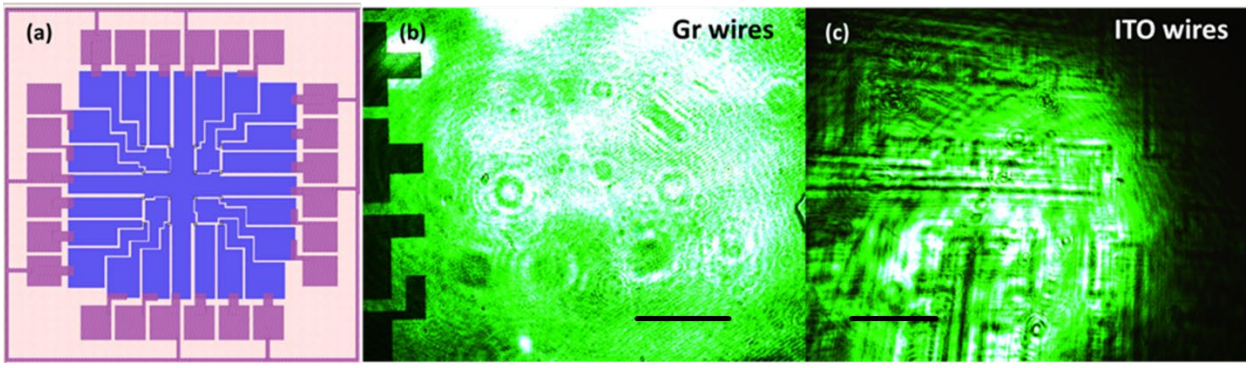

Figure 5.3. Array design (a) and optical images of one photodetector array captured by CMOS camera. Samples with graphene interconnects showed significantly weaker interference and scattering than samples with ITO interconnects, scale bar: 400 μm.

5.3 Multi-Focal-Plane Imaging

Given the devices' good yield, responsivity, and transparency, we used the transparent detector arrays for multi-focal-plane imaging. Fig. 5.4 (a) shows the images captured experimentally by the two arrays when a point object gradually moves away from the camera system. An illustrative diagram with a Gaussian beam is plotted together with the corresponding conditions in Fig. 5.4 (b). When the point object is close to the camera, it is imaged to somewhere close to the back imaging plane. At the same time, the front imaging plane only records the out-of-focus pattern of the object. When the source moves far away from the camera, the focused spot shifts to the front, so that the image captured by the back focal plane expands and blurs.

While a single image measures the lateral position of objects as in conventional cameras, the difference of images captured in different planes contains the object's depth information. Hence, the images are useful for reconstructing the 3D position of the point object.

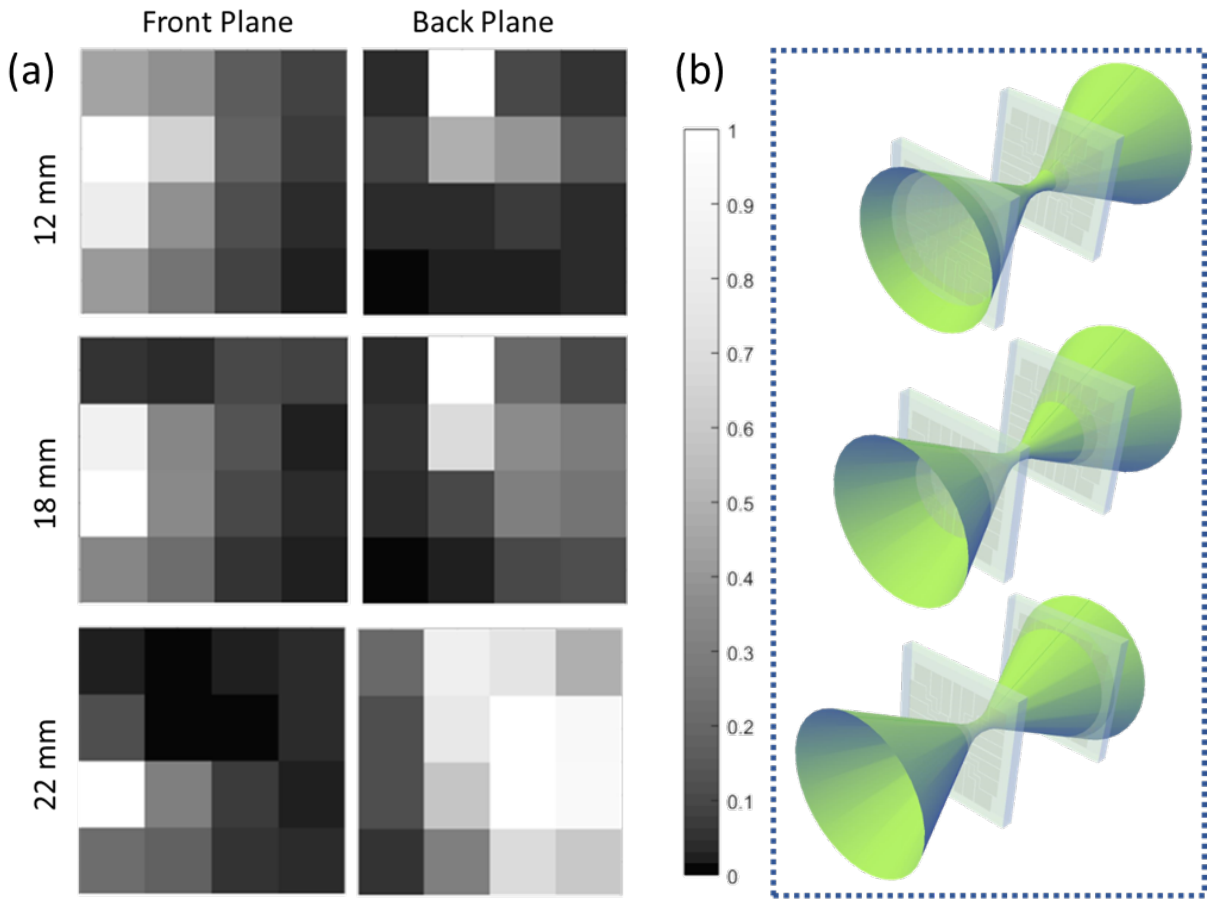

Fig. 5.4. Measurement setup and results. (a) Images captured by both photodetector planes with the object at three different positions along the optical axis (12 mm, 18 mm, 22 mm, respectively), the intensity is normalized and shown with arbitrary units. (b) The corresponding illustrations of the beam profile and the imaging planes of the left panel.

5.4 Introduction to Artificial Neural Networks

Computational methods can be used to decipher the 3D coordinates from the multi-focal-plane images. My collaborator, Mr. Zhengyu Huang, worked on algorithm development and found that artificial neural networks (NNs) work exceptionally well for our purpose. The major work contributed in the software side will appear in his Ph.D. thesis. In this thesis, we briefly discuss the results (Section 5.5), with a general introduction to neural networks (Section 5.4) for completeness.

NNs are computation architectures mimicking the neural system of animal brains. An NN consists of multiply artificial neurons. These neurons connect with the input, output and/or other

neurons. Each of the neurons receives signals (typically real numbers) from other parts of the network. After processing the input signal (usually with a nonlinear function), the neuron transmits the signals to other units with different weights.

Typical artificial NNs are organized into layers. For example, Fig. 5.5 shows a fully connected neural network we used for 3D position tracking. Each input is connected to multiple neurons in the first layer. When the signal propagates from left to right (forward propagation), the signal multiplies a weight assigned for each line between the input and first layer. At the input of each neuron in layer 1, the weighted signal from all inputs sums up. The summed signal is sent to a nonlinear function to produce the neuron's output. Subsequently, the output from layer 1 is sent to layer 2 following the same formalism. The ultimate output is expected to produce target values after training.

There are two important operations of the neural networks: the training process and the inference. In the training process, the neural network is provided with examples to learn from. Each example (training case) consists of a set of inputs and its corresponding correct output. The input signal propagates forward and gives predicted outputs. Initially, the output values differ from the correct ones. We can calculate a loss function (usually a measure of prediction error) and backpropagate the loss to the left. The tuning of each linear weight has a different effect on the loss. We can compute the loss function's partial derivative over the weights to determine the tuning amount that minimizes the loss function. An optimization algorithm takes advantage of the backpropagation to tune the weights at each training cycle slightly. By sending in many cases in many training cycles, the prediction error gradually reduces to a minimized value.

In the inference process, the test dataset is sent to the input. The output of the trained neural network is expected to resemble the correct values closely. We can evaluate the prediction accuracy by calculating the error between the output and correct values.

The neural network is an essential technology for machine learning. It can perform tasks without specific task-based, user-defined programs. Instead of compiling and processing codes, it learns to generate desired output through the training process. NNs are powerful tools in computer vision, speech recognition, computer translation, and many other fields.

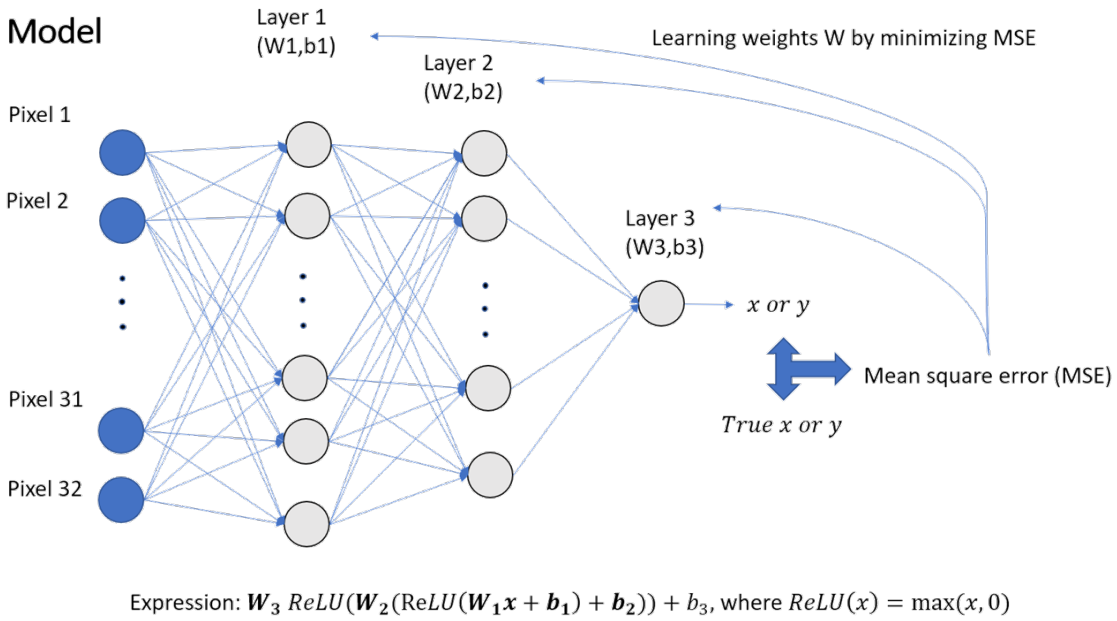

Figure 5.5. An example of a NN used in our 3D position tracking and its training process. Courtesy of Mr. Zhengyu Huang.

5.5 3D Position Tracking

For a proof-of-concept demonstration of 3D object detection using focal stack data, we track the 3D position of a single-point object translated in three dimensions. In the experiment, we moved the point object (dotted circle in Fig. 5.2 (a)) in a 3D spatial grid of size 0.6 mm × 0.6 mm × 20 mm by moving the lens on the left in Fig. 5.2 (a). In particular, we moved the lens using a 3D motorized stage; the point object moves accordingly as the lens moves, because the lens generates the point object. We set the distance between 3D grid points as 0.06 mm, 0.06 mm, and 2 mm, along x-, y-, and z-directions, respectively, leading to 1331 grid points in total. We collect double image stacks of the point object at each 3D position (as in Fig. 5.4). The dataset is separated into a training set and a test set. Each case (datapoint) in the dataset consists of 32 photocurrents (from two layers of 4-by-4 sensor arrays), together with the x, y, and z coordinates of the point object. The photocurrents are used as inputs to the neural network. The 3D coordinates are used as the expected values in the training process discussed above. We trained three separate MLP[135] neural networks to estimate the point object's three spatial coordinates from the focal stack (one for each spatial dimension); then, we evaluated its performance on the test set. The test results show that even using a photodetector array with very limited resolution

and only two imaging planes, the point object positions can be estimated accurately; see Fig. 5.6. For the entire test set, we measured estimation errors with root mean square error (RMSE) values: RMSE values are 0.012 mm, 0.014 mm, and 1.196 mm, along x-, y-, and z-directions, respectively.

We further performed 3D object reconstruction of extended objects with synthesized low-resolution data and high-resolution image stacks captured by a CMOS camera. For complete results, please refer to our journal paper[136] and Mr. Zhengyu Huang's Ph.D. thesis. Mr. Huang made a major contribution to the algorithm and CMOS camera testing of the system.

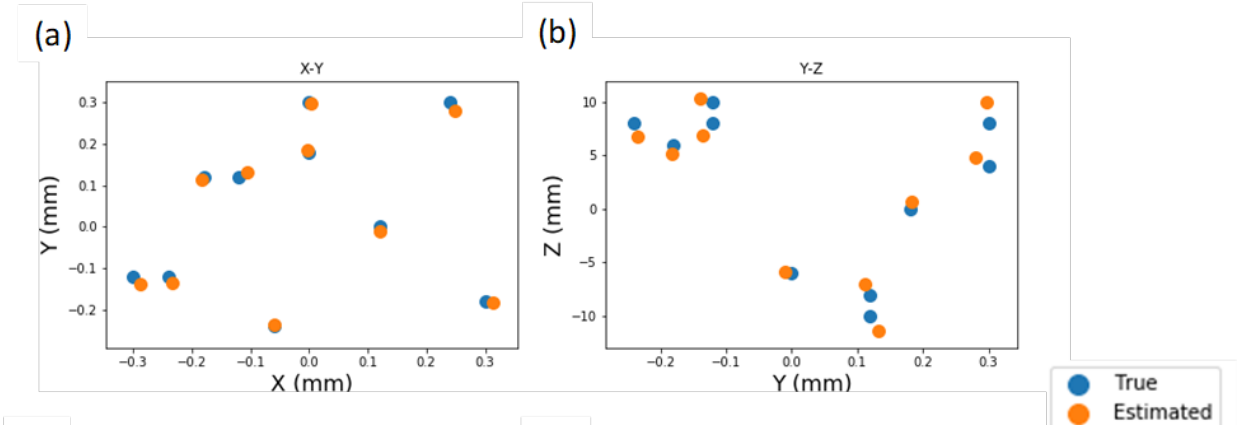

Fig. 5.6. Results of 3D point object tracking using focal stack data for three different types of point objects. (a)(b) Tracking results for single point object (only 10 test samples are shown).

5.6 Conclusion

In summary, a highly transparent, high-responsivity photodetector array with graphene as both the interconnects and photodetection pixels is fabricated. By stacking these arrays in multiple focal planes, a novel imaging system is experimentally examined. Combined with neural networks, such an imaging system can track the position of point objects even with a very limited number of pixels. After scaling-up, such imaging arrays will be a promising candidate for ultra-compact, high-resolution, and fast 3D object detection technology.

Chapter 6
Graphene as Hot-Carrier Fast Lane for Ultrafast Optoelectronics

6.1 Introduction

As discussed in previous chapters, graphene has high mobility and a picosecond scale hot carrier lifetime. The transient hot carrier dynamics enable graphene-based saturable absorbers[14,15], ultrafast photodetectors[16,46,63] and THz emitters[59,75,79,137]. The reported phenomena include photovoltaic carrier separation[46], photo-thermoelectric effect[59,75], photoconductive effect137, photo-Dember effect[16,63], thermally excited plasmons[79], etc. Despite the rich physics, pristine graphene devices showed low external quantum efficiency due to the low optical absorption[5] and ultrafast hot carrier relaxation (see Chapter 2) in the single atomic layer, which is significantly dwarfed by the bulk materials.

Still, graphene's combination of high mobility and short hot carrier lifetime is unique, especially compared with defect-rich semiconductors widely used in photoconductive switches (PCS). PCS is a mainstream technology in pulsed THz field generation and detection for THz imaging and time-domain spectroscopy[138,139]. Fig. 6.1(a) illustrates the device structure of a simple PCS. During operation, the metal pads impose a DC electric field across a defective semiconductor channel. Femtosecond laser pulses excite electron-hole pairs in the channel. The DC bias separates the excited carriers and creates a transient field that quickly decays along with the sub-picosecond carrier relaxation.

Early PCSs showed limited quantum efficiency of pump-to-THz photon conversion. To enable sub-picosecond device response, the channel materials are made defect-rich with either low-temperature material growth or ion-implantation to the crystal. The carrier mobility drops by orders of magnitudes[140,141,142] to 1-200 $cm^2V^{-1}s^{-1}$ in the damaged material. This lowers the excited carriers' travel distance before recombination and reduces the carrier separation

efficiency. Researchers employed interdigitated[143,144,145] and nanostructured plasmonic[146,147,148,149] metal contacts to make the carrier separation more efficient. However, the strategies require sub-micrometer device feature sizes, increasing the fabrication complexity. The ideal material for PCS requires strong absorption, fast carrier decay, and high carrier mobility simultaneously, which can be realized by neither pristine graphene nor defective semiconductor materials.

Fig 6.1(b) illustrates a proposed device design that combines graphene's high mobility with bulk materials' strong absorption using a 2D-3D heterostructure. A graphene layer is inserted in a regular silicon Auston switch. Under illumination, photoexcited carriers are generated majorly in silicon. The carriers first transfer to the upper graphene layer. Graphene's large mobility enables a significantly larger population of carriers to be separated and extracted before recombination. Graphene works as a hot-carrier fast lane that enables both a stronger THz emission and a larger photocurrent.

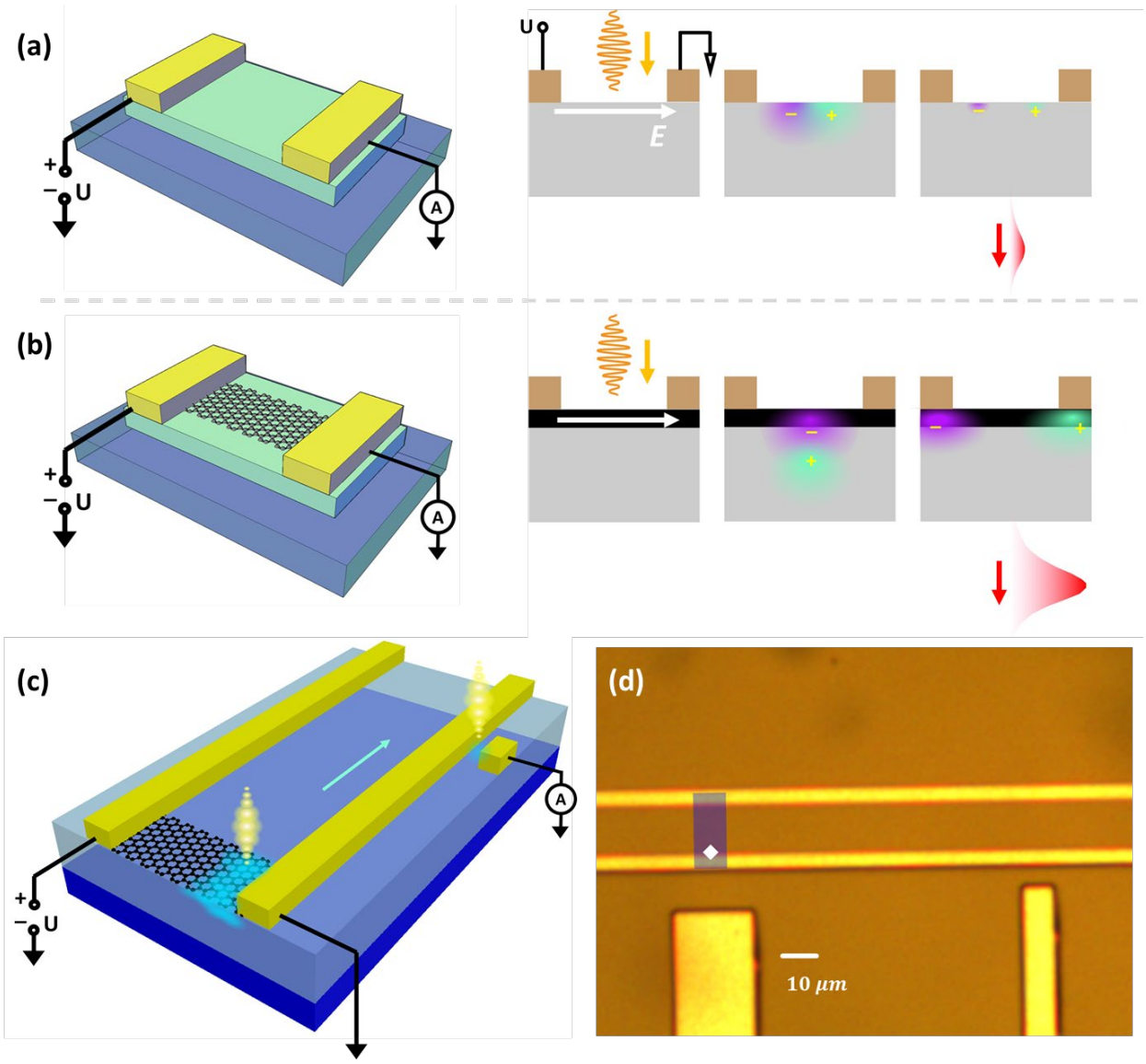

Figure 6.1. Schematic illustration of 2D-3D heterostructure-based THz emitter. (a) Structure of conventional simple THz photoconductive switch. Hot carrier separation efficiency is low due to reduced mobility and carrier lifetime. (b) Our device structure and the proposed THz emission mechanism. Vertical charge transfer happens after photo-excitation. The graphene layer enables a larger population of hot carriers to separate faster in the graphene layer, creating a stronger THz emission. (c) Schematic of the on-chip pump-probe measurement. A transmission line couples the field from the emitter to an Auston switch (detector). (d) Optical microscope image of the device. The emitter's graphene channel is rendered with enhanced colored contrast. Unless specifically stated, the pump beam focuses on the region labeled by the white diamond for both graphene devices and the control groups.

In this chapter, we start with our fabrication and characterization of the device with on-chip pump-probe spectroscopy. We observe an 80-time amplitude enhancement with the device working as a THz emitter, and an 800-time increase of responsivity as an infrared photodetector, both compared to the graphene-free control group. Then we introduce our study on the

underlying mechanism. Experimental results agree well with our proposed physical picture, with interlayer charge transfer as the dominating mechanism. The work presents a good example demonstrating that the ultrafast interlayer interactions can complement 2D material properties with 3D ones for a better device performance unparalleled by either of the materials alone. We conclude the chapter with our vision for such 2D-3D heterostructures for THz optoelectronic applications.

6.2 Device Fabrication and Characterization

Fig. 6.1(c)(d) shows the device structure and the on-chip pump-probe measurement setup. The device was fabricated on a silicon-on-sapphire substrate. We implanted O^+ ions into the silicon layer to introduce recombination centers. The recombination lifetime of the excited carriers reduces to 0.7 ps[150,151] at optimized implantation flux. A graphene channel connects the gold contacts that also serve as double-stripe THz waveguides[152].

We apply 0V to 10V bias across the graphene channel during the on-chip pump-probe measurement. The laser source is a Ti:sapphire laser mode-locked at 800 nm, with a pulse duration < 100 fs. The ultrafast hot carrier dynamics generate a THz field that couples to the coplanar waveguide. After 100-μm propagation, the signal reaches an Auston switch. A probe pulse gates the Auston switch to sample the transient THz field. We tune the time-delay between the pump and probe beam via a motorized delay line (see Chapter 3). A chopper modulates the pump beam at 2.5 kHz. A lock-in amplifier captures the electrical signal at this frequency for improved SNR.

6.3 THz Emission and Photocurrent Enhancement

Fig. 6.2(a) shows our measurement results with different bias voltage across the channel. The emission amplitude is linearly dependent on the applied bias. We also tested a control device without graphene on top. The device has the same geometry and is measured with identical illumination and bias condition. The amplitude enhancement is universal for different biases and

pump powers (Fig. 6.2(b)). We observe a maximum gain of 80 times (19 dB) for a low bias at 10 mW. Notice that this is not the ultimate limit, since gating and improved material properties will also improve the enhancement, as discussed later. Most notably, the enhancement factor increases for a higher pump power around 10 mW. This indicates a higher saturation threshold at high pump power for our device, which is desirable for high-efficiency THz emitters.

We then confirm the emitted signal's bandwidth with the Fourier-transformed emission spectra. We observe no bandwidth decrease in our device. Another important metric for THz emitters is the SNR. RCL circuit modeling suggests decreased channel resistance in general couples more thermal noise to the electromagnetic field emitted[153]. Despite a 10-time higher noise level due to graphene's higher conductivity, the signal's amplification is even larger. The SNR increases by more than 2 times. Concretely, the inserted graphene layer enables a significant gain in emission without sacrifice on either bandwidth or SNR.

We also examine the photocurrent extracted from the device. Unlike the emitted THz field, the photocurrent has a nonlinear dependence on the channel bias (Fig. 6.2 (d)). Additional spatially-resolved measurement (Fig. 6.3) also suggests that the photocurrent collection is most efficient at the edge, different from the THz field emission results. Photocurrent autocorrelation (Fig. 6.2 (e)) suggests intrinsic carrier dynamics with full-width-half-magnitude (FWHM) of 0.3 ps, which is even faster than the THz emission observations. More interestingly, the photocurrent harvested is almost three orders of magnitude higher with graphene than the case without graphene. The measured responsivity is lower than devices in a few other works, which are measured at much lower optical power[154,155,156]. Nevertheless, the 2D-3D device shows excellent potential as high-responsivity photodetectors with THz operation bandwidth after further optimization.

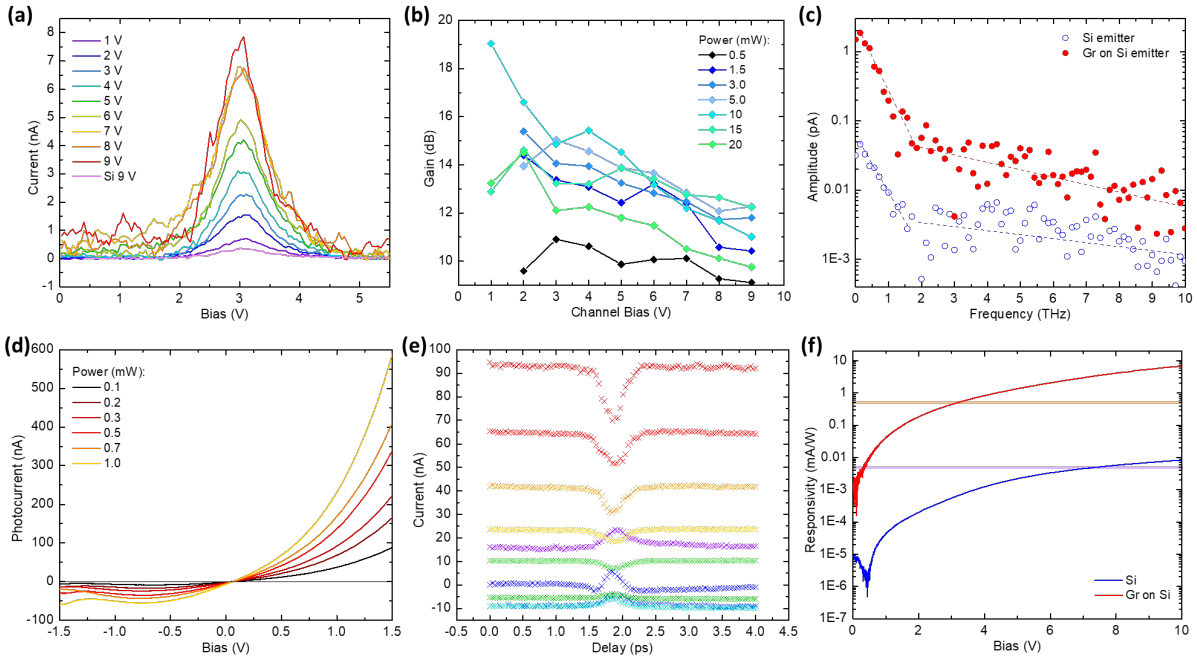

Figure 6.2. (a) Time-resolved measurement of THz emission under different bias, with pump power = 3 mW and probe power = 10 mW. (b) Amplitude enhancement over the graphene-free control group under different channel bias and pump power. The 2D-3D heterostructure device showed universal enhancement over an order of magnitude, with a gain of 80 times at small bias. (c) Fourier-transformed emission spectra of the two devices demonstrate decent bandwidth and SNR after the enhancement. (d) Photocurrent from the device under various powers. The nonlinear bias dependence may originate from local band alignment change under different biases. (e) Photocurrent autocorrelation with the pump beam (1 mW) and probe beam (0.5 mW) illuminating the same region on the device. Different colors correspond to a 0.2-V stepped bias change across the channel from -1 V (violet) to 1V (crimson). The FWHM of the peak is 0.3 ps for 1V bias. (f) Responsivity comparison of 2D-3D devices and the graphene-free counterpart. The insertion of the graphene layer results in about 800 times higher responsivity than the typical Auston switch. Light orange bar: reported responsivity of unbiased exfoliated graphene at metal edges; light violet bar: reported responsivity of unbiased CVD-grown graphene at metal edges contributed by lateral photo-Dember effect[16].

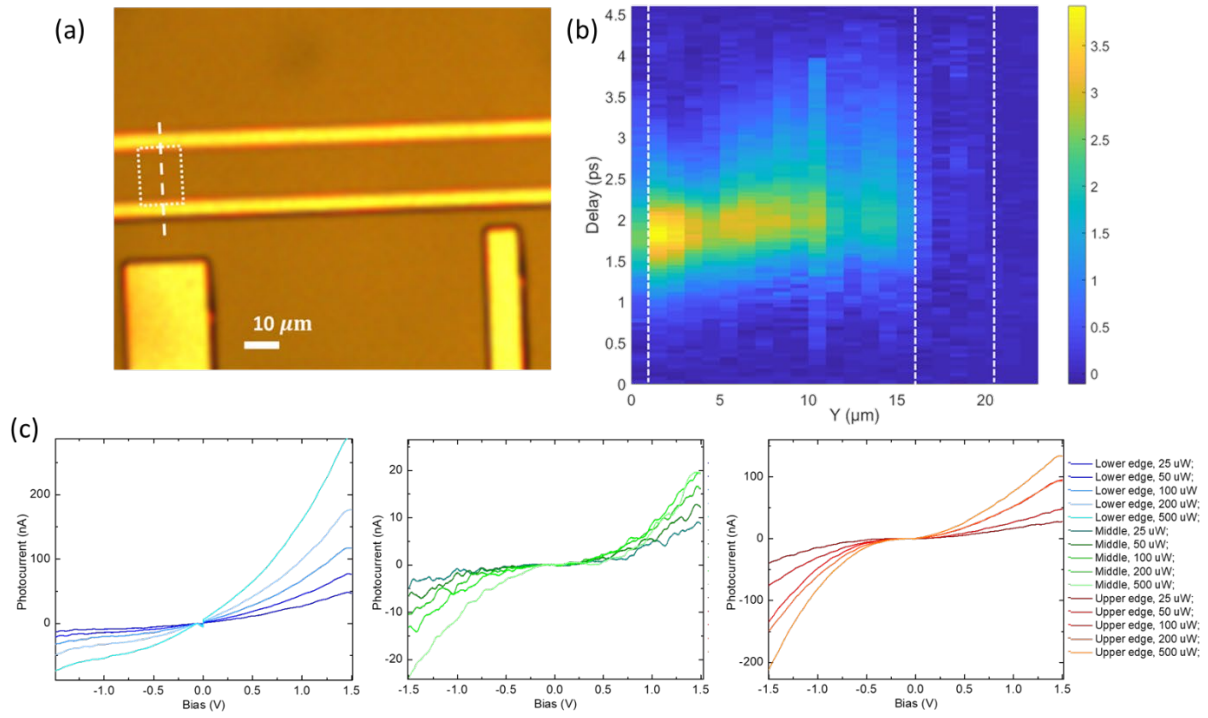

Figure 6.3. Spatially-resolved measurements of (b) THz emission and (c) photocurrent with excitation at different regions (white thick dashed line on the microscope image (a)) of the device. (b) The measurement shows significant, unlocalized THz emission throughout the channel. (c) With the beam centered at the upper and lower edge, the photocurrent is an order of magnitude larger than the case with the beam centered in the channel's center. We also observe a stronger nonlinearity with sweeping channel bias at the edges.

6.4 Enhancement Mechanism: Graphene as Hot Carriers' Fast Lane

We analyze the enhancement mechanism of the THz emission and the photocurrent with the above observations. Though the photocurrent extraction is naturally edge-related due to a limited carrier travel length, the THz enhancement is not. Scanning the pump beam along the channel gives large THz emission at and far away from the edge (Fig. 6.3). The observation, combined with the linear bias-amplitude dependence, eliminates the possibilities of edge effects as the dominating mechanism for THz emission enhancement, such as photo-thermoelectric and photovoltaic effects.

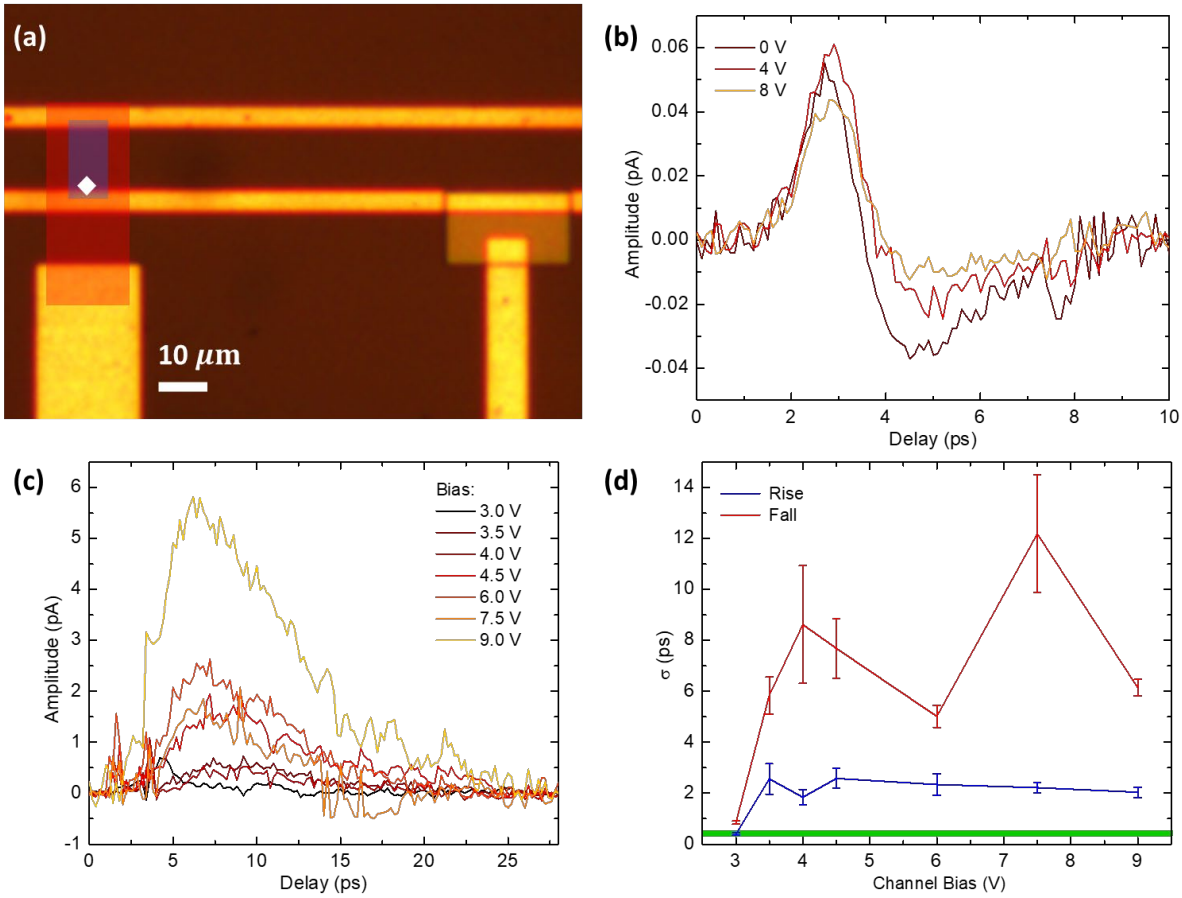

Figure 6.4. Additional control groups for THz emission mechanism studies. (a) Optical microscope image of the device with no silicon beneath graphene, red and blue rectangle shows the graphene gate and the channel, respectively. The graphene gate structure is also used in measurements shown in Fig. 6.5. The THz emission is excited at the metal-graphene edge, as indicated by the white diamond. (b) THz emission from the pure graphene device under different channel bias at the pump power of 5 mW and probe power of 30 mW. (c) THz emission from same 2D-3D heterostructure with a lightly implanted silicon substrate. (d) Extracted rise and fall time through Gaussian fit. The values are much larger compared to the values in heavily implanted devices (green banner).

We further understand graphene's role with evidence from two control groups: The first device is a silicon-free, pure graphene emitter; the second device is a graphene-silicon emitter with a lightly implanted silicon layer. We illuminated the device at the metal-graphene edge in the pure graphene sample and applied different channel biases. The pump-probe measurement showed two orders-of-magnitude smaller amplitudes, even with higher pump and probe power. The bias dependence showed the edge effect dominating the THz emission, contrary to the previous observations of a strong photoconductive effect137. This is because the beam is focused on the

edge in our test. The larger beam size used in the other experiment downplays the edge effects and makes the photoconductive effect stronger.

In the second control device, the lower defect density leads to a longer carrier lifetime in lightly-implanted silicon. Fig. 6.4 (c)(d) shows longer rise and fall times of the THz signal. The two control groups suggest that the carriers excited in silicon are the emission's major power source. The graphene layer can only make a difference later in either the carrier separation process or subsequent emitter-waveguide coupling.

A few remaining mechanisms could contribute to the THz emission besides the proposed charge transfer (CT) process. For example, graphene may change the circuit impedance, enabling more efficient field-coupling into the waveguide. Another possibility is non-radiative charge transfer (NRET) between the silicon and graphene layer, which also couples significant energy into hot carriers in graphene. To differentiate the mechanisms, we further fabricate graphene top gates and study the device's gate-dependent performance.

The graphene transfer curve in Fig. 6.5 (a) is asymmetric, with the n-branch current not going up as expected. We fixed the channel bias at 0 V and probed the photocurrent at sweeping gate bias with scanning photocurrent spectroscopy. The photocurrent flips sign under sweeping gate bias at regions sufficiently far from the edge built-in field. This indicates inversed vertical built-in field at the graphene-silicon interface under various gating. Fig 6.5 (c) is a band diagram consistent with the observed transfer curve and photocurrent polarity. Under negative bias, the graphene channel is p-doped and depletes the silicon layer. Under positive bias, the top gate has an n-doping effect on the graphene channel. However, the vertical band distortion drags the silicon layer to electron accumulation. The underneath accumulated electrons p-dope the graphene, partially compensating the gate tuning over channel conductance. The band diagram is consistent with our observations and previous reports claiming O^+ ions in silicon as a donor[157]. C-V measurements unveil parasitic graphene-silicon capacitance, further verifying the proposed band diagram (see Fig. 6.6).

We then sweep the gate bias and measure the peak THz emission amplitude. The amplitude follows an M-shaped gate dependence (Fig. 6.5 (d)). Such results exclude two of the remaining mechanisms as the dominant contributor to the enhanced emission: Addition of the graphene layer increases the conductance of the emitter channel, which may lead to enhanced coupling to

the waveguide. If this is the dominating mechanism, the emission amplitude should follow the channel conductance change, which contradicts our observations. On the other hand, the NRET process generates electron-hole pairs in graphene via dipole-dipole interactions. Theoretical works suggest these dipole interactions' strength monotonically decrease as the environment's permittivity increase[158]. While Kramers-Kronig relations can predict silicon's permittivity change under doping[159,160], the presence of defects, together with the graphene doping effect[161], adds complexities to a precise prediction. However, the NRET process shall not be suppressed to zero and create a sharp dip around 3 V gate bias, with no significant charge accumulation in either graphene or silicon. The observed complex gate dependence cannot be explained with the NRET model.

The CT process offers a reasonable explanation for the gate dependence. As is evident in Fig. 6.5 (b), the band alignment is flat near 0 V. In the flat band case, the CT process is suppressed due to the absence of a built-in electric field. This explains the zero amplitude observed in the middle. For large positive and negative biases, the graphene layer has lower mobility due to increased carrier-carrier interactions[16]. Hence a weaker dipole moment is generated within the shorter hot carrier lifetime. The combination of the two effects gives birth to the M-shape observed. The small amplitude in the middle indicates that other competing mechanisms, including NRET and vertical photo-Dember effect, are at least an order of magnitude weaker in contribution to the THz emission. Previous observations in graphene-diamond systems indicate NRET's dominance over CT[162,163,164]. This is possibly due to the high energy barrier for charge transport in the diamond crystal. Carriers are much more mobile in the silicon-graphene system, so that CT dominates the ultrafast process.

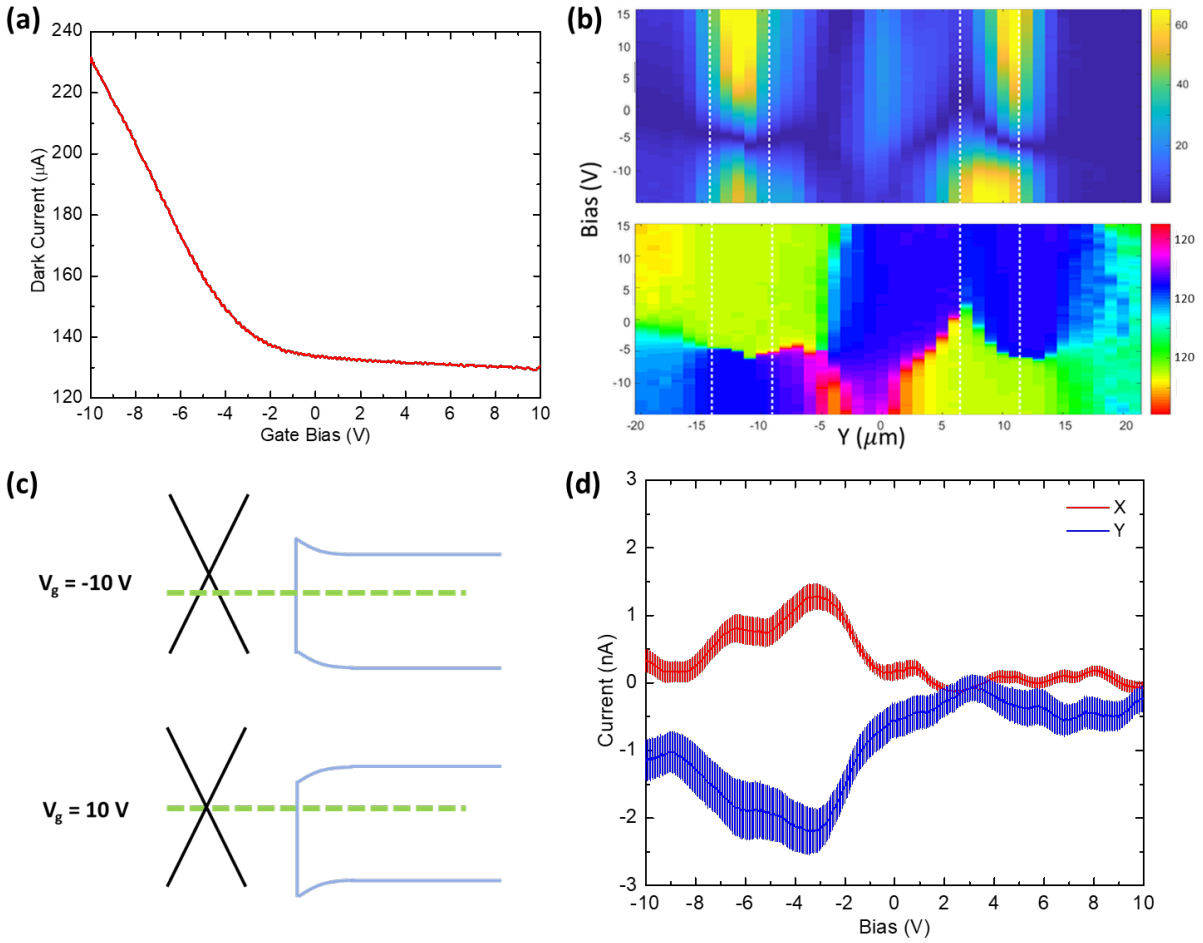

Figure 6.5. Gate dependence of graphene-silicon device performance. (a) Current across the device under 1V source-drain bias and varied gate bias. (b) The amplitude (upper) and phase (lower) of the photocurrent under scanned beam position and gate bias. The channel bias fixes at 0 V. (c) The band alignment diagram for the device based on (a) and (b). (d) The peak THz emission amplitude (with error bars) under various gate biases. X and Y channels are used for tracking the phase change of emission amplitude.

.

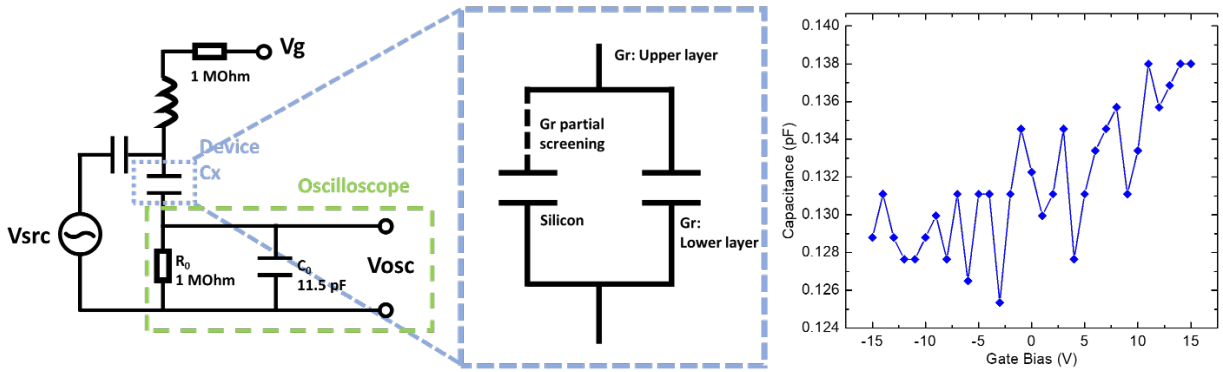

Figure 6.6. Measurement circuitry for gate capacitance extraction. Parasitic capacitance between silicon and graphene channel exists due to partial screening of field through graphene. The C-V measurements are performed at 2 MHz source frequency. At this frequency and circuit parameters, we approximately have $\frac{V_{osc}}{V_{src}} \cong \frac{C_x}{C_0}$. This equation enables us to extract the gate capacitance. Right: increase of total capacitance due to DC gating.

The picture of CT as the dominant mechanism is consistent with our proposed strategy for efficient carrier separation. Graphene is an essential building block of the device. Despite the fact that high electron mobility transistors (HEMT) can also provide considerably high mobility after the CT process, the device would be more challenging to fabricate to maintain a good interface between the absorber layer and the high-mobility channel. The Van der Waals interaction between graphene and other materials allows easy fabrication with good interface qualities. More improvements can also be made to the device fabrication process: the graphene we used has modest mobility of 400 $cm^2V^{-1}s^{-1}$ as extracted from FET and CV measurements due to the poor growth quality. This limits the carrier extraction efficiency. Furthermore, excited carriers in low-temperature-grown GaAs (LT-GaAs) relax faster and travels longer. LT-GaAs and high-quality graphene can further boost the THz emission amplitude and photodetection responsivity in various applications. Additionally, both impedance matching in THz emission and dark noise reduction in photodetection demands a reduced channel conductance. Advanced device structure designs are necessary for further improvements.

6.5 Conclusion

By inserting a graphene layer as the hot-carrier fast lane in a silicon Auston switch, we demonstrated significant amplitude enhancement of the device as a THz emitter, together with a giant responsivity increase as a photodetector. Despite the earlier expectations of weak THz emission in graphene-based devices[165], our work shows that a combination of graphene and traditional bulk materials can surpass both materials as a THz emitter. Further developments on similar systems will point to high-performance THz emitters and ultrafast photodetectors. More generally, this work is an example demonstrating the potential of 2D-3D heterostructures. The design inspires novel engineering over ultrafast hot carrier dynamics in 2D and 3D

heterostructures. The materials' desired properties can complement each other for important applications.

Chapter 7
Conclusion

7.1 Summary

The thesis presents three example works that harness the ultrafast hot carrier dynamics in graphene heterostructures for optoelectronic applications. At the device level, we design various heterojunctions for efficient separation and extraction of hot carriers. The devices' unique properties allow us to take specific strategies to make them useful, either through supreme performance enhancement or unique system design that is only made possible by the special device properties.

In Chapter 4, we added gate tunability to a graphene phototransistor. By doing so, the detector gains a spectrally-selective response. We use computational spectroscopy algorithms, namely least-square linear regression, to convert the gate and wavelength-dependent photocurrent into reconstructed light source spectra. The system features unprecedented compactness compared to other spectrometer designs. It can lead to promising applications in miniaturized spectroscopy and multi-spectral imaging.

In Chapter 5, we take advantage of the phototransistor from another perspective: its high transparency. We fabricate transparent photodetector arrays and assemble them into a multi-focal plane imaging system. Fully connected neural networks process the photocurrent collected from different focal planes and predict the 3D configuration information of the object. The system is a compact, high-speed and power-efficient solution for 3D information acquisition, which is useful in autonomous vehicles and AR/VR applications.

Lastly, Chapter 6 introduces another device design approach that uses graphene as a fast lane for hot carriers jammed in photoconductive switches. The additional graphene layer results in

orders-of-magnitude enhancements when operating the device as both THz emitters and high-speed photodetectors. We confirm charge transfer at the 2D-3D interface as the contributing mechanism, which is consistent with our device design philosophy. The work provides a new design strategy for future ultrafast optoelectronic devices.

7.2 Learning from Mistakes

The conclusion part of this thesis provides unique opportunities to learn from mistakes. We start with a reflection on the three projects, followed by a discussion aiming to probe nanodevice development's common pitfalls.

The graphene spectrometer introduced in Chapter 4 suffers significant experimental deviation from theory. The poor device quality, especially the defective tunneling barrier, prevents the ideal spectral reconstructions with a simple linear model.

On the other hand, the applied light source was not favorable. OPA signal beams through narrow bandpass filters have a short pulse duration. The high instantaneous power creates thermal pathways in the photodetection mechanism. Secondly, the beam's large spatial dispersion prohibits proper focusing at multiple wavelengths, so that only single-peak spectra are tested. We have to manually adjust the dispersion-caused misalignment every time we shift the testing wavelength. The ideal light source should support continuous waves at a broad spectral range, with little spatial dispersion and sufficient luminescence. Supercontinuum sources are good choices.

Starting with exfoliated 2D heterostructures and corresponding fabrication infrastructures, together with proper light sources, could have significantly improved the outcome. To my great regret, we spent months streamlining existing processes without critical changes towards a cleaner system.

Chapter 5 discussed the multi-focal-plane imaging system with experimental data from two layers of 4-by-4 sensor arrays. For the first few months, the critical problems are: (1) How large arrays can we make with our processes? (2) What detection function can we achieve with the array?

We left the second question open until the very end of the project. The upside is that we avoided device performance uncertainty. The downside is that we had no system-level guidance towards a more mature functionality.

We eventually achieved 99% device yield yet stopped at testing data with a small array and only two layers. We could have stacked 5 or more layers and 8-by-8 arrays for more complex 3D object detections. Imagine a better package that soaks 5 layers in a plastic tank filled with the proper oil for perfect refractive index compensation. With the whole imager stack packed in a transparent box, the demonstration could have advanced one step further towards product-level maturity.

Another key issue we neglected until the very end is the device performance. The phototransistor's speed and noise were later found to be crucial in implementing the device to ambient illuminations. Much work could have been done at the beginning to further enable high-speed, high-response, low noise devices (see Section 5.2.2). Moreover, the graphene channel's large dark current is highly unwelcome for further scaling up the system with scanning lines.

The THz emitter project has fewer pitfalls thanks to previous experiences. We avoided extended efforts on pure graphene systems, which provide a two-orders-of-magnitude lower emission amplitude and little new physics. The major problem comes again from the poor material choices. LT-GaAs is found to be 5-time more efficient for the transient hot carrier generation than amorphous silicon. Moreover, the poor CVD-grown graphene sample had very low mobility compared with the typical value. Much stronger signals were possible with more careful material choices at the beginning.

Another pity is the absence of free-space emission experiments. We planned to transfer a graphene layer to a commercial photoconductive switch and measure the THz emission power. This is solid evidence of graphene's potential for stronger THz emitters. However, due to the funding cut and the Covid-19 pandemic, the missing piece of the puzzle is lost.

7.2.1 General Methodology

The thesis's ultimate goal is to develop a reliable methodology to bring nanodevices to industry-level nano-systems. With the lessons learnt, we conclude with a tentative standard operation procedure that serves for other similar projects. It is a substitution of Heilmeier's Catechism[166] for our specific purpose. Nanoscale science and technologies are time-consuming and labor-intensive to explore. Doing the homework well is a must before getting hands dirty.

The butterfly-like diagram in Fig. 7.1 illustrates the thought process before the experimental works. We describe each step separately below:

Proved science and capabilities include the experimental findings that support the planned research. It is the initial reason for the exploration of the topic. Particularly, for nano + machine learning innovations described in the later section, the device should have the essential information encoded in either the input or the output. For example, in the graphene spectrometer project, the photoresponse curves' differences for various wavelength encodes spectral information. The encoded information can be decoded (using machine learning tools) to give useful outputs. Reversely, intuitive signals can be encoded into inputs of nano-systems for target functions.

Other material candidates may achieve similar functions. In that case, the originally proposed material/device is not the only possible route towards the new technology. We should carefully compare the key factors of the existing solutions (including remaining problems intrinsic to the solutions) to determine the best choice.

The **remaining problems** represent the imperfections in the previous demonstrations that may impact specific applications. Typical considerations for nanomaterials and devices include performance drifting, mass production feasibility, environmental (temperature, moisture, contamination, etc.) sensitivity, durability, noise level, speed, power efficiency, etc. Some properties are critical for the proposed application, while some are not. Each property may be strongly dependent on certain material growth, device structure, or fabrication process. For example, our work in Chapter 4 is sensitive to both graphene quality and barrier dielectric property, while Chapter 5's project works well with CVD-grown graphene. We could have made the right choices if we had a more thorough comprehension of the application's requirements imposed on the imperfect nanodevices.

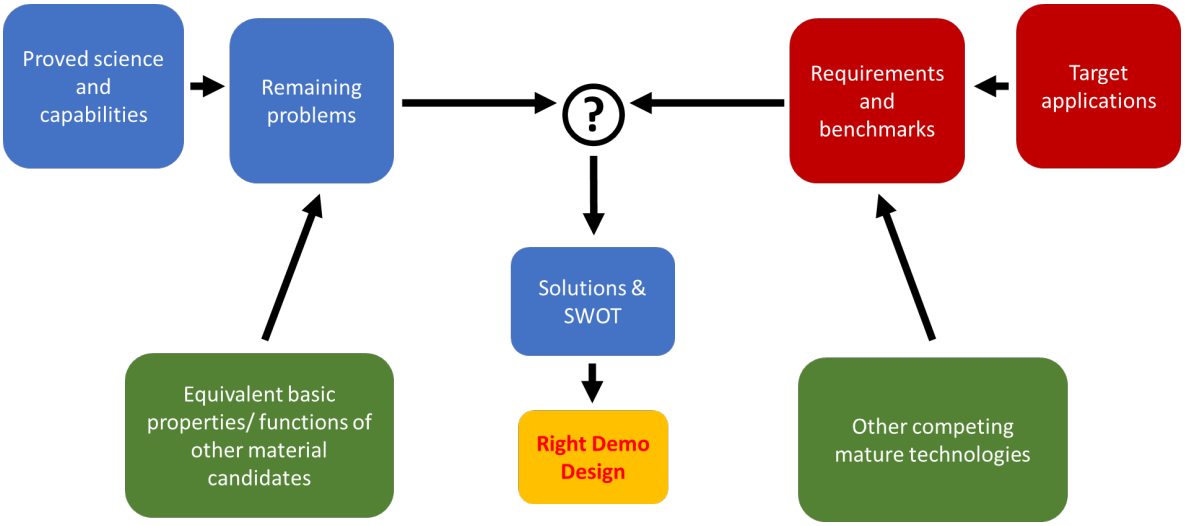

Fig. 7.1. The butterfly diagram illustrating the thought flow for making good research plans and decisions.

The **target applications** are conceived in the ideal case following real market demand. Other **competing technologies** may offer a developed solution. As discussed in Chapter 1, the valid innovation must overcome the barrier and provide significant figure of merits if mature technology already exists. To quantitatively address the issue, we should set **requirements and benchmarks** based on the competing technologies and application scenarios. Comparison over the material/device side and the product side eliminates most ideas and solutions. We can analyze the remaining solutions with SWOT or other reasoning methods to determine acceptable opportunities and risks. Then we can come up with the right **demo design**: It should be feasible given the limited resources in lab, and be advanced enough to showcase the innovation's potential in real applications. It is a delicate tradeoff. However, proper packaging, control system design, and choices of demonstrated functionalities can make substantial differences that convert the work from abstract toys to magic.

7.2.2 Face the Reality

However, any efforts to bridge nanoscale science and industrial applications is a long run. Researchers have to dance with the funding tempo, cope with unexpected outcomes, and

sometimes live through a global pandemic and political climate changes. Tradeoffs are always made to the butterfly diagram. Even worse, the proposed methodology does not lie on an objective basis: The scientific value of research depends on many aspects. Human perceptions of nature and research tastes can be highly subjective. The market influence of an innovation depends on even more subtle factors.

Like stock traders, maybe the best to do is to take the opportunities and avoid apparent bad decisions. The more careful and experienced we are, the wiser decisions we make.

7.3 Future Works: the Power of Nano-Optoelectronics + Machine Learning

The possible direct extensions of the presented works are already included in the previous sections. Here we extend the works from the methodology level, and discuss the necessities and possibilities of combining nanotechnology with machine learning algorithms.

In Chapter 4 and 5, we used machine learning algorithms to process data into the ultimate results that are useful for practical applications. The combination of nanodevices and machine learning is not a coincidence. Machine learning algorithms relax nanodevices' performance requirements in several aspects: (1) The intrinsic input and/or output of the nanodevices need not to be strictly the intuitive, ultimate result required by the application. The nanodevice only needs to perform the information conversion that randomly encodes the necessary information. The neural networks can work as an interface between the encoded information and the target input/output of the system. (2) The central conundrum for nanodevices' commercialization comes from the nonuniformity, nonlinearity, noise, drifting, and other imperfections. The learning process in the machine learning algorithms automatically accounts for these problems. For example, neural networks can compensate a nanodevice array's nonuniformity (see Chapter 5) simply by adjusting the weights in a single linear layer. Neural networks can be robust against noise and hardware drifting, though usually at the expense of a larger training dataset and a larger number of adjustable weights.

The design philosophy is not single-sided. Given the flexibility that only randomly encoded necessary information is required, nanodevices can advance to a previously unvisited regime. It

can perform sensing, modulation, and other functionalities in application contexts previously impossible. The miniaturized spectrometer and the ultra-compact 3D camera in Chapter 4 and 5 are two examples. With the synergic design of hardware and software, the nanodevices can prove new functionalities or perform existing functionalities with novel applicational advantages. Conventional design intuition may not apply in this approach. New insights from application-oriented design and inverse design strategies may be helpful in the future. The combination of nanodevices with machine learning forms a hardware-software reservoir computing system. It can become a new approach to link nanodevices, especially nano-sensors, to industry-level applications.

The above arguments stem from a device developer's perspective. The picture is even more intriguing from an Internet-of-things (IoT) perspective[167,168]. Sensors and smart devices will surround future human life. Some sensors need to provide logical feedbacks instead of analytical signals; some sensors' readout should be processed locally due to speed, communication bandwidth, energy, or privacy considerations. In either case, the deep hybrid of sensors and edge computation modules becomes necessary. A Lego-like assembly of general-purpose sensors and processor modules may eventually give ways to specifically designed intelligent sensing modules, especially with growing market demand for multiple specific purposes.

In conclusion, the synergic design of nanodevices and machine learning algorithms, as supported by our works, is a promising new approach to bring novel nanoscale physics to the corners of future households.

Reference:

[1] Wallace P R. The band theory of graphite[J]. Physical Review, 1947, 71(9): 622.
[2] McClure J W. Diamagnetism of graphite[J]. Physical Review, 1956, 104(3): 666.
[3] Novoselov K S, Geim A K, Morozov S V, et al. Electric field effect in atomically thin carbon films[J]. science, 2004, 306(5696): 666-669.
[4] Wang L, Meric I, Huang P Y, et al. One-dimensional electrical contact to a two-dimensional material[J]. Science, 2013, 342(6158): 614-617.
[5] Nair R R, Blake P, Grigorenko A N, et al. Fine structure constant defines visual transparency of graphene[J]. Science, 2008, 320(5881): 1308-1308.
[6] Xia F, Wang H, Xiao D, et al. Two-dimensional material nanophotonics[J]. Nature Photonics, 2014, 8(12): 899.
[7] Kim K S, Zhao Y, Jang H, et al. Large-scale pattern growth of graphene films for stretchable transparent electrodes[J]. nature, 2009, 457(7230): 706.
[8] Bae S, Kim H, Lee Y, et al. Roll-to-roll production of 30-inch graphene films for transparent electrodes[J]. Nature nanotechnology, 2010, 5(8): 574.
[9] Pospischil A, Furchi M M, Mueller T. Solar-energy conversion and light emission in an atomic monolayer p–n diode[J]. Nature nanotechnology, 2014, 9(4): 257.
[10] Baugher B W H, Churchill H O H, Yang Y, et al. Optoelectronic devices based on electrically tunable p–n diodes in a monolayer dichalcogenide[J]. Nature nanotechnology, 2014, 9(4): 262.
[11] Koppens F H L, Mueller T, Avouris P, et al. Photodetectors based on graphene, other two-dimensional materials and hybrid systems[J]. Nature nanotechnology, 2014, 9(10): 780.
[12] Zhao H, Guo Q, Xia F, et al. Two-dimensional materials for nanophotonics application[J]. Nanophotonics, 2015, 4(1): 128-142.
[13] Liu M, Yin X, Ulin-Avila E, et al. A graphene-based broadband optical modulator[J]. Nature, 2011, 474(7349): 64.
[14] Bao Q, Zhang H, Wang Y, et al. Atomic-layer graphene as a saturable absorber for ultrafast pulsed lasers[J]. Advanced Functional Materials, 2009, 19(19): 3077-3083.
[15] Martinez A, Sun Z. Nanotube and graphene saturable absorbers for fibre lasers[J]. Nature Photonics, 2013, 7(11): 842.
[16] Liu C H, Chang Y C, Lee S, et al. Ultrafast lateral photo-Dember effect in graphene induced by nonequilibrium hot carrier dynamics[J]. Nano letters, 2015, 15(6): 4234-4239.
[17] Reiss T, Hjelt K, Ferrari A C. Graphene is on track to deliver on its promises[J]. Nature nanotechnology, 2019, 14(10): 907-910.
[18] What is graphene? 2D Materials https://2dmsolutions.com/ products-services/what-is-graphene/ (2017).
[19] Graphene markets, technologies and opportunities 2014–2024 IDTechEx https://www.idtechex.com/research/articles/graphenemarkets-technologies-and-opportunities-2014-2024-00006555. asp (2014).
[20] Bringing reality to the hype, the total graphene market set for a modest $126 million in 2020. Lux R esearch http://blog. luxresearchinc.com/blog/2013/03/bringing-reality-to-the-hypethe-total-graphene-market-set-for-a-modest-126-millionin-2020/ (2013).
[21] Graphene materials for opto & electronic applications. Yole Développement http://www.yole.fr/iso_upload/News/2014/ PR_Graphene_YOLE%20DEVELOPPEMENT_January%202014. pdf (2014).
[22] Kong W, Kum H, Bae S H, et al. Path towards graphene commercialization from lab to market[J]. Nature nanotechnology, 2019, 14(10): 927-938.
[23] Tournié E, Cerutti L. Mid-infrared Optoelectronics[J]. 2019.
[24] Huang P Y, Ruiz-Vargas C S, Van Der Zande A M, et al. Grains and grain boundaries in single-layer graphene atomic patchwork quilts[J]. Nature, 2011, 469(7330): 389.
[25] Neto A H C, Guinea F, Peres N M R, et al. The electronic properties of graphene[J]. Reviews of modern physics, 2009, 81(1): 109.
[26] Physics of graphene[M]. Springer Science & Business Media, 2013.
[27] Novoselov K S, Geim A K, Morozov S V, et al. Two-dimensional gas of massless Dirac fermions in graphene[J]. nature, 2005, 438(7065): 197.
[28] Geim A K, Novoselov K S. The rise of graphene[M]//Nanoscience and Technology: A Collection of Reviews from Nature Journals. 2010: 11-19.
[29] Ando T, Nakanishi T, Saito R. Berry's phase and absence of back scattering in carbon nanotubes[J]. Journal of the Physical Society of Japan, 1998, 67(8): 2857-2862.
[30] McEuen P L, Bockrath M, Cobden D H, et al. Disorder, pseudospins, and backscattering in carbon nanotubes[J]. Physical Review Letters, 1999, 83(24): 5098.
[31] Bolotin K I, Sikes K J, Jiang Z, et al. Ultrahigh electron mobility in suspended graphene[J]. Solid State Communications, 2008, 146(9-10): 351-355.
[32] Hass J, Feng R, Li T, et al. Highly ordered graphene for two dimensional electronics[J]. Applied Physics Letters, 2006, 89(14): 143106.

[33] Emtsev K V, Speck F, Seyller T, et al. Interaction, growth, and ordering of epitaxial graphene on SiC {0001} surfaces: A comparative photoelectron spectroscopy study[J]. Physical Review B, 2008, 77(15): 155303.
[34] Li X, Cai W, An J, et al. Large-area synthesis of high-quality and uniform graphene films on copper foils[J]. science, 2009, 324(5932): 1312-1314.
[35] Xu X, Zhang Z, Dong J, et al. Ultrafast epitaxial growth of metre-sized single-crystal graphene on industrial Cu foil[J]. Science bulletin, 2017, 62(15): 1074-1080.
[36] Mattevi C, Kim H, Chhowalla M. A review of chemical vapour deposition of graphene on copper[J]. Journal of Materials Chemistry, 2011, 21(10): 3324-3334.
[37] Caldwell J D, Anderson T J, Culbertson J C, et al. Technique for the dry transfer of epitaxial graphene onto arbitrary substrates[J]. ACS nano, 2010, 4(2): 1108-1114.
[38] Dean C R, Young A F, Meric I, et al. Boron nitride substrates for high-quality graphene electronics[J]. Nature nanotechnology, 2010, 5(10): 722.
[39] Mayorov A S, Gorbachev R V, Morozov S V, et al. Micrometer-scale ballistic transport in encapsulated graphene at room temperature[J]. Nano letters, 2011, 11(6): 2396-2399.
[40] Zhou, Minmin, et al. "Photoresist as a choice of molecularly thin gate dielectrics in graphene-based devices." APL Materials 9.3 (2021): 031104.
[41] Dawlaty J M, Shivaraman S, Chandrashekhar M, et al. Measurement of ultrafast carrier dynamics in epitaxial graphene[J]. Applied Physics Letters, 2008, 92(4): 042116.
[42] Strait J H, Wang H, Shivaraman S, et al. Very slow cooling dynamics of photoexcited carriers in graphene observed by optical-pump terahertz-probe spectroscopy[J]. Nano letters, 2011, 11(11): 4902-4906.
[43] Graham M W, Shi S F, Ralph D C, et al. Photocurrent measurements of supercollision cooling in graphene[J]. Nature Physics, 2013, 9(2): 103.
[44] Lee E J H, Balasubramanian K, Weitz R T, et al. Contact and edge effects in graphene devices[J]. Nature nanotechnology, 2008, 3(8): 486.
[45] Mueller T, Xia F, Freitag M, et al. Role of contacts in graphene transistors: A scanning photocurrent study[J]. Physical Review B, 2009, 79(24): 245430.
[46] Park J, Ahn Y H, Ruiz-Vargas C. Imaging of photocurrent generation and collection in single-layer graphene[J]. Nano letters, 2009, 9(5): 1742-1746.
[47] Xia F, Mueller T, Golizadeh-Mojarad R, et al. Photocurrent imaging and efficient photon detection in a graphene transistor[J]. Nano letters, 2009, 9(3): 1039-1044.
[48] Xia F, Mueller T, Lin Y, et al. Ultrafast graphene photodetector[J]. Nature nanotechnology, 2009, 4(12): 839.
[49] Mueller T, Xia F, Avouris P. Graphene photodetectors for high-speed optical communications[J]. Nature photonics, 2010, 4(5): 297.
[50] Freitag M, Low T, Xia F, et al. Photoconductivity of biased graphene[J]. Nature Photonics, 2013, 7(1): 53.
[51] Long, Mingsheng, et al. "Broadband photovoltaic detectors based on an atomically thin heterostructure." Nano letters 16.4 (2016): 2254-2259.
[52] Kasap S O, Sinha R K. Optoelectronics and photonics: principles and practices[M]. New Jersey: Prentice Hall, 2001.
[53] Konstantatos G, Badioli M, Gaudreau L, et al. Hybrid graphene–quantum dot phototransistors with ultrahigh gain[J]. Nature nanotechnology, 2012, 7(6): 363.
[54] Liu, Chang-Hua, et al. "Graphene photodetectors with ultra-broadband and high responsivity at room temperature." Nature nanotechnology 9.4 (2014): 273.
[55] Zhang D, Cheng G, Xu Z, et al. Electrically tunable photoresponse in a graphene heterostructure photodetector[C]//2017 Conference on Lasers and Electro-Optics (CLEO). IEEE, 2017: 1-2.
[56] Ashcroft N W, Mermin N D. Solid state physics (saunders college, philadelphia, 1976)[J]. Appendix N, 2010.
[57] Cutler M, Mott N F. Observation of Anderson localization in an electron gas[J]. Physical Review, 1969, 181(3): 1336.
[58] Lemme M C, Koppens F H L, Falk A L, et al. Gate-activated photoresponse in a graphene p–n junction[J]. Nano letters, 2011, 11(10): 4134-4137.
[59] Gabor N M, Song J C W, Ma Q, et al. Hot carrier–assisted intrinsic photoresponse in graphene[J]. Science, 2011, 334(6056): 648-652.
[60] Song J C W, Rudner M S, Marcus C M, et al. Hot carrier transport and photocurrent response in graphene[J]. Nano letters, 2011, 11(11): 4688-4692.
[61] Xu X, Gabor N M, Alden J S, et al. Photo-thermoelectric effect at a graphene interface junction[J]. Nano letters, 2009, 10(2): 562-566.
[62] Liu C H, Dissanayake N M, Lee S, et al. Evidence for extraction of photoexcited hot carriers from graphene[J]. ACS nano, 2012, 6(8): 7172-7176.
[63] Ma Q, Lui C H, Song J C W, et al. Giant intrinsic photoresponse in pristine graphene[J]. Nature nanotechnology, 2019, 14(2): 145.
[64] Fong K C, Schwab K C. Ultrasensitive and wide-bandwidth thermal measurements of graphene at low temperatures[J]. Physical Review X, 2012, 2(3): 031006.
[65] Yan J, Kim M H, Elle J A, et al. Dual-gated bilayer graphene hot-electron bolometer[J]. Nature nanotechnology, 2012, 7(7): 472.

[66] Guo Q, Yu R, Li C, et al. Efficient electrical detection of mid-infrared graphene plasmons at room temperature[J]. Nature materials, 2018: 1.
[67] Furchi, Marco, et al. "Microcavity-integrated graphene photodetector." Nano letters 12.6 (2012): 2773-2777.
[68] Kang, Pilgyu, et al. "Crumpled Graphene Photodetector with Enhanced, Strain-Tunable, and Wavelength-Selective Photoresponsivity." Advanced Materials 28.23 (2016): 4639-4645.
[69] Fang, Zheyu, et al. "Graphene-antenna sandwich photodetector." Nano letters 12.7 (2012): 3808-3813.
[70] Fang, Zheyu, et al. "Plasmon-induced doping of graphene." Acs Nano 6.11 (2012): 10222-10228.
[71] Pile, David FP. "Graphene gets gap plasmons." Nature Photonics 13.2 (2019): 72.
[72] Gan, Xuetao, et al. "Chip-integrated ultrafast graphene photodetector with high responsivity." Nature Photonics 7.11 (2013): 883.
[73] Wang, Xiaomu, et al. "High-responsivity graphene/silicon-heterostructure waveguide photodetectors." Nature Photonics 7.11 (2013): 888.
[74] Pospischil, Andreas, et al. "CMOS-compatible graphene photodetector covering all optical communication bands." Nature Photonics 7.11 (2013): 892.
[75] Prechtel L, Song L, Schuh D, et al. Time-resolved ultrafast photocurrents and terahertz generation in freely suspended graphene[J]. Nature communications, 2012, 3: 646.
[76] Yadav D, Tombet S B, Watanabe T, et al. Terahertz wave generation and detection in double-graphene layered van der Waals heterostructures[J]. 2D Materials, 2016, 3(4): 045009.
[77] Obraztsov P A, Kanda N, Konishi K, et al. Photon-drag-induced terahertz emission from graphene[J]. Physical Review B, 2014, 90(24): 241416.
[78] Maysonnave J, Huppert S, Wang F, et al. Terahertz generation by dynamical photon drag effect in graphene excited by femtosecond optical pulses[J]. Nano letters, 2014, 14(10): 5797-5802.
[79] Tong J, Muthee M, Chen S Y, et al. Antenna enhanced graphene THz emitter and detector[J]. Nano Letters, 2015, 15(8): 5295-5301.
[80] Yao B, Liu Y, Huang S W, et al. Broadband gate-tunable terahertz plasmons in graphene heterostructures[J]. Nature Photonics, 2018, 12(1): 22.
[81] Gallegos D, Long K D, Yu H, et al. Label-free biodetection using a smartphone[J]. Lab on a Chip, 2013, 13(11): 2124-2132.
[82] Edwards P, Zhang C, Zhang B, et al. Smartphone based optical spectrometer for diffusive reflectance spectroscopic measurement of hemoglobin[J]. Scientific reports, 2017, 7(1): 12224.
[83] Bao J, Bawendi M G. A colloidal quantum dot spectrometer[J]. Nature, 2015, 523(7558): 67.
[84] Sahoo S K, Tang D, Dang C. Single-shot multispectral imaging with a monochromatic camera[J]. Optica, 2017, 4(10): 1209-1213.
[85] Redding B, Liew S F, Sarma R, et al. Compact spectrometer based on a disordered photonic chip[J]. Nature Photonics, 2013, 7(9): 746.
[86] Kita D M, Miranda B, Favela D, et al. High-performance and scalable on-chip digital Fourier transform spectroscopy[J]. Nature communications, 2018, 9(1): 4405.
[87] Souza M C M M, Grieco A, Frateschi N C, et al. Fourier transform spectrometer on silicon with thermo-optic non-linearity and dispersion correction[J]. Nature communications, 2018, 9(1): 665.
[88] Muneeb M, Vasiliev A, Ruocco A, et al. III-V-on-silicon integrated micro-spectrometer for the 3 μm wavelength range[J]. Optics express, 2016, 24(9): 9465-9472.
[89] Liapis A C, Gao B, Siddiqui M R, et al. On-chip spectroscopy with thermally tuned high-Q photonic crystal cavities[J]. Applied Physics Letters, 2016, 108(2): 021105.
[90] Yu M, Okawachi Y, Griffith A G, et al. Silicon-chip-based mid-infrared dual-comb spectroscopy[J]. Nature communications, 2018, 9(1): 1869.
[91] Dutt A, Joshi C, Ji X, et al. On-chip dual-comb source for spectroscopy[J]. Science advances, 2018, 4(3): e1701858.
[92] Ycas G, Giorgetta F R, Baumann E, et al. High-coherence mid-infrared dual-comb spectroscopy spanning 2.6 to 5.2 μm[J]. Nature Photonics, 2018, 12(4): 202.
[93] Zhang C, Cheng G, Edwards P, et al. G-Fresnel smartphone spectrometer[J]. Lab on a Chip, 2016, 16(2): 246-250.
[94] Sorak D, Herberholz L, Iwascek S, et al. New developments and applications of handheld Raman, mid-infrared, and near-infrared spectrometers[J]. Applied Spectroscopy Reviews, 2012, 47(2): 83-115.
[95] Ferrari M, Quaresima V. A brief review on the history of human functional near-infrared spectroscopy (fNIRS) development and fields of application[J]. Neuroimage, 2012, 63(2): 921-935.
[96] Mak, Kin Fai, et al. "Optical spectroscopy of graphene: from the far infrared to the ultraviolet." Solid State Communications 152.15 (2012): 1341-1349.
[97] Xia, Fengnian, Hugen Yan, and Phaedon Avouris. "The interaction of light and graphene: basics, devices, and applications." Proceedings of the IEEE 101.7 (2013): 1717-1731.
[98] Lee, Seunghyun, et al. "Homogeneous bilayer graphene film based flexible transparent conductor." Nanoscale 4.2 (2012): 639-644.
[99] Hastie T, Qian J. Glmnet vignette[J]. Retrieve from http://www. web. stanford. edu/~ hastie/Papers/Glmnet_Vignette. pdf. Accessed September, 2014, 20: 2016.
[100] Mullen K M, Van Stokkum I H M. nnls: The Lawson-Hanson algorithm for non-negative least squares (NNLS)[J]. 2007.

[101] Wang H, Strait J H, George P A, et al. Ultrafast relaxation dynamics of hot optical phonons in graphene[J]. Applied Physics Letters, 2010, 96(8): 081917.
[102] Tielrooij K J, Song J C W, Jensen S A, et al. Photoexcitation cascade and multiple hot-carrier generation in graphene[J]. Nature Physics, 2013, 9(4): 248.
[103] Brida D, Tomadin A, Manzoni C, et al. Ultrafast collinear scattering and carrier multiplication in graphene[J]. Nature communications, 2013, 4: 1987.
[104] Hong X, Kim J, Shi S F, et al. Ultrafast charge transfer in atomically thin MoS 2/WS 2 heterostructures[J]. Nature nanotechnology, 2014, 9(9): 682.
[105] Ma Q, Andersen T I, Nair N L, et al. Tuning ultrafast electron thermalization pathways in a van der Waals heterostructure[J]. Nature Physics, 2016, 12(5): 455.
[106] Sinha D, Lee J U. Ideal graphene/silicon Schottky junction diodes[J]. Nano letters, 2014, 14(8): 4660-4664.
[107] Lenzlinger M, Snow E H. Fowler-Nordheim tunneling into thermally grown SiO2[J]. Journal of Applied physics, 1969, 40(1): 278-283.
[108] Haigh, S. J., et al. "Cross-sectional imaging of individual layers and buried interfaces of graphene-based heterostructures and superlattices." arXiv preprint arXiv:1206.6698 (2012).
[109] Georgiou, Thanasis, et al. "Vertical field-effect transistor based on graphene-WS2 heterostructures for flexible and transparent electronics." Nature nanotechnology 8.2 (2013): 100-103.
[110]Hashem I E, Rafat N H, Soliman E A. Theoretical study of metal-insulator-metal tunneling diode figures of merit[J]. IEEE Journal of Quantum Electronics, 2012, 49(1): 72-79.
[111] Simmons J G. Generalized formula for the electric tunnel effect between similar electrodes separated by a thin insulating film[J]. Journal of applied physics, 1963, 34(6): 1793-1803.
[112] Tse W K, Sarma S D. Energy relaxation of hot Dirac fermions in graphene[J]. Physical Review B, 2009, 79(23): 235406.
[113] Bistritzer R, MacDonald A H. Electronic cooling in graphene[J]. Physical Review Letters, 2009, 102(20): 206410.
[114] Lee G H, Yu Y J, Lee C, et al. Electron tunneling through atomically flat and ultrathin hexagonal boron nitride[J]. Applied physics letters, 2011, 99(24): 243114.
[115] Tan Y W, Zhang Y, Bolotin K, et al. Measurement of scattering rate and minimum conductivity in graphene[J]. Physical review letters, 2007, 99(24): 246803.
[116] Fallahazad B, Lee K, Kang S, et al. Gate-tunable resonant tunneling in double bilayer graphene heterostructures[J]. Nano letters, 2015, 15(1): 428-433.
[117] Kokaly, R.F., Clark, R.N., Swayze, G.A., Livo, K.E., Hoefen, T.M., Pearson, N.C., Wise, R.A., Benzel, W.M., Lowers, H.A., Driscoll, R.L., and Klein, A.J., 2017, USGS Spectral Library Version 7 Data: U.S. Geological Survey data release, https://dx.doi.org/10.5066/F7RR1WDJ
[118] Liu, Nan, et al. "Large-area, transparent, and flexible infrared photodetector fabricated using PN junctions formed by N-doping chemical vapor deposition grown graphene." Nano letters 14.7 (2014): 3702-3708.
[119] Zheng, Zhaoqiang, et al. "Flexible, transparent and ultra-broadband photodetector based on large-area WSe2 film for wearable devices." Nanotechnology 27.22 (2016): 225501.
[120] Tsai, Shu-Yi, Min-Hsiung Hon, and Yang-Ming Lu. "Fabrication of transparent p-NiO/n-ZnO heterojunction devices for ultraviolet photodetectors." Solid-State Electronics 63.1 (2011): 37-41.
[121] Tanaka, Hideyuki, et al. "Transparent image sensors using an organic multilayer photodiode." Advanced Materials 18.17 (2006): 2230-2233.
[122] Stiebig, Helmut, et al. "Standing wave detection by thin transparent n–i–p diodes of amorphous silicon." Thin solid films 427.1-2 (2003): 152-156.
[123] Jovanov, Vladislav, et al. "Transparent Fourier transform spectrometer." Optics letters 36.2 (2011): 274-276.
[124] Niclass, Cristiano L., et al. "Light detection and ranging sensor." U.S. Patent Application No. 15/372,411.
[125] Oggier, Thierry, Scott T. Smith, and Andrew Herrington. "Line scan depth sensor." U.S. Patent Application No. 15/700,231.
[126] Schwarz, Brent. "LIDAR: Mapping the world in 3D." Nature Photonics 4.7 (2010): 429.
[127] Sun, Baoqing, et al. "3D computational imaging with single-pixel detectors." Science 340.6134 (2013): 844-847.
[128] Antipa, Nick, et al. "DiffuserCam: lensless single-exposure 3D imaging." Optica 5.1 (2018): 1-9.
[129] Lam, Edmund Y. "Computational photography with plenoptic camera and light field capture: tutorial." JOSA A 32.11 (2015): 2021-2032.
[130] Lien M B, Liu C H, Chun I Y, et al. submitted to Nature Photonics.
[131] Blocker C J, Chun I Y, Fessler J A. Low-Rank Plus Sparse Tensor Models for Light-field Reconstruction from Focal Stack Data[C]//2018 IEEE 13th Image, Video, and Multidimensional Signal Processing Workshop (IVMSP). IEEE, 2018: 1-5.
[132] Il Yong Chun, Zhengyu Huang, Hongki Lim, and Jeffrey A. Fessler, “Momentum-Net: Fast and convergent iterative neural network for inverse problems,” submitted, Jul. 2019. [Online] Available: http://arxiv.org/abs/1907.11818
[133] Balandin A A. Low-frequency 1/f noise in graphene devices[J]. Nature nanotechnology, 2013, 8(8): 549-555.
[134] Spietz L, Lehnert K W, Siddiqi I, et al. Primary electronic thermometry using the shot noise of a tunnel junction[J]. Science, 2003, 300(5627): 1929-1932.
[135] Rosenblatt, F. (1958). The perceptron: a probabilistic model for information storage and organization in the brain. Psychological review, 65(6), 386.
[136] Zhang, Dehui, et al. "Neural network based 3D tracking with a graphene transparent focal stack imaging system." Nature Communications 12.1 (2021): 1-7.

[137] Hunter N, Mayorov A S, Wood C D, et al. On-chip picosecond pulse detection and generation using graphene photoconductive switches[J]. Nano letters, 2015, 15(3): 1591-1596.
[138] Malhotra I, Jha K R, Singh G. Terahertz antenna technology for imaging applications: A technical review[J]. International Journal of Microwave and Wireless Technologies, 2018, 10(3): 271-290.
[139] Burford N M, El-Shenawee M O. Review of terahertz photoconductive antenna technology[J]. Optical Engineering, 2017, 56(1): 010901.
[140] Krotkus A, Marcinkevicius S, Jasinski J, et al. Picosecond carrier lifetime in GaAs implanted with high doses of As ions: An alternative material to low-temperature GaAs for optoelectronic applications[J]. Applied physics letters, 1995, 66(24): 3304-3306.
[141] Frankel M Y, Tadayon B, Carruthers T F. Integration of low-temperature GaAs on Si substrates[J]. Applied physics letters, 1993, 62(3): 255-257.
[142] Brown E R, Smith F W, McIntosh K A. Coherent millimeter-wave generation by heterodyne conversion in low-temperature-grown GaAs photoconductors[J]. Journal of Applied Physics, 1993, 73(3): 1480-1484.
[143] Brown E R. A photoconductive model for superior GaAs THz photomixers[J]. Applied physics letters, 1999, 75(6): 769-771.
[144] Gregory I S, Baker C, Tribe W R, et al. Optimization of photomixers and antennas for continuous-wave terahertz emission[J]. IEEE Journal of Quantum electronics, 2005, 41(5): 717-728.
[145] Winnerl S, Peter F, Nitsche S, et al. Generation and detection of THz radiation with scalable antennas based on GaAs substrates with different carrier lifetimes[J]. IEEE Journal of Selected Topics in Quantum Electronics, 2008, 14(2): 449-457.
[146] Park S G, Jin K H, Yi M, et al. Enhancement of terahertz pulse emission by optical nanoantenna[J]. ACS nano, 2012, 6(3): 2026-2031.
[147] Jarrahi M. Advanced photoconductive terahertz optoelectronics based on nano-antennas and nano-plasmonic light concentrators[J]. IEEE Transactions on Terahertz Science and Technology, 2015, 5(3): 391-397.
[148] Berry C W, Wang N, Hashemi M R, et al. Significant performance enhancement in photoconductive terahertz optoelectronics by incorporating plasmonic contact electrodes[J]. Nature communications, 2013, 4(1): 1-10.
[149] Yardimci N T, Yang S H, Berry C W, et al. High-power terahertz generation using large-area plasmonic photoconductive emitters[J]. IEEE Transactions on Terahertz Science and Technology, 2015, 5(2): 223-229.
[150] Ketchen M B, Grischkowsky D, Chen T C, et al. Generation of subpicosecond electrical pulses on coplanar transmission lines[J]. Applied Physics Letters, 1986, 48(12): 751-753.
[151] Doany F E, Grischkowsky D, Chi C C. Carrier lifetime versus ion-implantation dose in silicon on sapphire[J]. Applied Physics Letters, 1987, 50(8): 460-462.
[152] Zhong Z, Gabor N M, Sharping J E, et al. Terahertz time-domain measurement of ballistic electron resonance in a single-walled carbon nanotube[J]. Nature nanotechnology, 2008, 3(4): 201.
[153] Hou L, Shi W, Chen S. Noise analysis and optimization of terahertz photoconductive emitters[J]. IEEE Journal of Selected Topics in Quantum Electronics, 2012, 19(1): 8401305-8401305.
[154] Park, Jeong-Woo, et al. "High-Speed Traveling-Wave Photodetector with a 3-dB Bandwidth of 410 GHz." ETRI Journal 34.6 (2012): 942-945.
[155] Mikulics, Martin, et al. "Subpicosecond electron-hole recombination time and terahertz-bandwidth photoresponse in freestanding GaAs epitaxial mesoscopic structures." Applied physics letters 101.3 (2012): 031111.
[156] Yin, Jianbo, et al. "Ultrafast and highly sensitive infrared photodetectors based on two-dimensional oxyselenide crystals." Nature communications 9.1 (2018): 1-7.
[157] Kaiser W, Keck P H. Oxygen content of silicon single crystals[J]. Journal of Applied Physics, 1957, 28(8): 882-887.
[158] Förster T. Zwischenmolekulare energiewanderung und fluoreszenz[J]. Annalen der physik, 1948, 437(1-2): 55-75.
[159] Soref, Richard A., and Brian R. Bennett. "Kramers-Kronig analysis of electro-optical switching in silicon." Integrated Optical Circuit Engineering IV. Vol. 704. International Society for Optics and Photonics, 1987.
[160] Soref R, Bennett B. Electrooptical effects in silicon[J]. IEEE journal of quantum electronics, 1987, 23(1): 123-129.
[161] Hao, Ran, et al. "Ultra-compact optical modulator by graphene induced electro-refraction effect." Applied Physics Letters 103.6 (2013): 061116.
[162] Brenneis A, Gaudreau L, Seifert M, et al. Ultrafast electronic readout of diamond nitrogen–vacancy centres coupled to graphene[J]. Nature nanotechnology, 2015, 10(2): 135.
[163] Tielrooij K J, Orona L, Ferrier A, et al. Electrical control of optical emitter relaxation pathways enabled by graphene[J]. Nature Physics, 2015, 11(3): 281-287.
[164] Reserbat-Plantey A, Schädler K G, Gaudreau L, et al. Electromechanical control of nitrogen-vacancy defect emission using graphene NEMS[J]. Nature communications, 2016, 7(1): 1-6.
[165] Novoselov K S, Fal V I, Colombo L, et al. A roadmap for graphene[J]. nature, 2012, 490(7419): 192-200.
[166] G. Heilmeier, "Some Reflections on Innovation and Invention," Founders Award Lecture, National Academy of Engineering, Washington, D.C., as published in The Bridge, National Academy of Engineering, Winter 1992.
[167] Kitayama, Ken-ichi, et al. "Novel frontier of photonics for data processing—Photonic accelerator." APL Photonics 4.9 (2019): 090901.
[168] Wetzstein, Gordon, et al. "Inference in artificial intelligence with deep optics and photonics." Nature 588.7836 (2020): 39-47.